Title	Studies on Characterization and Modeling for Manganese-type Lithium-ion Secondary Batteries
Author(s)	Somakettarin, Natthawuth
Citation	大阪大学, 2018, 博士論文
Version Type	VoR
URL	https://doi.org/10.18910/69582
rights	
Note	

Doctoral Dissertation

Studies on Characterization and Modeling for Manganese-type Lithium-ion Secondary Batteries

Natthawuth Somakettarin

December 2017

Graduate School of Engineering
Osaka University

Acknowledgements

This research has been carried out during the author's tenure of doctoral course at the Graduate School of Engineering, Osaka University, under the guidance of Professor Dr. Tsuyoshi Funaki at the Division of Electrical, Electronics and Information Engineering, Graduate School of Engineering, Osaka University, Japan.

First and foremost, I would like to express my deep and sincere gratitude to my academic advisor, Professor Dr. Tsuyoshi Funaki for all of his support and giving me the opportunity to study in Japan, also for his guidance, motivation, valuable discussions and generous commitment. Throughout my doctoral work, he inspired me to develop my systematic thinking and research skill, and encouraged me for the various experiences in the conference contribution.

Second, I would like to express my sincere appreciation to Associate Professor Dr. Hideharu Sugihara for his support and valuable suggestions throughout this research work, also for reviewing my dissertation.

I would like to express my sincere appreciation to Professor Dr. Toshifumi Ise for his valuable comments and suggestions during the reviewing of dissertation.

May I also take this opportunity to express my sincere gratitude to the other members of my dissertation committee: Professor Dr. Shigemasa Takai and Professor Dr. Hiroyuki Shiraga in the Graduate School of Engineering, Osaka University for their valuable suggestions to fulfill the completeness of my dissertation.

I would like to express my appreciation to Assistant Professor Dr. Takaaki Ibuchi for his kind assistance for the facility in laboratory since he was my senior.

Acknowledgements (Cont.)

I also would like to give special thanks to Mr. Shawn Anderson, my colleague at Osaka University for editing the English manuscripts.

I would like to express my sincere thanks to Ms. Fumie Imura for her kind assistance during I stayed in Japan, and thanks all my friends especially in the laboratory for their warm helps in research and living.

I am thankful to the Royal Thai Government Scholarship for supporting the scholarship during my study in Japan.

Lastly, but most importantly, I am heartily thankful to everyone in my family for their supporting without the conditions, and giving me the encouragement through finish the research work.

Natthawuth Somakettarin

Osaka, Japan, December 2017

Preface

Lithium-ion batteries (LIBs) have gained a widespread attention as powerful energy storage and large-scale power source systems. They are anticipated as a solution to alleviate energy problems such as renewable energy storage and back-up power systems and reliable power sources of modern electric vehicles. The battery management system (BMS) needs to be developed to handle those enormous battery systems. The based knowledge for the BMS development is the understanding of nonlinear dynamic response behaviors and meanings of characteristic changes of the interested battery.

In this dissertation, the characterization and modeling of a Lithium manganese oxide secondary battery (LMO) are focussed. The aims of this study are to understand the electrochemical behaviors and characteristic responses of the LMO under various operating conditions. On the first part of dissertation, a general introduction of the LIBs and their utilizations is expressed. The literature surveys of characterization and modeling of LIBs are briefly reviewed. For the second part, the background knowledge for the LMO structure and related mechanisms of the battery during operations are introduced. The third part proposes the characterization technique and its system design in order to analyze the battery characteristics and effects of operations to the battery characteristic behaviors that are discussed in the fourth part. The modeling of LMO and the identified battery parameters based on the practical testing information are introduced and verified in the fifth part. The last part of dissertation also investigates the phase-transition mechanism and deterioration of the aging cell during the cycling operations.

The proposed characterization method, modeling, analysis techniques, electrochemical explanations and results of the study will be used to provide us essential knowledge for further development of the BMS design, and can also be applied for studying the behaviors and dynamic responses of other similar electrode Li-ion batteries.

Contents

Contents

Contents

Glossary

Ah	Ampere-hour
BMS	Battery management system
CC	Constant current
CCCA	Conditional current cutting algorithms
CCCS	Current controlled current source
CV	Constant voltage
DCV	Discharge cut-off voltage
DEKF	Dual extended Kalman filter
DV	Differential voltage
DVA	Differential voltage analysis
EC	Ethylene Carbonate
EMC	Ethyl Methyl Carbonate
EOL	End of life
ESR	Effective series resistance
ESS	Energy storage system
FCCT	Full-charged cutting current threshold
FCTR	Faradic charge-transfer resistance
GPIB	General purpose interface bus
IC	Incremental capacity
ICA	Incremental capacity analysis
LAB	Lead acid battery
LCO	Lithium cobalt oxide battery
LFP	Lithium iron phosphate battery
LIB	Lithium-ion battery
LMO	Lithium manganese oxide battery
MSE	Mean of squared residuals of the errors
NCA	Lithium nickel cobalt aluminum oxide battery
NMC	Lithium nickel manganese cobalt oxide battery
OCP	Over current protection
OCV	Open-circuit-voltage
OPP	Over power protection
SD	Standard deviations
SEI	Solid electrolyte interface
SOC	State of charge
SOH	State of health
UVP	Under voltage protection
VCVS	Voltage controlled voltage source

Chapter 1

Introduction

1.1 General overviews

Nowadays, renewable energy resources, such as solar and wind energies, have been popularized in this energy crisis decade. They are expected as a solution to mitigate energy shortage and global warming problems. The energy storage system (ESS) with battery and their management systems are the key technologies in order to utilize the renewable energy resources efficiently and worthily.

Li-ion secondary batteries (LIBs) have been of interest and continuously developed, they are considered as large-scale power sources and progressive ESS devices due to their prominent characteristics such as high energy density, high power, fast response, low self-discharge rate and long cycle and calendar life [1]. A comparison of characteristics for recent cathode technologies used in high power batteries, such as Lithium cobalt oxide (LCO), Lithium nickel cobalt aluminum oxide (NCA), Lithium nickel manganese cobalt oxide (NMC), Lithium manganese oxide (Spinel LMO), Lithium iron phosphate (LFP) and lead acid batteries (LAB), is shown in Table 1.1.

Table 1.1 Characteristics of recent cathode technologies used in the battery ESS [2-6].

Cathode technology	Nominal voltage (V)	Energy density		Thermal stability (Safety)	Life span	Cost
		Gravimetric (Wh/kg)	Volumetric (Wh/L)			
1. LCO	3.6	195	560	Poor	Good	High
2. NCA	3.6	220	600	Fair	Very good	Fair
3. NMC	3.6	205	580	Fair	Good	Fair
4. LMO	3.8	150	420	Good	Good	Low
5. LFP	3.2	90-130	333	Very good	Very good	Fair
6. LAB	2.0	33-42	40-50	Fair	Very poor	Low

Remark: *The cathodes for LIB cells no. 1-5 used with the carbon-based anode.*

The LIBs have also been widely adopted in many applications such as the electric vehicles, electronic devices, energy backup and standby units in power and telecommunication systems. The utilizations of modern Li-ion secondary batteries can be categorized into three groups by the applications and pack sizes, which are used in small devices, driving system and stationary system as shown in Figure 1.1.

These energy systems require enormous batteries, which consist of large amounts of cells to obtain the desired power, energy, rated current, and voltage. The battery management system (BMS) is necessary for the modern batteries to estimate the state of charge (SOC), monitor the electrical state and state of health (SOH), protect and control all of the batteries, and maximize the performance during the operations. The understanding of characteristics and behaviors of the batteries is important for the engineers who develop the BMS algorithms.

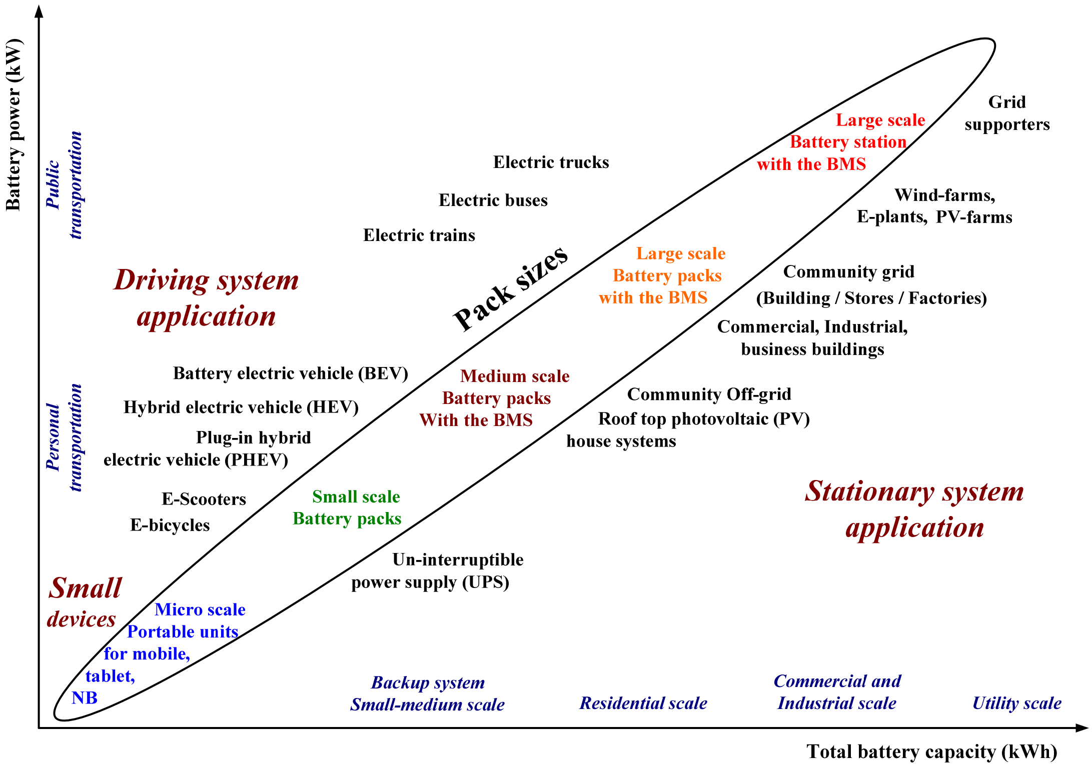

Figure 1.1 Applications of modern Li-ion secondary batteries

1.2 *Reviews of characterization and modeling of Lithium-ion batteries*

In recent years, many researchers had studied and proposed the achievements regarding the battery characterization for various applications such as the battery modeling, estimations of SOC and SOH parameters, cell capacity, and capacity loss in batteries. Non-linear characteristic models based on practical and usable capacity implementations were introduced [7] to apply in the electrical LIB modeling for predicting the battery runtime and electrical performance of the batteries, the model was validated in good agreement by comparing with the different testing conditions for polymer Li-ion and nickel-metal hydride batteries. An open-circuit-voltage (OCV) of LIBs is one of the important elements in the BMS development, which displays the electrode properties inside the battery and acts as an equivalent voltage source of the LIBs. A normalized OCV model was also proposed to a battery fuel gauge in the BMS application [8], summarizing that the internal voltage source characteristic, as the OCV, remains the same regardless of the age or temperature of the battery as long as the actual battery capacity is used in the characterization process. The SOC estimation was also introduced with applying recovery and hysteresis factors of the voltage characteristic function in olivine-type cathode batteries ($LiFePO_4$ or LFP) [9]. The empirical battery characteristic model extracted from the experiments is applied into a dual extended Kalman filter (DEKF) algorithm in order to estimate the SOC and battery capacity for the online applications by using a concept of normalized capacity computation with the same base cut-off voltage [10]. The cycling capacity loss of LIBs can be approximated with the characterized OCV parameter under different aged conditions and its residual factor that was extracted from the difference between the experiment and the model indicated in percentage of capacity loss for the aged LFP cells [11].

The benefits of battery characterization and modeling are not limited only to the state and parameter estimations, and can also be applied for investigating and studying the battery electrode properties and their related internal electrochemical behaviors. However, many previous researchers [12-14] have only studied the dynamic characteristics and parameters of the battery. Most of them do not pay attention to the concordance of the given results with physical phenomena. In order to understand the behaviors of the battery, the corresponding phenomena need to be clarified. For LIBs, the electrode properties can be identified by measuring the battery voltages under very low-current conditions. The electrode and phase transformation properties of LIBs are studied and analyzed with the advancement of OCV characterization by considering with the differential voltage and incremental capacity techniques for LFP batteries [15].

The abovementioned previous studies allow us to realize the limitations and substantial benefits obtained from the characterization and modeling. However, the viewpoints of these studies do not concentrate on the comprehensive factors that affected all accurate battery characteristic determinations. Without the investigation of various conditions, the estimation models can only work correctly in a linear range (20%–80% SOC) [16]. These are a delicate task for model-based state estimations in the BMS [17].

In this research, we focus on a lithium manganese oxide battery (LMO). The comparative characteristics of the cathode for high power batteries illustrated in Table 1.1 shows that the LMO is one of the attractive cathode technologies to be considered for the future large-scale ESS applications because of its several notable characteristics such as high nominal voltage per cell, high thermal stability, long life, low cost, high discharge current rupturing and notable performance for fast charge and discharge operations [18-19].

The studies of characterization and modeling of the LMO have become necessity since the BMS requires the accurate knowledge of characteristics and parameters for controlling the batteries. It is necessary to investigate nonlinear dynamic characteristics of the LMO with the empirical results obtained from the experiments to develop the efficient BMS algorithms. In order to obtain an accurate battery model and to investigate the battery characteristic intensively, a programmable-controlled battery characterization system needs to be developed for observing a slow response of electrochemical behaviors with safety and long-cycling operations.

1.3 Objectives of the study

The objectives of this study are shown as follows:

1) To understand nonlinear dynamic responses of the lithium manganese oxide battery (LMO) under various operating conditions such as testing current amplitudes, operating temperatures and cycling deteriorations during charge and discharge operations.

2) To understand the mechanisms of characteristic changes and relevant behaviors of the LMO through the electrical equivalent circuit components, especially the open-circuit-voltage (OCV) and effective series resistance (ESR), which are greatly influenced by the electrochemical processes inside the battery.

3) To provide an equivalent circuit model of the LMO using practical testing information for further predicting the battery behaviors and proper designing the battery management system (BMS).

1.4 Scopes of research

The scopes of research that serve the objectives are listed as follows:

1) Summarize the operating principle and relevant mechanisms of the LMO during the charge and discharge operations.
2) Design and develop a programmable Li-ion battery characterization system.
3) Design and develop a programmable Li-ion battery life-cycle-test system.
4) Analyze the changes of LMO characteristic in open-circuit-voltage (OCV), effective series resistance (ESR) and capacity (Q_B) under various operating conditions such as testing current amplitudes, operating temperatures and cycling deteriorations.
5) Model and verify the LMO electrical equivalent circuit, and identify the electrical parameters of the battery based on the experiment of transient responses.
6) Analyze the phase-transition mechanism and cycling deterioration in the LMO based on the differential voltage (DV) and incremental capacity (IC) techniques.

1.5 Dissertation outlines

The remaining details of this dissertation are organized as follows: The properties, operating principle, structure and electrical modeling of Lithium manganese oxide batteries (LMO) are described in Chapter 2. Chapter 3 proposes the characterization concept and a design of characterization systems. Chapter 4 analyzes and discusses the LMO characteristics. Chapter 5 proposes the modeling of the LMO, developed parameter identification method and its verification. The phase-transition mechanism and cycling deterioration in the LMO are analyzed in Chapter 6. Finally, conclusions and future recommended research directions are given in Chapter 7.

The chapter flow of dissertation, scopes of research and contributions of the study are summarized as shown in Figure 1.2.

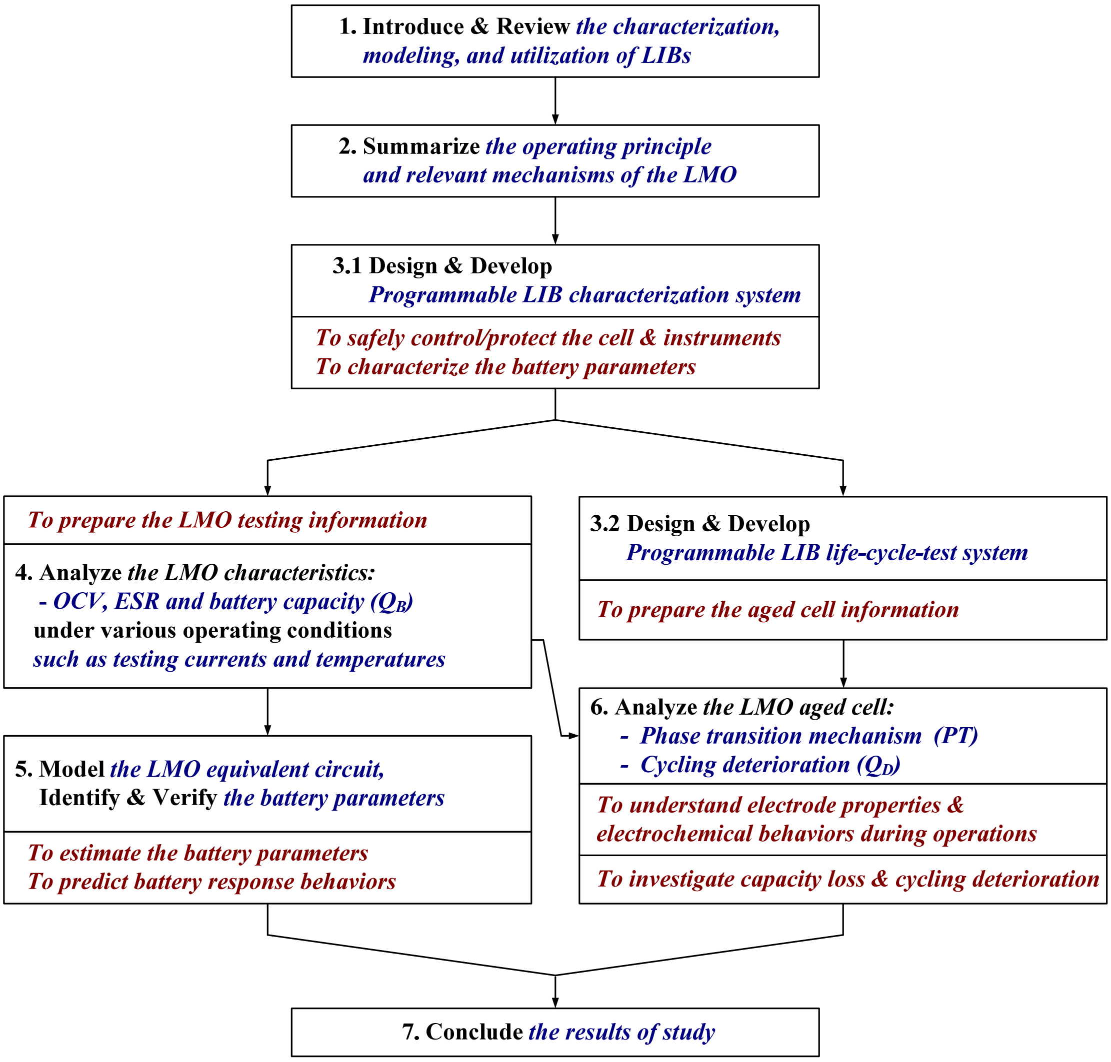

Figure 1.2 Flowchart of the chapter flow, scopes of research and contributions of the study.

1.6 References

[1] W. Schalkwijk and B. Scrosati, Advances in Lithium-Ion batteries, Springer, 2002.

[2] NPC (2015), “Battery cell and pack costs and characteristics”, [Online]. Available: http://www.cleanleap.com/.

[3] B. Lawson (2013), “Battery and energy technologies”, [Online]. Available: http://www.mpoweruk.com/.

[4] Rock tech lithium inc. (2016), “EV battery makers”, [Online]. Available: http://www.rocktechlithium.com/.

[5] C. Gonzalez (2015), “Lithium-ion power for data storage and servers”, [Online]. Available: http://www.datacenterjournal.com/.

[6] I. Buchmann (2017), “Is Li-ion the solution for the electric vehicle?”, [Online]. Available: http://batteryuniversity.com/.

[7] M. Chen and G.A. Rincon-Mora, “Accurate electrical battery model capable of predicting runtime and I-V performance”, IEEE Trans. Energy Convers., Vol. 21, pp. 504–511, 2006.

[8] B. Pattipati, B. Balasingam, G.V. Avvari, K.R. Pattipati, and Y. Bar-Shalom, “Open circuit voltage characterization of lithium-ion batteries”, J. Power Sources, Vol. 269, pp. 317–333, 2014.

[9] M.A. Roscher and D.U. Sauer, “Dynamic electric behavior and open-circuit-voltage modeling of $LiFePO_4$- based lithium ion secondary batteries”, J. Power Sources, Vol. 196, pp. 331–336, 2011.

[10] S. Lee, J. Kim, J. Lee, and B.H. Cho, “State-of-charge and capacity estimation of lithium-ion battery using a new open-circuit voltage versus state-of-charge”, J. Power Sources, Vol. 185, pp. 1367–1373, 2008.

[11] M.A. Roscher, J. Assfalg, and O.S. Bohlen, “Detection of utilizable capacity deterioration in battery systems”, IEEE Trans. Veh. Technol., Vol. 60, pp. 98–103, 2011.

1.6 References (Cont.)

[12] H. Zhang and M. Y. Chow, "Comprehensive-dynamic battery modeling for PHEV-applications", Power and Energy society general meeting, 2010-IEEE, DOI: 10.1109/PES.2010.5590108, pp. 1-6, 2010.

[13] Y. Zhang, C. Zhang, and N. Cui, "An adaptive estimation scheme for open-circuit voltage of power Lithium-Ion battery", Research article in Abstract and applied analysis, Hindawi publishing corp., Vol.2013, Article ID 481976, pp.1-6, 2013.

[14] A. Rahmoun and H. Biechl, "Modeling of Li-ion batteries using equivalent circuit diagrams", Electrical review, ISSN 0033-2097, R.88NR-7b, pp.152-156, 2012.

[15] M. Petzl and M.A. Danzer, "Advancements in OCV measurement and analysis for lithium-ion batteries", IEEE Trans. Energy Convers., Vol. 28, pp. 675–681, 2013.

[16] F. Codeca, S.M. Savaresi, and G. Rizzoni, "On Battery State of Charge Estimation: A New Mixed Algorithm", In Proceedings of the 17th IEEE International Conference on Control Applications, Part of 2008 IEEE Multi-conference on Systems and Control, San Antonio, TX, USA, pp. 102–107, 3–5 September, 2008.

[17] B. Pattipati, C. Sankavaram, and K.R. Pattipati, "System identification and estimation framework for pivotal automotive BMS characteristics", IEEE Trans. Syst. Man Cybern.-Part C Appl. Rev., Vol. 41, pp. 869–884, 2011.

[18] C.M. Julien, A. Mauger, K. Zaghib, and H. Groult, "Comparative issues of cathode materials for Li-ion batteries", Inorganics, Vol. 2, pp. 132–154, 2014.

[19] D.K. Kim, P. Muralidharan, H.W. Lee, R. Ruffo, Y. Yang, C.K. Chan, H. Peng, R.A. Huggins, and Y. Cui, "Spinel $LiMn_2O_4$ nanorods as Lithium ion battery cathodes", Nano Lett., Am.Chem. Soc., Vol. 8, pp. 3948–3952, 2008.

Chapter 2

Properties and Electrical Model of Lithium Manganese Oxide Batteries

2.1 Structure, operating principle, and relevant mechanisms of the LMO

In this section, the structure, main components, related electrochemical reaction and the operating principle inside lithium manganese oxide batteries (LMO) will be explained using a simplified schematic of the battery structure as shown in Figure 2.1.

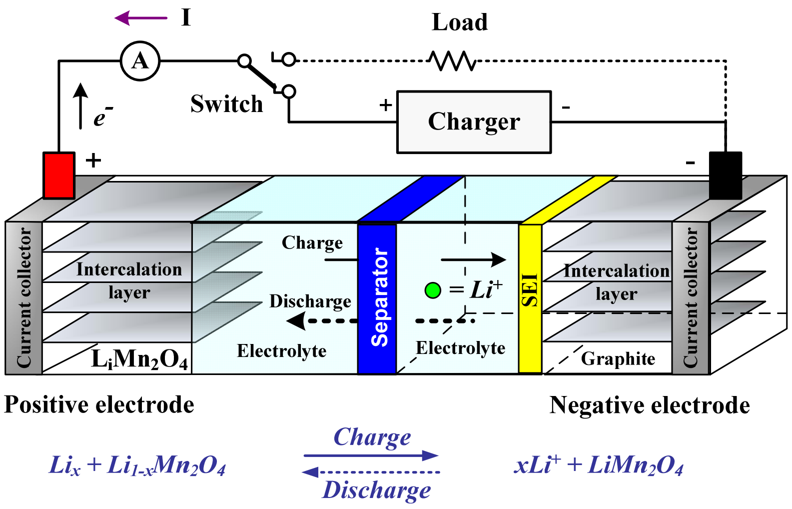

Figure 2.1 Structure of lithium manganese oxide batteries.

The LMO structure comprises of positive and negative electrodes, current collector, intercalation layers, layer of solid electrolyte interface (SEI), electrolyte and separator. Understanding the operating principle and LMO structure is essential for studying and explaining the physical behaviors that miscellaneously occur inside the battery during operations.

Main operating principle for rechargeable LMO can be divided into 2 processes. They are the charge and discharge processes. In the charge process, after energizing the rated charging voltage from the charger through the current collector via the battery terminal, the electron current is forced to flow through the external circuit from positive into negative electrodes. The current collector acts as a passage to collect the current into the cell. It is made from thin aluminium foil for the positive side and thin copper foil for the negative side.

The positive electrode is a composition of lithium manganese oxide ($LiMn_2O_4$). The electrode constitutes a porous 3D-spinel crystalline structure, which only allows the insertion or extraction of Li-ions. An LMO crystal structure is classified in an $A[B_2]O_4$ spinel-type with the cubic Fd3m space group. The spinel structure consists of eight $A[B_2]O_4$ units as $\{Li\}_{8a}[Mn_2]_{16d}O_4$ [1,2]. This constitution gives a stable structure in the spinel compound resulting in high nominal voltage per cell, low internal resistance, high discharge current rupturing, high thermal stability for over-charge, notable performance for fast charge/discharge operations, cheaper and higher safety than a conventional type such as lithium cobalt oxide battery (LCO) [3-5].

The negative electrode is made from carbon-based Lithiated graphite (LiC_6), and has a prominent property in high storage capacity due to its flat potential profile [6]. However, the negative graphite electrode has significant influences on the reduction of the potential for full cell operations, open circuit voltage (OCV) patterns and the usable capacity, especially after cycling due to the loss of active material and the degradation from a dissolution of the solid electrolyte interface (SEI) layer [7,8]. Moreover, a characteristic of the graphite electrode on the OCV pattern is more distinguished, especially when compared with other flat potential cathodes, such as LFP batteries [9].

For the charge process, the reaction that Li-ion is being extracted from the $LiMn_2O_4$ positive electrode is called the oxidation. While the reaction that Li-ion is being inserted into the negative electrode is called the reduction. The extracted Li-ion from the positive electrode moves through the electrolyte and separator into the negative electrode inside the battery. On the contrary, for the discharge process after the switch has moved to the load, a Li-ion then moves back from the negative to positive electrodes through the electrolyte. At the same time, the electron current is also moved to the positive electrode at opposite direction of the charge process through an external circuit outside the battery for compensating a balance reaction of the battery. In addition, the negative electrode for rechargeable LIBs is defined as an anode when it released Li-ions during the discharge, and is defined as a cathode when it received Li-ions during the charge. Cathode and anode definitions of rechargeable LIBs depend on the direction of Li-ions flowing at that electrode.

During the charge and discharge operations, Lithium ions (Li^+) are inserted into, and are extracted from the crystalline structure of electrodes that is also called the intercalation layer or host lattice. These operating processes are called the intercalation and de-intercalation mechanisms, respectively. Due to the consistency of structure during operations, this battery type is safe for operations. However, the reactions of Li-ion intercalation and de-intercalation are onerous for aging batteries. They can lead to a gradual decrease of the capacity during the cycling operations. [6,10,11].

In addition, the electrodes are separated by a polymer separator, which has structured as a porous membrane. This separator is used to prevent electrical short circuits between the electrodes, while it only allows the reversible ionic charge transportation of the lithium. During the intercalation, Li-ions can only transport via the Lithium salt electrolyte (Lithium hexafluorophosphate, or $LiPF_6$), which has dominant properties in high ionic conduction and high electronic insulation.

The electrolyte conductivity depends on the electrolyte temperature and organic solvents. The increment of temperature facilitates a conductivity of the electrolyte. However, the electrolyte solution is unstable at a rise temperature around 60°C, and the electrolyte conductivity is gradually decreased at the temperature above 80°C. The electrolyte can dissolve in the organic solvents as Ethyl Methyl Carbonate (EMC) and the co-solvent as Ethylene Carbonate (EC). On the surface of the negative graphite electrode, a solid electrolyte interface (SEI) layer is formed by the EC. This layer acts as a protective film to prevent the solvent molecules entering the graphite electrode. For the effective protection, the SEI must be operated under the cell temperature below than 70°C [12-15].

2.2 Understanding of phase-transitions in the LMO

An understanding of phase-transition mechanisms is important in order to study the state of health (SOH) and deterioration occurring inside the battery. A battery management system (BMS) is indispensable for safety and long-cycling operations. The SOH of the LIBs is one of the important elements in the BMS to observe the trends of deterioration before occurring the fault and end of life (EOL) of the batteries [16,17].

The BMS development requires an understanding of the internal electrochemical behaviors of the LIBs. The key process to understand the phenomena regarding the SOH and deteriorations inside the battery is a phase-transition mechanism study during the charge and discharge operations. The understanding of the phase-transition is also significant for studying the changes of electrical conductivity in the LMO due to a temperature variation during operations [18].

The phase-transition is referred to as a crystal structure change during the cycling operations, which is reversible between the cubic (Fd3m) and orthorhombic (Fddd) forms of crystal system. During cycling operations, the LMO can be recharged and discharged many times between the electrodes via intercalation and de-intercalation mechanisms.

The phase-transitions of LMO are associated with two features of intercalation and de-intercalation. One is the lithiation of λ-MnO_2, which is a lithium insertion into a spinel electrode leading to $Li_2Mn_2O_4$. The other one is the de-lithiation of $LiMn_2O_4$, which extracts the lithium from the same electrode leading to λ-MnO_2 [19].

In this study, the phase-transition will be studied within the specified cell voltage range (The details will be shown in the next chapter). The operations under/over the range will be prohibited to avoid the violation of operations under/over voltage limits of the cell.

The phase-transition is closely related with the battery deterioration, which is presented by the OCV variation. In order to understand the characteristic changes and phase transformation behaviors, the OCV characterization system needs to be developed, as shown the details in Chapter 3.

2.3 Electrical equivalent circuit model of the LIB

The electrical equivalent circuit modeling in this study is based on a transient response. This model considered the practical testing information to study the electrochemical phenomena through the electrical components.

2.3.1 Transient response model

A transient response model is referred to the second order Randle's equivalent circuit model [20], which was originally proposed for the lead acid batteries. The transient response model for the LMO is shown in Figure 2.2.

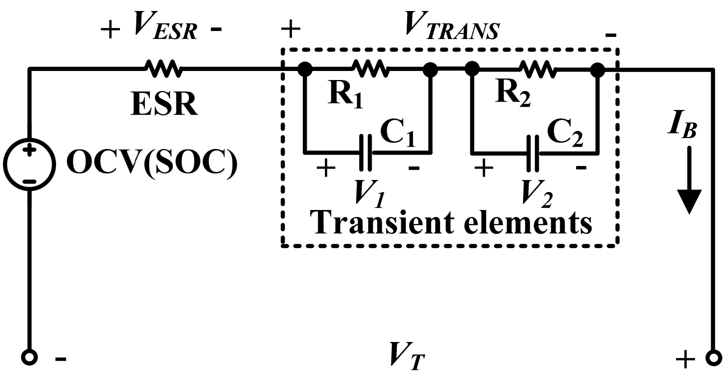

Figure 2.2 Transient response model of the LMO battery.

It comprises of four components as follows:

- The voltage source, called open-circuit-voltage (OCV), displays the unique characteristic property of the electrodes for each battery type. The OCV is generally indicated as a function of the state of charge (SOC). Details for the OCV will be explained in the next section.
- The bulk ohmic resistances of the cell is called effective series resistance (ESR or R_0), which reflects the major resistances of the connecting wires, electrodes, separator and electrolyte.
- The first RC parallel circuit reflects the faradic charge-transfer resistance (FCTR or R_1) and its related double-layer capacitance (C_1).
- The second RC parallel circuit reflects the resistance (R_2) and capacitance (C_2) for the diffusion process in electrolyte [21].

In order to study and understand the battery behaviors, the study of related parameters under various operating conditions is needed. For the scope of this study, we intensively focus on characteristic changes in open-circuit-voltage (OCV) and effective series resistance (ESR), because they are greatly influenced by the electrochemical processes inside the battery [22].

2.3.2 Dynamic voltage behaviors of LIBs

Dynamic voltage behaviors of the LIB cell are shown in Figure 2.3, which is observed for a pulse test with the developed characterization system. The details of the system will be explained in Section 3.

After applying the discharge pulse current, the voltage at battery terminals is instantaneously dropped down as illustrated with the red line in Window A of Figure 2.3. This immediate drop phenomenon is called the instantaneous response, which occurs from the voltage drop (V_{ESR}) across the equivalent bulk resistance (ESR). The depth of voltage drop depends on ohmic equivalent resistances of the electrolyte, separator and electrodes of the battery.

The cell voltage has continuously decreased over the time for discharging as illustrated with the black dash line in Figure 2.3. This smooth change of exponential voltage is called the transient response, which is expressed by the voltage drop across the equivalent RC parallel pairs of the circuit in Figure 2.2.

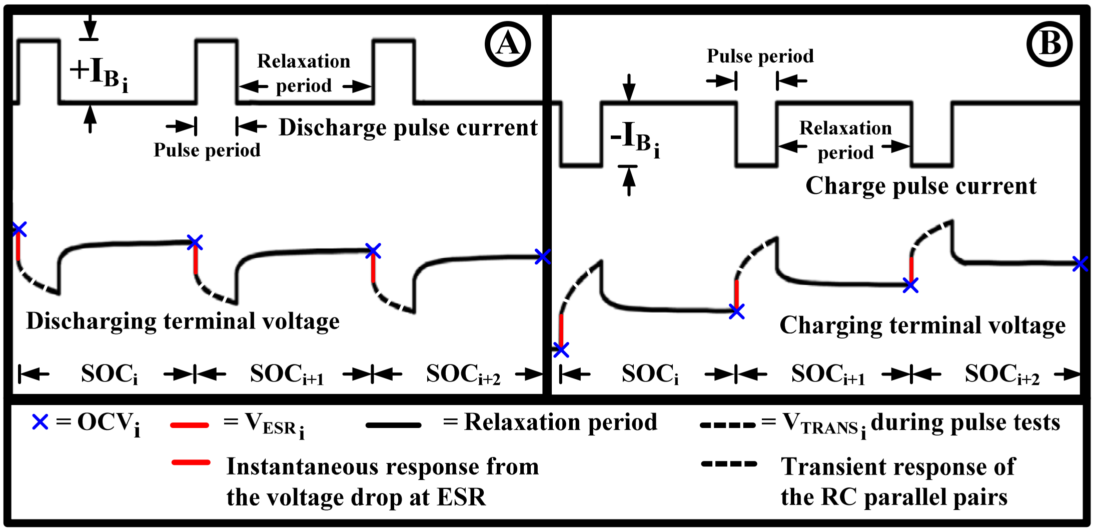

Figure 2.3 Dynamic voltage behaviors of LIBs

The black solid line of voltage in Figure 2.3 indicates the voltage response of the relaxation period. In this period, the voltage at the battery terminals is relaxed after disconnecting of pulse current to balance the internal electrochemical reaction. The cell has reached to its equilibrium condition at the end of relaxation. The measured terminal voltage is estimated as the OCV as shown with the blue cross of Figure 2.3. The investigation details of the OCV and its optimum relaxation time will be shown in Chapter 4. At the same time, the dynamic voltage response for the charge process can be observed as shown in Window B of Figure 2.3.

2.4 Chapter summary

This chapter gathers and describes the properties, operating principle, structure and electrical modeling of Lithium manganese oxide batteries (LMO). The studying of LMO structure is for the equivalent circuit modeling of battery. Intercalation and de-intercalation mechanisms are important for characterizing the behaviors, and to analyze the characteristic results of the battery.

2.5 References

[1] J. Sugiyama, T. Tamura, and H. Yamauchi, “Elastic/anelastic behavior during the phase transition in spinel $LiMn_2O_4$”, J. Phys., Vol. 7, pp.9755-9764, 1995.

[2] K. Ozawa, Lithium Ion Rechargeable Batteries: Materials, Technology, and New Applications, Wiley-VCH Verlag GmbH, Germany, 1st ed., pp.103-157, 2009.

[3] C.M. Julien, A. Mauger, K. Zaghib, and H. Groult, “Comparative issues of cathode materials for Li-ion batteries”, Inorganics, Vol. 2, pp. 132–154, 2014.

[4] D.K. Kim, P. Muralidharan, H.W. Lee, R. Ruffo, Y. Yang, C.K. Chan, H. Peng, R.A. Huggins, and Y. Cui, “Spinel $LiMn_2O_4$ nanorods as Lithium ion battery cathodes”, Nano Lett., Am.Chem. Soc., Vol. 8, pp. 3948–3952, 2008.

[5] A. Patil, V. Patil, D.W. Shin, J.W. Choi, D.S. Paik, and S.J. Yoon, “Review issue and challenges facing rechargeable thin film lithium batteries”, Mater.Res., Bull. 43, 1913–1942, 2008.

[6] T. Piao, S. M. Parka, C. H. Dohb, and S. I. Moon, “Intercalation of Li-ion into Graphite electrodes studied by AC impedance measurements”, J. Electrochem. Sci., Vol.146(8), pp.2794-2798, 1999.

2.4 References (Cont.)

[7] J. Wang, J. Purewal, P. Liu, J.H. Garner, S. Soukazian, E. Sherman, A. Sorenson, L. Vu, H. Tataria, and M.W. Verbrugge, "Degradation of lithium ion batteries employing graphite negatives and nickel-cobalt-manganese oxide + spinel manganese oxide positives: Part 1, aging mechanisms and life estimation", J. Power Sources, Vol. 269, pp. 937–948, 2014.

[8] A.J. Smith, J.C. Burns, and J.R. Dahn, "High-precision differential capacity analysis of $LiMn_2O_4$/graphite cells", Electrochem., Solid-State Letter, Vol. 14, pp. A39–A41, 2011.

[9] M. Safari and C. Delacourt, "Aging of a commercial graphite/$LiFePO_4$ cell", J. Electrochem., Vol. 158, pp. A1123–A1135, 2011.

[10] M. Urbain, M. Hinaje, S. Raël, B. Davat, and P. Desprez, "Energetical modeling of Li-ion batteries", Industry Applications Conf., 42nd IAS Annual Meeting conference of IEEE, LA, USA, pp. 714-721, 2007.

[11] G. W. Ling, X. Zhu, Y. B. He1, Q. S. Song, B. Li, Y. J. Li, Q. H. Yang, and Z. Y. Tang, "Structural and thermal stabilities of spinel $LiMn_2O_4$ materials under commercial power batteries cycling and abusive conditions", Int. J. Electrochem. Sci., Vol.7, pp.2455-2467, 2012.

[12] P. Arora and Z. J. Zhang, "Battery Separators", Chemical Reviews, Vol.104(10), pp.4419-4462, 2004.

[13] H.J. Bergveld , W.S. Kruijt, and Peter H. L. Notten, Battery management systems: Design by modeling, Philips research vol.1, Springer, pp.31-52, 2002.

[14] C. H. Doh, D. H. Kim, J. H. Lee, D. J. Lee, B. S. Jin, H. S. Kim, S. I. Moon, Y. Hwang, and A. Veluchamy, "Thermal behavior of Li_xCoO_2 cathode and disruption of solid electrolyte interphase film", Bull, Korean Chem. Soc., 30 (4), pp.783–786, 2009.

2.4 References (Cont.)

[15] M.B. Pinson and M. Z. Bazant, "Theory of SEI formation in rechargeable batteries: Capacity fade, accelerated aging and lifetime prediction", Dept. of Physics, MIT, USA, pp.3-5, 2012.

[16] B. Pattipati, C. Sankavaram, and K.R. Pattipati, "System identification and estimation framework for pivotal automotive BMS characteristics", IEEE Trans. on Systems, Man, and Cybernetics, Vol. 41(6), pp. 869-884, 2011 (DOI: 10.1109/TSMCC.2010.2089979).

[17] H. Rahimi-Eichi, U. Ojha, F. Baronti, and M.Y. Chow, "Battery management system: An overview of its application in the smart grid and electric vehicles", IEEE Industrial Electronics. Mag., Vol. 7(2), pp. 4-16, 2013 (DOI: 10.1109/MIE.2013.2250351).

[18] M. Parka, X. Zhanga, M. Chunga, G. B. Lessa, and A. M. Sastry, "A review of conduction phenomena in Li-ion batteries", J. Power sources, Vol.195(24), pp.7904-7929, 2010.

[19] G. Amatucci and J.M. Tarascon, "Optimization of insertion compounds such as $LiMn_2O_4$ for Li-ion batteries", J. of Electrochem, Vol. 149(12), pp. K31-K46, 2002.

[20] D. Andrea, Battery management systems for large Li-ion battery packs, Artech house press, Boston, 2010.

[21] E. Kuhn, C. Forgez, P. Lagonotte, and G. Friedrich, "Modeling Ni-MH battery using Cauer and Foster structures", J. Power Sources, Vol. 58(2), pp. 1490-1497, 2006.

[22] S.S. Zhang, K. Xu, and T.R. Jow, "Electrochemical impedance study on the low temperature of Li-ion batteries", Electro-chim. Acta, Vol. 49(7), pp.1057-1061, 2004.

Chapter 3

Characterization Method and System

This chapter shows the characterization method and the developed characterization system for the LMO batteries. In recent years, many manufacturers proposed their own best technology for the copyrighted battery test system with several testing features. However, most of them have separated into the individual units depending on the purposes of study and investigation with the specific ranges of battery rating [1-4]. The modern LIBs have always been invented and pervasively developed for several applications with different usage environments. The test systems must extensively be able to handle the changes of those various battery technologies and testing conditions. The limitation of the existing test systems for the end-users is the difficulty in developments of individual hardware/software controlling, interactive monitoring and testing algorithms for the various LIBs. Therefore, our-owned characterization system needs to be developed. The aims of this development are: 1) to integrate all of necessary features for the battery performance tests into one system with the flexibilities of modification, maintenance and further developments to support any modern LIBs; and 2) to extract the parameters of LIB for modeling the battery behaviors under several operating conditions, and to identify characteristic changes regarding the phase transformations and cycling deterioration with a safety. The details of the tested cell, characterization method, design of developed system, comparison of features with conventional test systems and criteria for the aged cell preparation will be introduced in the next sections.

3.1 Cell for testing

In this research, a pouch type single-cell manganese Li-ion secondary battery from NEC Tokin Corporation was used for studying the characteristics and extracting the electrical parameters. The details of cell specification are shown in Table 3.1.

Table 3.1 Cell specification

Description		Specification
Electrode type: Spinel single cell	Manganese Oxide // Lithiated graphite	$LiMn_2O_4$ // LiC_6
Rated capacity		3.5Ah
Terminal voltage	Nominal value	3.8V
	Rated charging	4.2V
	Rated discharging	3.0V
Max. continuous current (C-rate)	Charging	3.5A (1C)
	Discharging	20.0A (5.7C)
Operating temperature	Charging range	0 to 40° C
	Discharging range	-10 to 50° C
Cell dimension	70 mm x 124 mm x 4 mm	
Volume	0.03472 liters	
Maximum weight	100 g	

Remark: C-rate is a unit to define the operating current values of the batteries, and used for expecting the operating times of charge and discharge.
C-rate = Operating current (A) / Rated capacity of the battery (Ah).

3.2 Characterization of OCV

This section introduces a methodology for OCV characterization. The OCV in the circuit of Figure 2.2 is extracted as a measured voltage at battery terminals (V_T) after relaxing from the applied short pulse currents both on the discharge and charge operations to settle the battery to its equilibrium state [5]. This method is called the OCV pulse test based on the galvanostatic intermittent titration technique [6].

After a long resting to make sure that the cell voltage is constant and close to its equilibrium (The optimum resting period will be investigated in Section 4.2), the battery current and voltages across the effective series resistance (V_{ESR}) and transient elements (V_{TRANS}) become zero. Then, the V_T in Equation (3.1) is deserved as the OCV:

$$V_T = OCV - V_{ESR} - V_{TRANS} \tag{3.1}$$

For the OCV characterization, the other parameters, such as the effective series resistance (ESR) and transient elements as mentioned in Figure 2.2 will be ignored because they have no effect on the OCV.

Usually, the OCV is illustrated as a function of the SOC. The SOC is defined as the available charge at the interested point to the total charge of the fully charged cell. The SOC calculation based on the coulomb counting method is shown in Equation (3.2). The accumulated capacity of the battery is given by Equation (3.3). The test is performed within operating voltage ranges of the cell between 3.0V and 4.2V (0-100% of SOC).

$$SOC(t) = SOC_0 - \int_{t_0}^{t_{cut-off}} \frac{I_B(t)}{3600 \times Q_B} dt \tag{3.2}$$

$$Q_B = \frac{1}{3600} \int_{t_0}^{t_{cut-off}} I_B(t)\, dt \tag{3.3}$$

Where

I_B = Battery current (A), which has a positive sign for the discharge and negative sign for the charge

Q_B = Accumulated capacity of the battery (Ah)

SOC = State of charge of the battery (the SOC is between 0 and 1)

SOC_0 = Initial value of the SOC

t_0 = Starting time of testing

$t_{cut-off}$ = Cut-off time of testing after reaching the operating voltage limits of the battery

3.3 Characterization of ESR

This section introduces a methodology for ESR characterization. The ESR in the circuit of Figure 2.2 can be extracted using the same test system for the OCV characterization. After applying a pulse current into the terminal of battery for each SOC, the ESR can be calculated by the ratio of instantaneous response of voltage drop to the battery current based on the ohm's law [7] as shown in Equation (3.4). The details of instantaneous response and voltage drop at ESR were shown in Figure 2.3.

$$ESR = V_{ESR} / I_B \tag{3.4}$$

Where

ESR = Effective series resistances (Ω)

V_{ESR} = Instantaneous response of voltage drop across the effective series resistance.

3.4 Characterization system

The characterization of LIB parameters usually takes a significant amount of time due to a slow response of electrochemical behaviors for the intercalation and de-intercalation processes. In order to safely extract the parameters OCV, ESR, Q_B and SOC, it is necessary to develop a reliable test system.

In this section, a computer-controlled characterization system is developed as shown in Figure 3.1. The test system comprises of the programmable DC supply (max 60V/25A, 1500W), DC electronic load (max 150V, 200A), multi-channel memory recorder with a current probe of 30A, precise digital voltmeter ($5^{1/2}$ digits), computer-based control with monitoring system and temperature/humidity chamber for controlling the test environment between 0^{o}C and 40^{o}C. General purpose interface bus (GPIB)-based sequential-control and protective algorithms were implemented with a LabVIEW environment for controlling the charge and discharge processes and testing instruments. This system is used to control the testing instruments and record the parameters for studying the dynamic responses of the LIB.

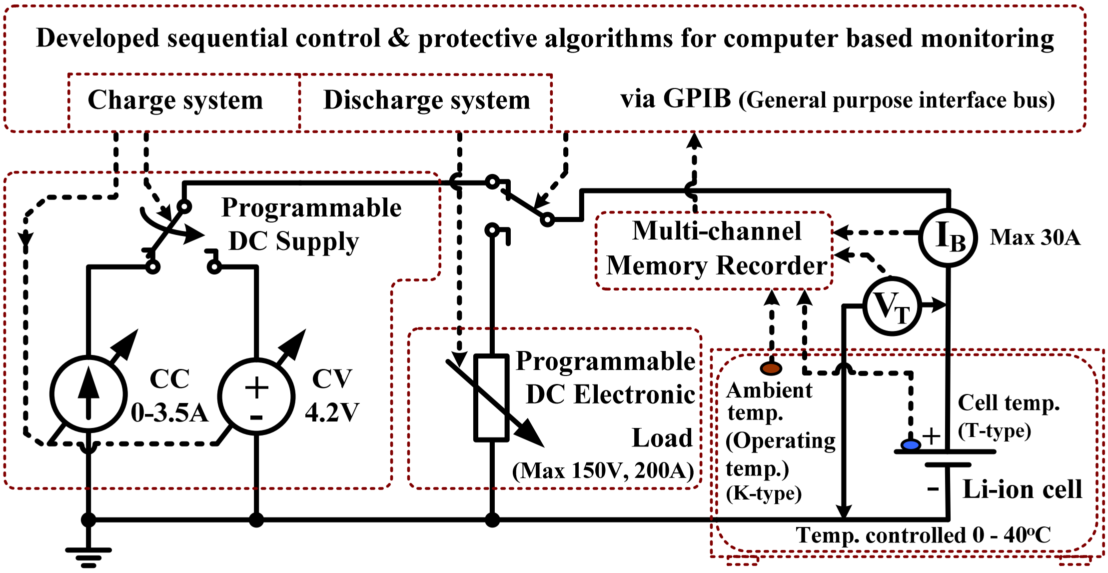

Figure 3.1 A developed computer-controlled characterization system.

3.4.1 Design criteria of characterization system

The test system could manage all of sequential operations automatically without malfunctions for any LIB types to the parameters such as current amplitudes (in C-rates), step-sizes of the pulse test, rest times, pulse cycles, current and voltage protection limits and charge/discharge cut-off voltages.

Moreover, the system could record the instantaneous status (with 10ms/sampling) during the operations such as battery current, voltage, tested cycle, SOC, testing and resting durations, date, time, status and alarm messages in case of violating the protection limits. It could represent them onto the display monitor and immediately cut-off the instruments and battery after occurring the faults.

The control sequence of characterization system is divided into the following 2 parts: one is the discharge system, and the other is the charge system.

3.4.2 Design of discharge system

A proposed discharge system with the sequential-control flowchart and the discharge characterization procedure are shown in Figure 3.2.

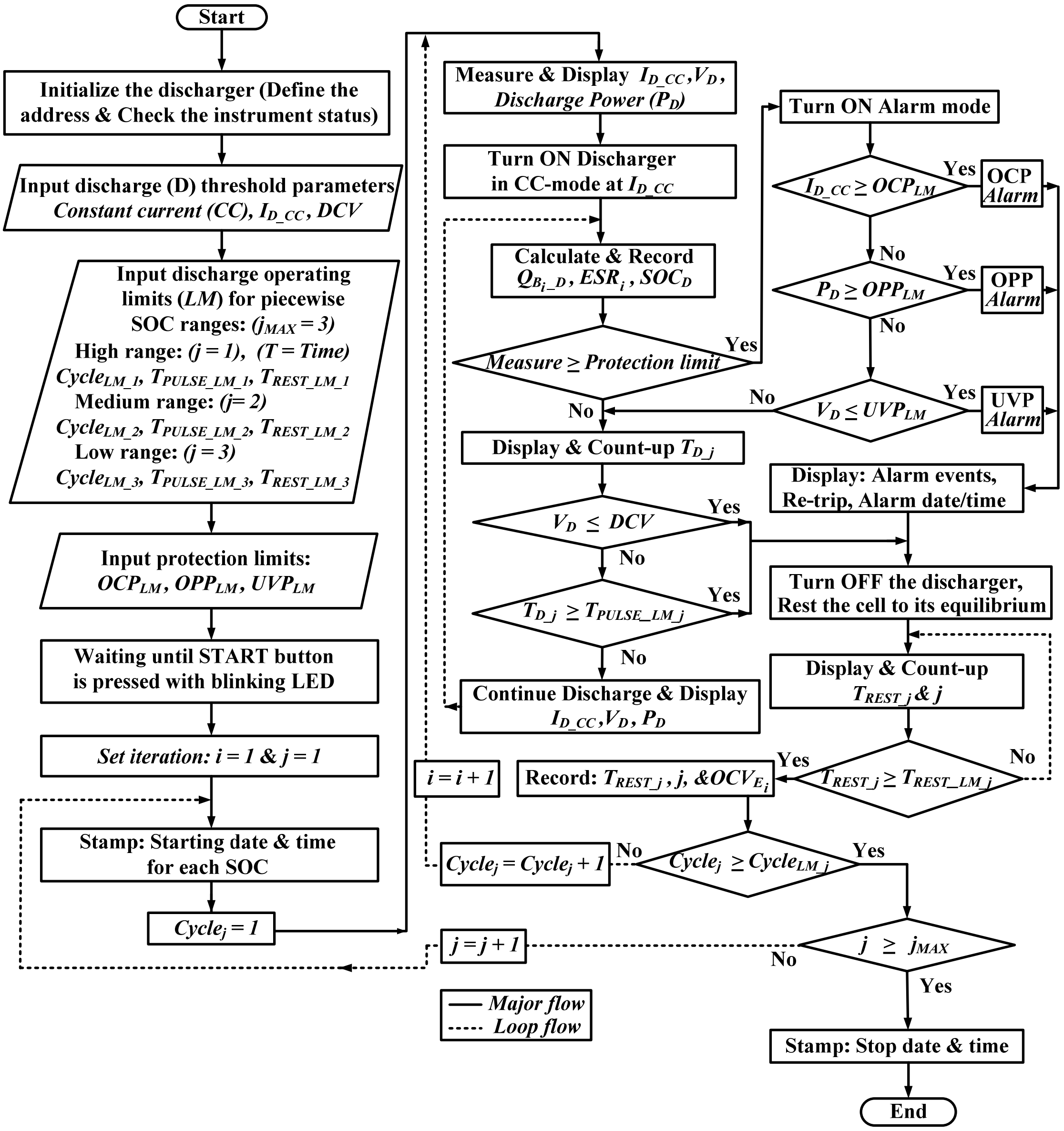

Figure 3.2 A proposed discharge system for parameter characterization.

Over current (OCP), over power (OPP) and under voltage (UVP) protections, as well as discharge cut-off voltage limit (DCV) detection were designed to test the LIB safely in the discharge system.

The battery is discharged following sequential procedures. The discharge current is cut when reaching the pulse discharge time for each cycle with the conditional current cutting algorithms (CCCA). The cell rests until the voltage is settled and close to its equilibrium and the OCV is recorded. During the discharge operations, the accumulated charge, ESR and SOC are also calculated. The test is repeated until reaching the discharge cut-off voltage limit (DCV), and the protection system turns off the discharger if it detects some failures during the operation.

3.4.3 Design of charge system

A charge system based on the constant current to constant voltage (CC-CV) method was designed for the battery parameter characterization to prevent the over charge. A proposed charge system with the sequential control flowchart and the charge characterization procedure are shown in Figure 3.3. Conditional current cutting algorithms (CCCA) for our CC-CV module are divided into three modes as follows:

- The first mode is a full-charged cutting mode, which cuts off the charger when the current exceeds a full-charged cutting current threshold (FCCT). In the CV state, the cell voltage is kept constant. Then, the cell current is reduced to zero. The FCCT value is set at 0.1% (0.001C-rates) to make sure that the battery reaches a full charge.

- The second mode is a pulse-timer mode (PULSE_C), which is used for the parameter extraction. This mode considers the current cutting conditions on both the pulse time and the FCCT value. The process for recording the extracted parameters is similar to the discharge system.

- The third mode is a standard-charge mode (STD_C). It charges by the CC-CV method, and is then cut off at 2.5hrs. This mode is recommended by the manufacturer in order to charge the battery in a standard condition before any discharge tests occur, and in order to compare the battery capacity under the different environments. During the charge processes, the accumulated charge, ESR and SOC are also calculated.

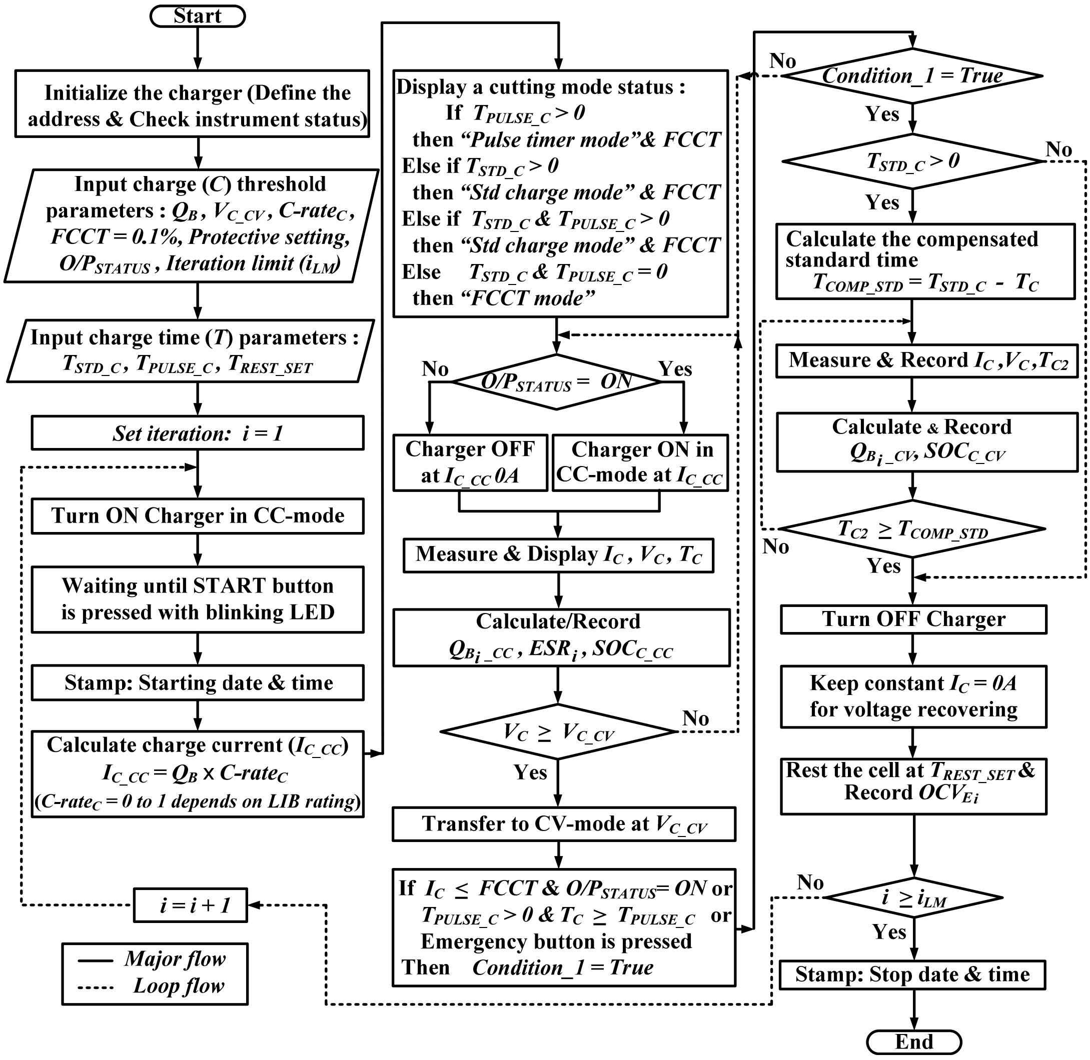

Figure 3.3 A proposed charge system for parameter characterization.

3.5 Characterization of aged cell and preparation

In order to investigate the cycling deterioration of the LIB, the aged cell needs to be prepared. The characterization of aged cells is performed by using the same test system and procedures as mentioned in Section 3.4.

A programmable sequential-controlled life-cycle-test system for the aged cell preparation is designed and developed based on the concept and design criteria of charge and discharge systems for LIB characterization.

The test system is setup following the standard testing condition in a temperature chamber at 20^{o}C, and the cycling cell is operated within the voltage range between 3V and 4.2V with a full rate of charge and discharge operations using the same testing configuration as in Figure 3.1.

The cell has operated for 400 cycles, 1,200 cycles and 2,400 cycles to be the equivalent aged cell for 1 year, 3 years and 6 years, respectively. For each desired cycle, the cell will be characterized and recorded the aging information. The investigation details of cycling deterioration will be shown in Chapter 6.

During a cycling test, the cell is protected by our developed protection system algorithm as same as in the characterization system. If it detects some failures, the charger and discharger are then turned-off with sending an alarm message. A flowchart of proposed life-cycle-test system for aged cell preparation is shown in Figure 3.4.

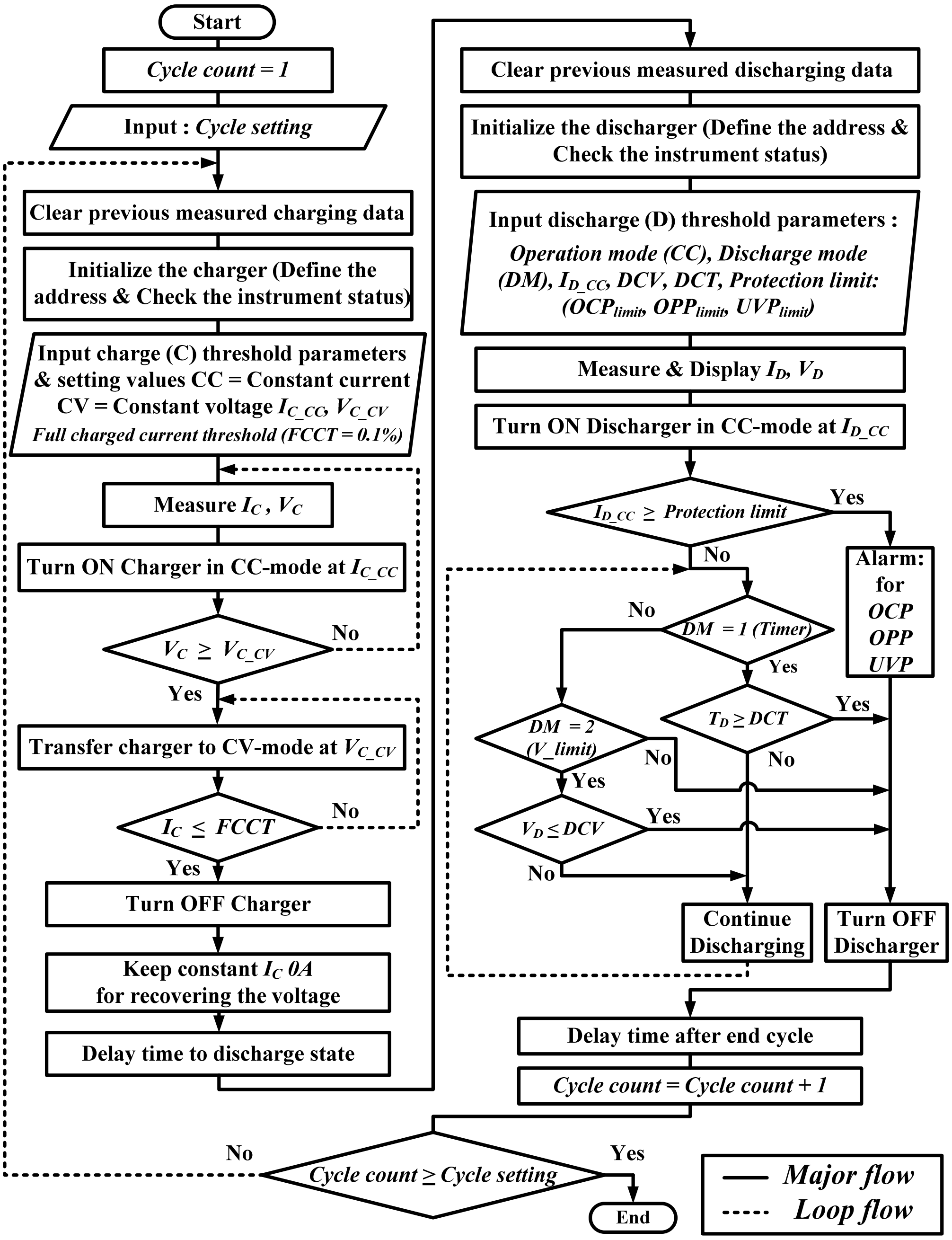

Figure 3.4 A proposed life-cycle-test system for aged cell preparation.

3.6 Features of the developed LIB test system

This section summarizes all of features of the developed battery cell test system. The comparison of features of the developed test system compared with conventional test systems [1-4] is shown in Table 3.2.

Table 3.2 Feature comparison of the developed test system

Issues and features of battery test system	**Conventional test system**				**Developed test system**
	[1]	**[2]**	**[3]**	**[4]**	
Charge control features					
- Constant current (CC) setting/measurement	/	/	/	/	/
- Constant voltage (CV) setting/measurement	/	/	/	/	/
- Automatic CC-CV charging/measurement	/	/	/	/	/
- Charge capacity test/measurement	/	/	/	-	/
- Continuous-timer CC-CV charging mode	/	/	/	/	/
- Pulse-timer CC-CV charging mode	-	-	/	-	/
- Delay time setting during the charge cycle test	-	-	-	-	/
- Percentage setting of full-charge cutting current	-	-	-	-	/
- Standard charging mode	/	/	/	/	/
- Easy setting of charging current in C-rate & Ah	-	-	-	-	/
Discharge control features					
- Constant current (CC) setting/measurement	/	/	/	/	/
- Constant voltage (CV) setting/measurement	/	/	-	/	/
- Constant power (CP) setting/measurement	/	/	/	/	/
- Discharge capacity test/measurement	/	/	/	-	/
- Discharge cut voltage (DCV) control/setting	/	/	/	/	/
- Continuous discharging + cutting with DCV/timer	/	/	/	/	/
- Pulse discharging + cutting with DCV/timer	-	-	/	/	/
- Delay time setting during the discharge cycle test	-	-	-	-	/
- Easy setting of discharging current in C-rate & Ah	-	-	-	-	/
Specific characterization features					
- Life cycle test	S	/	/	/	/
- OCV test	S	S	*	S	/
- ESR calculation	S	S	*	S	/
- SOC calculation	S	-	-	-	/

Remark: / = Yes, - = No, S = Separated into individual module with cost,
* = Can be done in the future with higher cost,
# = Can be done in the future with lower cost.

Table 3.2 (Cont.) Feature comparison of the developed test system

Issues and features of battery test system	**Conventional test system**				**Developed test system**
	[1]	**[2]**	**[3]**	**[4]**	
Manipulation features					
- Integrating all necessary features into one system	-	*	-	*	/
- Numerical setting/menu bar for input parameters	/	/	/	/	/
- Temperature control	S	S	S	-	/
- Interactive controlling on display operation	-	-	-	-	/
- Real-time display monitoring	-	-	/	/	/
- Automatic display testing status & operation mode	/	/	/	/	/
- Display testing parameters V, I, P, time/date	/	-	/	/	/
- Record testing parameters V, I, P, time/date	/	/	/	/	/
- Export to Excel/Data files	/	/	/	/	/
- Computer based monitoring	/	/	-	/	/
- Various types of battery testing	/	/	/	*	/
- Multi-channel/large packs of battery testing	S	/	*	S	*
Sequential control features					
- Sequential control setting	S	/	/	/	/
- Automatic Charge => Discharge	/	/	/	/	/
- Automatic Charge => different-steps of discharge	-	-	#	-	/
- Automatic Discharge => Charge	-	/	/	/	/
Protection features					
- Interactive push-button Start/Stop button	-	-	-	-	/
- Emergency stop button	-	-	-	-	/
- Over current protection (OCP)	/	/	/	/	/
- Over power protection (OPP)	/	/	-	-	/
- Under voltage protection (UVP)	/	/	-	-	/
- Over voltage protection (OVP)	/	/	/	/	/
- Cut-off the system after faults	/	/	/	/	/
- Display and record date/time of faults	/	/	/	-	/
- Flashing signal warning for faults	-	-	-	-	/
- Display alarm status messages	-	-	-	-	/
- Re-trip alarm function then cut-off the system	-	-	-	-	/
Further developments					
- Expand to higher voltage/current ranges	*	*	*	-	#
- Flexible to modify the sequential testing controls	*	*	-	-	#
- Easy to replace/maintenance	*	*	*	#	#

Remark: / = Yes, - = No, S = Separated into individual module with cost,
* = Can be done in the future with higher cost,
# = Can be done in the future with lower cost.

3.7 Chapter summary

This chapter described the procedure of characterization based on the pulse test method for the LMO battery. The model equations for the battery characterization such as OCV, ESR, SOC, capacity are also explained. This chapter also designed and developed the computer-based characterization system implemented with sequential-controlled and protection algorithms of charge and discharge to study the battery characteristic properties. The life-cycle-test system is also developed to prepare the aged cell and information for investigating the cycling deterioration. The new mixed features of charge and discharge algorithms for battery performance tests, such as conditional current cutting with interactive on-screen display control and protection algorithms integrated with the specific battery characterization features for all-in-one test system, are proposed and compared with the conventional test systems. The testing procedures, characterization techniques and developed system can also be applied for studying the voltage properties and characteristic variations of any Li-ion battery types.

3.8 References

[1] Chroma ATE Inc. (2017), “Battery test solutions”, [Online]. Available: http://www.chromaate.com/.

[2] Arbin Instruments (2017), “Battery test equipment”, [Online]. Available: http://www.arbin.com/.

[3] Cadex Electronics Inc. (2014), “Battery testing system”, [Online]. Available: http://www.cadex.com/.

[4] Hokuto Denko Corp. (2017), “Battery charge/discharge system”, [Online]. Available: http://www.hokuto-denko.co.jp/.

[5] M. Petzl and M.A. Danzer, “Advancements in OCV measurement and analysis for lithium-ion batteries”, IEEE Trans. Energy Convers., Vol. 28, pp. 675–681, 2013.

3.8 References (Cont.)

[6] W. Weppner, R.A. Huggins, “Determination of the kinetic parameters of mixed-conducting electrodes and application to the system Li_3Sb”, J. Electrochem. Soc., Vol. 124, pp. 1569–1578, 1977.

[7] H.G. Schweiger, O. Obeidi, O. Komesker, A. Raschke, M. Schiemann, C. Zehner, M. Gehnen, M. Keller, and P. Birke, “Comparison of several methods for determining the internal resistance of Lithium ion cells”, Sensors, Vol. 10, pp. 5604-5625, 2010.

Chapter 4

Analysis of LMO Characteristics

In this chapter, the LMO characteristics, which obtained from the characterization system in Chapter 3, are analyzed under the difference of experimental conditions. Several aspects of the adjusting factors for operating condition, such as the step-sizes of pulse tests, resting periods of the cell, testing current amplitudes (C-rates) of the pulse, and continuous charge-discharge tests, hysteresis phenomena, terminal voltage relationships and operating temperatures on the OCV, ESR and capacity characteristics, will be discussed and evaluated to understand nonlinear characteristics and related behaviors of the LMO, to obtain precise information for the parameter extraction, and to further design management algorithms of the BMS application.

4.1 Effect of step-size in the pulse test on the OCV characteristic

In this section, the effect of the step-size in the pulse test is experimentally investigated and discussed for the suitable test conditions to provide an accurate OCV characterization by using the developed characterization system. This study extracted the OCVs from the pulse tests for different step-sizes. The step-size (ΔSOC) is set at 0.5%, 1%, 5%, and 10% under the same condition with 1C-rate 20°C and 10 min resting. ΔSOC means the step-size of the pulse tests between 0% and 100% of the SOC range. ΔSOC 1–5% means the variable step-size of the pulse tests, which gives a 1% step for the non-linear operating regions of 0–10% and 90–100% SOC ranges, and a 5% step for the linear region of 10–90% SOC range.

The tests were performed within the limits of the rated voltage between 3 V and 4.2V. The effect of step-sizes during pulse tests to the OCV characteristic is shown in Figure 4.1. ΔSOC 1% and 0.5% give the same OCV characteristic for all SOC ranges. ΔSOC 5% also gives the same OCV result for the SOC range between 10% and 90%. However, it gives an inconsistent OCV for the SOC ranges below 10% and above 90% (non-linear regions). The large step-size prominently affects to the OCV pattern in non-linear regions (windows A and C in Figure 4.1). Moreover, wide steps also cause the incomplete OCV measurement in a low SOC range (0%–10%), as illustrated by the blue and green dots in Window B of Figure 4.1b.

The 1% step-size is sufficient for OCV characterization for SOC ranges below 10% and above 90%, and the 5% step-size for the 10–90% SOC range. Figure 4.1 also shows the extracted OCVs for a step-size at ΔSOC 1–5%. ΔSOC 1–5% also gives a satisfactory OCV characteristic. Therefore, the ΔSOC 1–5% should be chosen to apply for all of our tests.

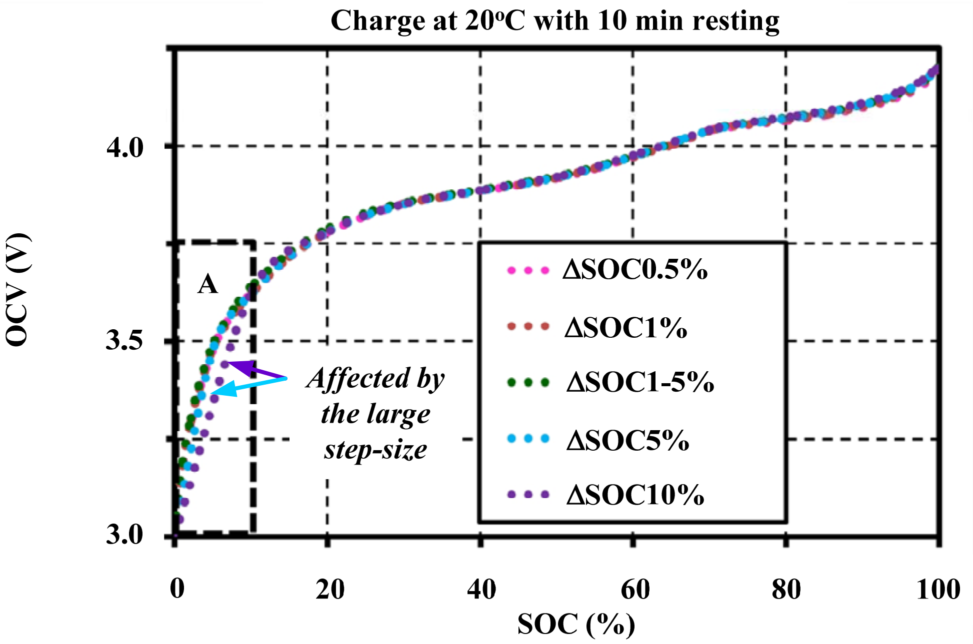

a) Under the charge test

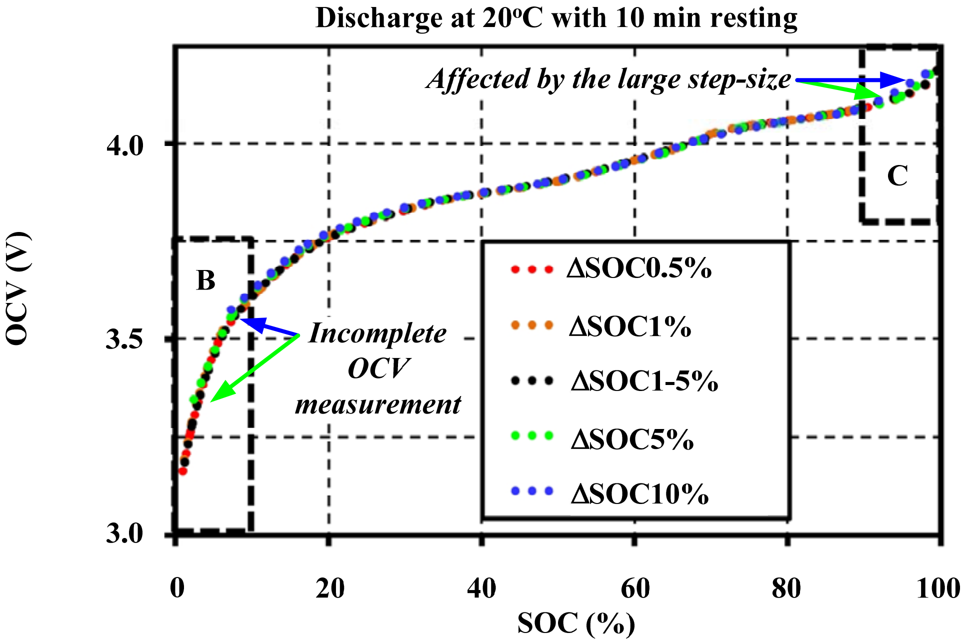

b) Under the discharge test

Figure 4.1 Effects of step-sizes during pulse tests on the OCV characteristic at 20 °C with 10 min resting.

4.2 Effect of resting period in the pulse test on the OCV characteristic

In order to study the effect of resting period of the cell in the pulse test, the slope percentage of relaxed voltage (%Slope$_{rv}$) for the cell was measured for each SOC step. The %Slope$_{rv}$ is calculated with Equation (4.1). The tests were performed for the different resting periods from 1 second to 3 hours to identify a suitable relaxation period for the OCV determination:

$$\%\mathrm{Slope}_{rv} = 100 \times \frac{\left(V_{SOC_i} - V_{SOC_{i-1}}\right)}{\left(t_{SOC_i} - t_{SOC_{i-1}}\right)} \tag{4.1}$$

Where

$V_{SOC_{i-1}}$ = Voltage at the starting of the relaxation state for each SOC

$t_{SOC_{i-1}}$ = Time at the starting of the relaxation state for each SOC

V_{SOC_i} = Voltage at the end of the relaxation state for each SOC

t_{SOC_i} = Time at the end of the relaxation state for each SOC

The slopes of the relaxed voltage versus the resting periods illustrated in Figure 4.2 show that the variation of voltage decayed down near zero after 1 min of resting. The slopes for all SOCs decayed down to zero at 60 min of resting. Therefore, the resting period should be evaluated between 1 min and 60 min to observe the influence on the extracted OCV.

Figure 4.3 shows the effect of resting periods on the extracted OCV under the same testing condition (at 1C-rate 20 °C with ΔSOC 1–5%). The low resting period gives a bloated OCV between 60% and 80% of SOCs, and cannot reflect the curly trends of OCV characteristic both on the charge and discharge operations. From the experiments, a recommended resting period for accurate OCV for this cell type is at

60 min to ensure that the cell has reached its equilibrium. However, it can be reduced to 30 min or 10 min for a fast OCV approximation.

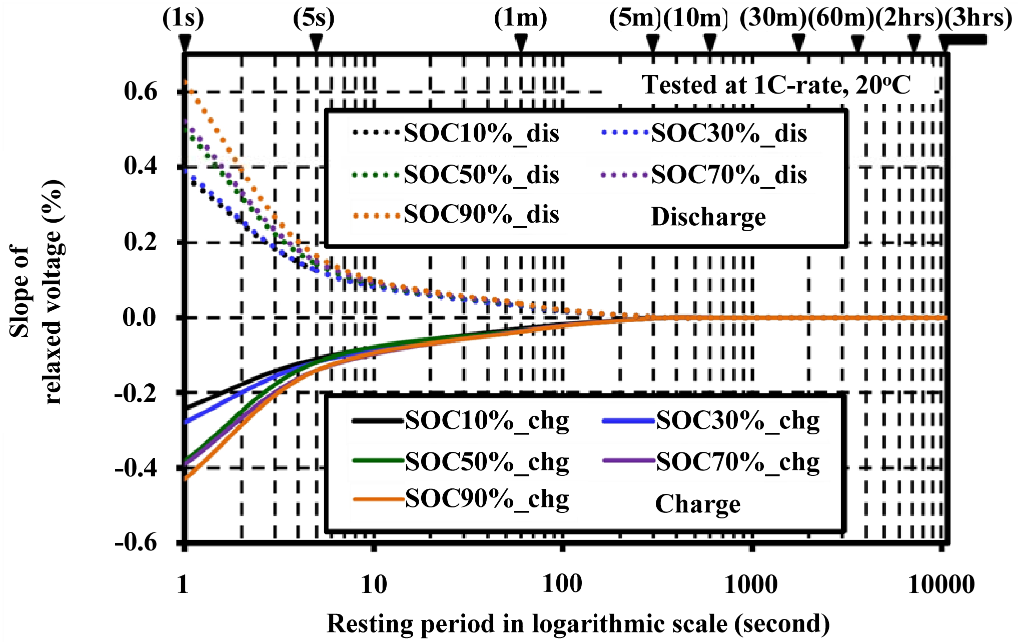

Figure 4.2 Slopes of the relaxed voltage versus the resting periods.

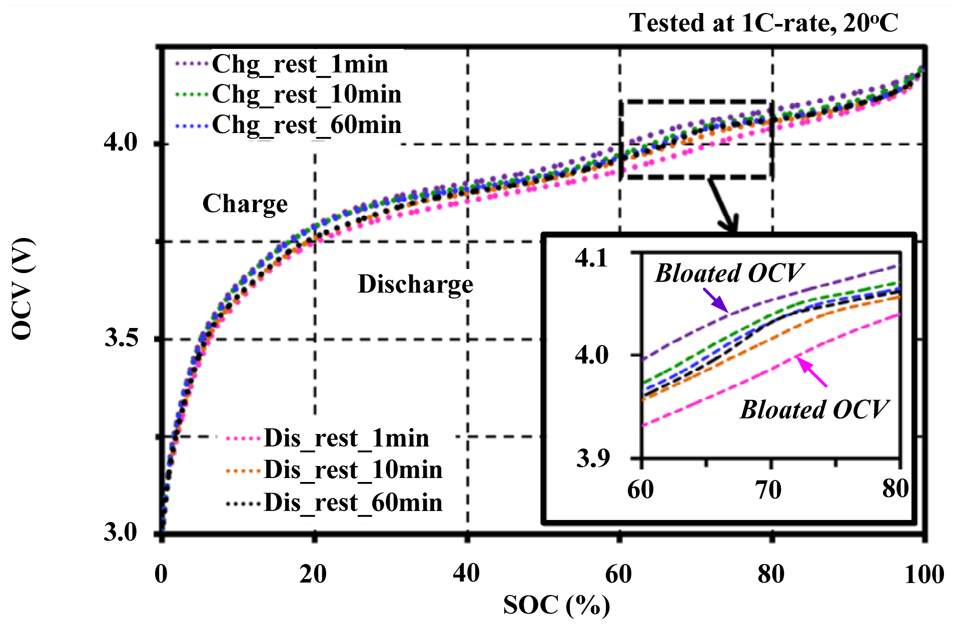

Figure 4.3 Effects of resting periods on the OCV characteristic.

4.3 Effect of SOC linearization range on the OCV approximation

This section characterizes the OCV as a function of the SOC in linear range. The tests are performed at constant pulse current 1C-rate at 20°C, and rested 60 min for each pulse by using the developed characterization system as described in Chapter 3.

Usually, the OCV has a non-linear relationship with the SOC. In this study, we ignore the OCV hysteresis effect by averaging the extracted OCVs for the charge and discharge. The purpose of this modeling is to simplify the OCV linearized model for a simple approximation, and to find the appropriate linear range for the BMS implementation.

The linearization ranges of SOC are divided into 20-80%, 20-90%, 15-95%, and 10-95% for evaluating the applicability and appropriate range for OCV linearized model, and considering the appropriate linear fitting range.

The residual sum of squares (RSS) between the measured OCV and linearized model for each range are evaluated as shown in Figure 4.4.

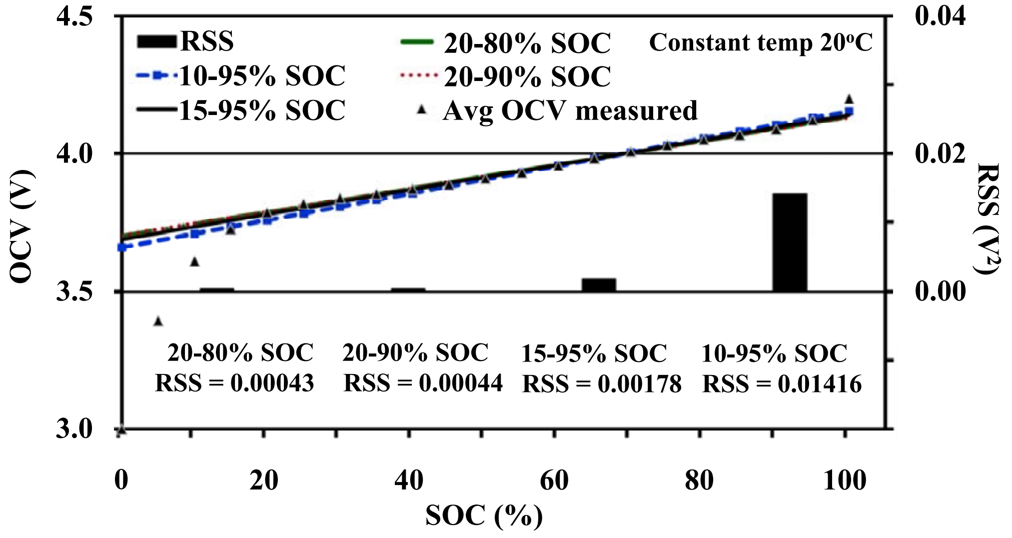

Figure 4.4 OCV characteristic under different linearization ranges of the SOC.

The appropriate SOC range for linearization is 15-95%. Because it gives the RSS only $0.00178V^2$, and the range is wide enough for observing the OCV response when compared with the widest range as 10-95%, which has the highest RSS of $0.01416V^2$. The linearized OCV model (OCV_L) of the 15-95% SOC range is shown in Equation (4.2).

$$\mathrm{OCV_L(SOC)} = (4.5036\times10^{-3})\,\mathrm{SOC} + 3.690 \tag{4.2}$$

4.4 Effect of current amplitude in the pulse test on the OCV characteristic

In order to investigate the effects of current amplitude (C-rate) on the OCV, the pulse charge and discharge tests were performed under the same testing condition (At 20°C with ΔSOC 1–5% and 60 min resting). The OCVs were extracted for different C-rates between C/4 and 1C. The effects of pulse current amplitudes on the OCV for the charge and discharge cannot be observed as shown in Figure 4.5.

The extracted OCVs with adequate relaxing period show that the voltage responses for the different C-rates correspond to both charge and discharge tests. It can be concluded that the pulse current amplitudes have no effect on the OCV characteristic under the constant temperature and same resting period.

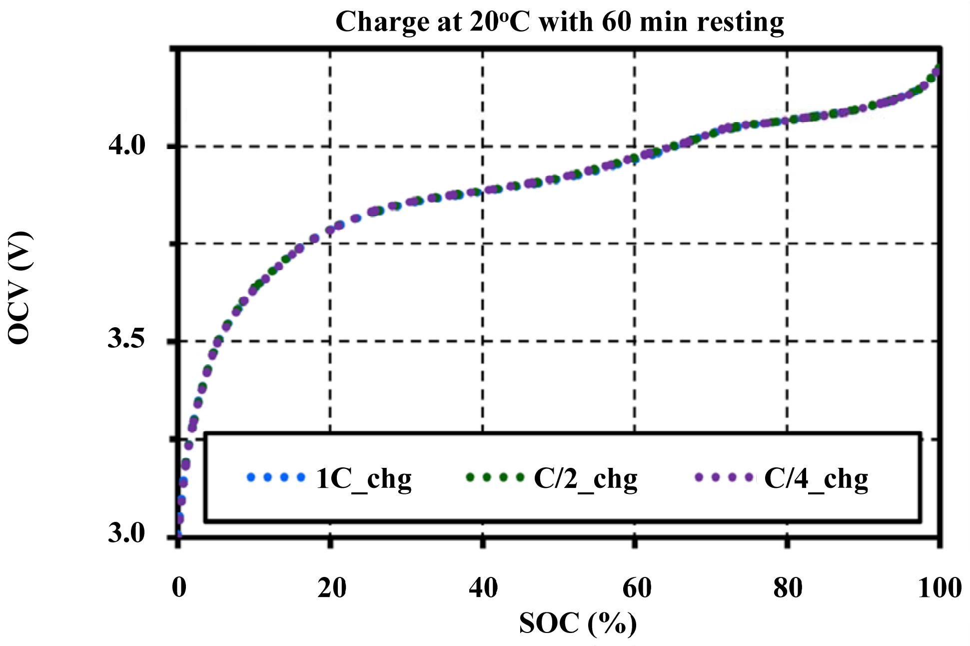

a) Under the charge test

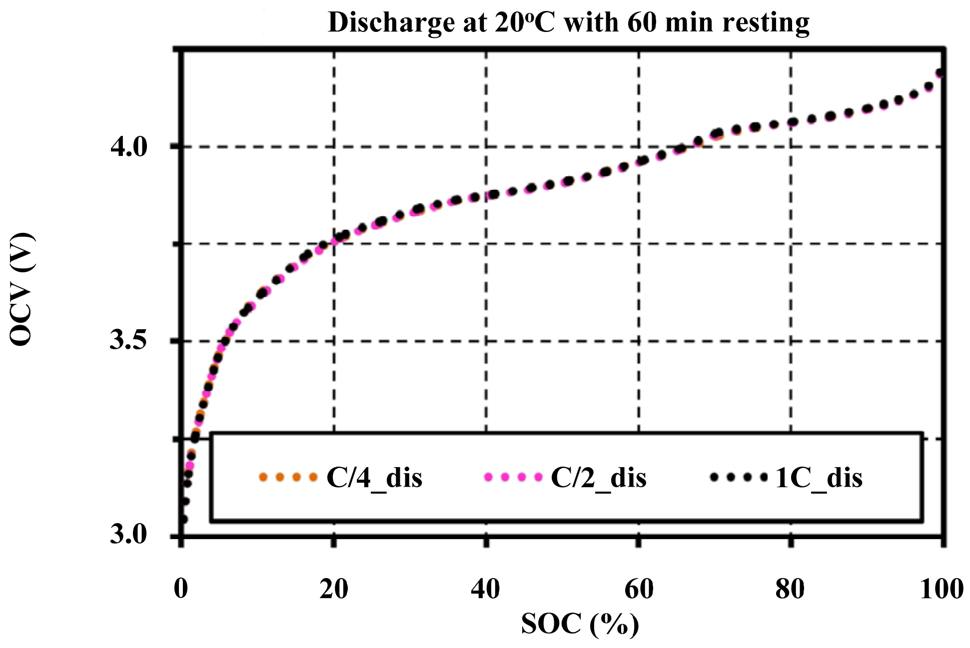

b) Under the discharge test

Figure 4.5 Effects of pulse current amplitudes on the OCV characteristic

4.5 Effect of hysteresis on the OCV characteristic

The hysteresis phenomenon in the LMO can be observed by applying the pulse charge and discharge tests in OCV characterization process, for the same testing condition (tested at 20°C with 60 min resting) as described in Section 4.2.

Figure 4.6 shows the OCV for charge (chg) and discharge (dis) with the different C-rates. A small hysteresis occurs in the range of 5–40% SOC for the charge and discharge, and it is magnified in Figure 4.7. It shows that the C-rates of the pulse tests also have no effect on the hysteresis character.

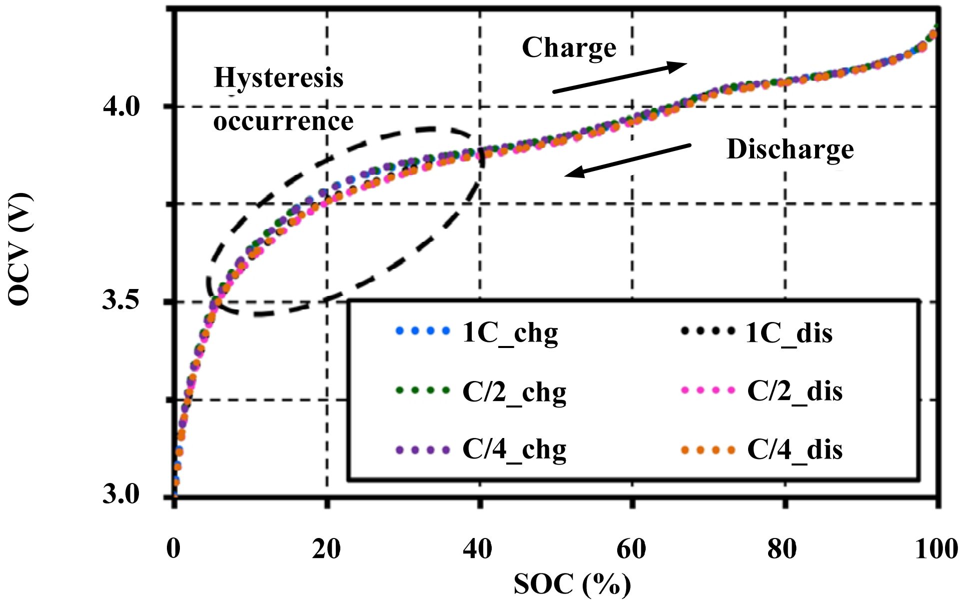

Figure 4.6 Hysteresis occurrence on the OCV characteristics.

The hysteresis, which results from mechanical stress, thermo-dynamical entropic effects and microscopic distortions within the active electrode material in Li-intercalation, is unique for each cell material [1]. The characterized OCVs illustrate that this cell type has a narrow hysteresis property between the charge and discharge.

The difference in OCV (ΔOCV) for the charge and discharge to the averaged values is shown in Figure 4.8. The maximum and minimum voltage gaps of the averaged OCV, which occurred at 25% SOC, are only ±14.368mV, or ±0.379% of the average value.

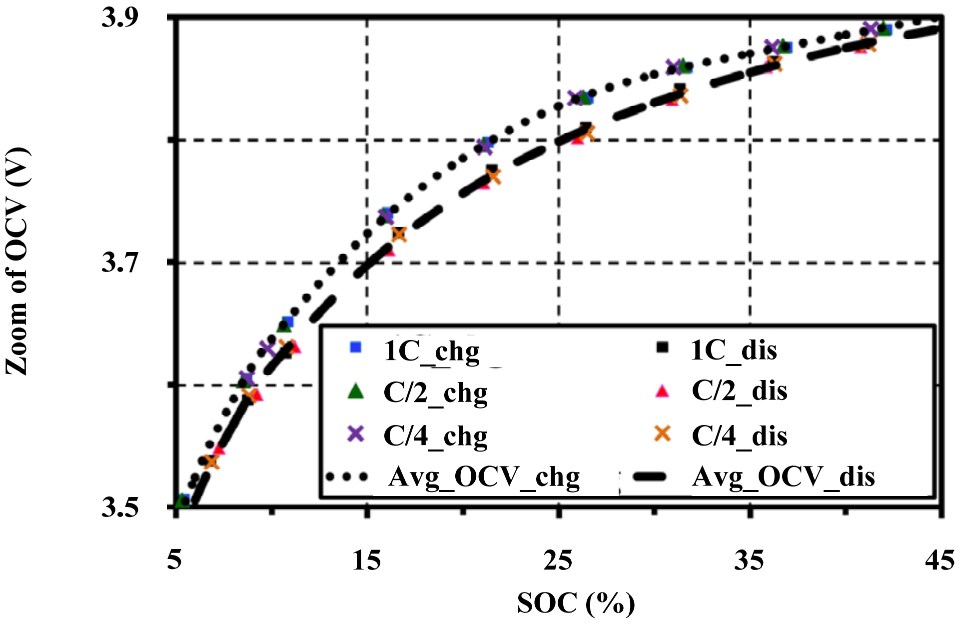

Figure 4.7 Zoom of the hysteresis occurrence.

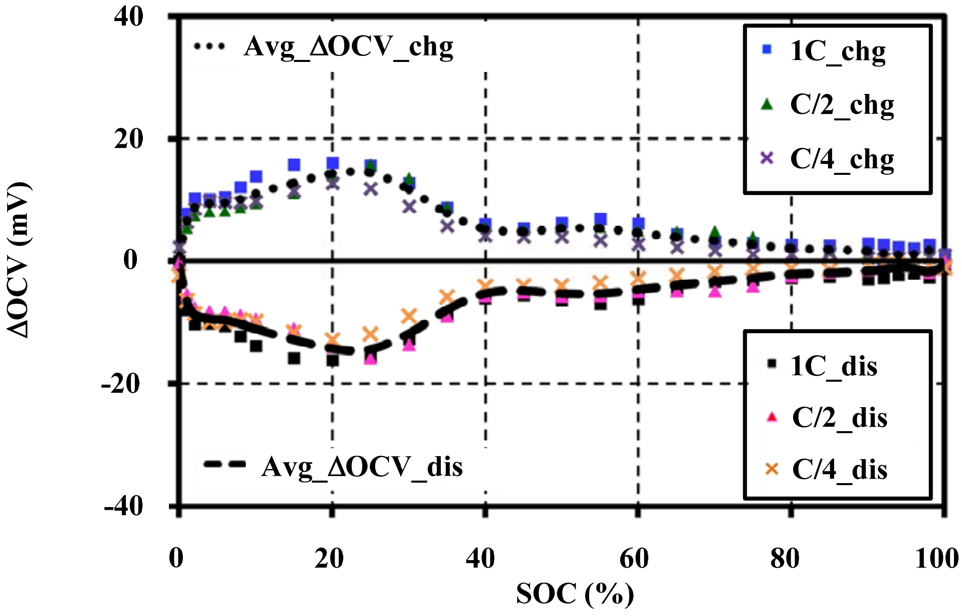

Figure 4.8 ΔOCV for the averaged charge and discharge values.

4.6 Effect of current amplitude on the ESR characteristic

The cell was prepared with the fully charged of standard condition, 1C-rate 20°C, following the CC-CV method as the initial condition for studying the effects of current amplitudes on the ESR characteristic. The pulse tests are performed, for the different C-rates between C/10 and 1C at 20°C with 60 min resting, by using the characterization system as described in Chapter 3. The ESR is calculated for the instantaneous response of voltage drop (V_{ESR}) with Equation (3.4). The effects of current amplitudes (C-rates) on the ESR characteristic are shown in Figure 4.9.

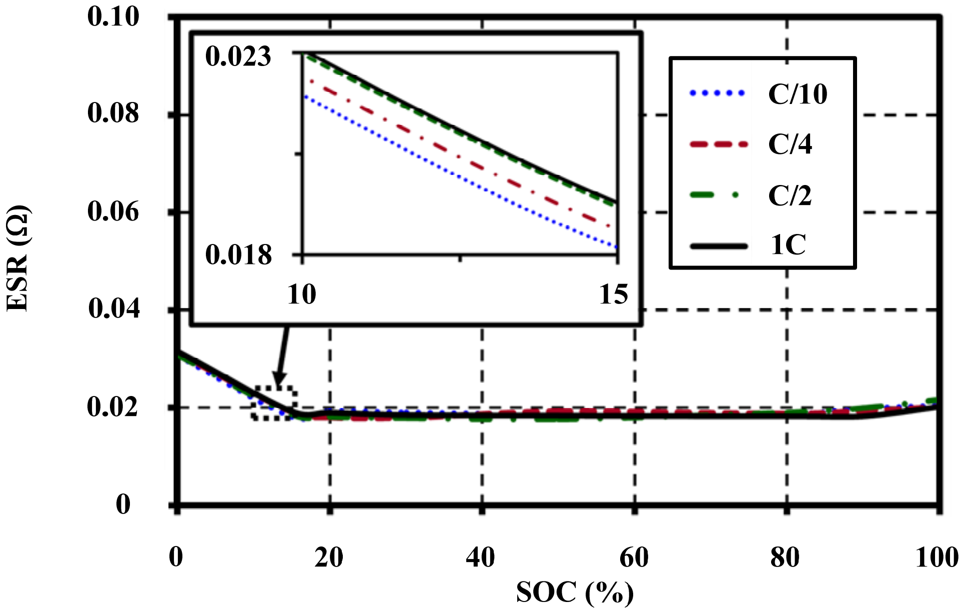

Figure 4.9 Effects of pulse current amplitudes on the ESR characteristic.

For the different C-rates, the resistance has no obvious difference in the SOC and C-rates, and almost constant in the range of 15-95% SOC. It can be concluded that the pulse current amplitudes have also no effect on the ESR characteristic under the constant temperature and same resting period.

4.7 Effect of temperature on the ESR characteristic

In order to study the effect of operating temperature on the ESR characteristic, the pulse charge and discharge tests are performed with the same standard testing condition at constant pulse current 1C-rate and 60 min resting. The operating temperatures are varied between 0°C and 40°C in the controlled temperature chamber. The ESR can also be obtained by Equation (3.4). The effects of temperatures on the ESR characteristic are illustrated in Figure 4.10.

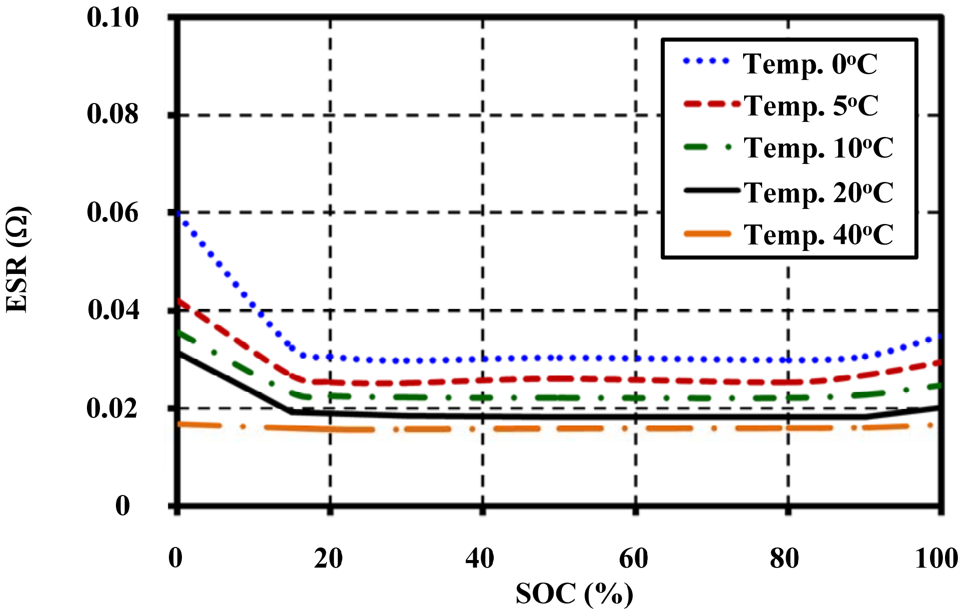

Figure 4.10 The effects of temperatures on the ESR characteristic.

Figure 4.10 shows a significant difference in ESR to temperatures. The resistance is constant along the SOC range of 15-95% irrespective of temperatures. However, for the SOC range below than 15%, the resistances significantly differ with the temperature. The ESR obviously increases with the decreasing temperature.

The effect of temperature on the ESR is explained as the ionic transition between electrodes via the electrolyte. The variation of internal resistances is ascribed by the change of ionic and electrical conductivities in the electrolyte. The effective phase-transition of the LMO reveals that the electrical conductivity has increased at room temperature and above temperature operations, and it will be decreased for a low temperature [2]. The high viscosity of electrolyte in the intercalation and de-intercalation for a low temperature makes Li-ions difficult to transport between the electrodes. This electrolyte resistance rise reflects on the increment of ESR. The relationship between the ESR (also FCTR) and ionic conductivity of the electrolyte under low temperature is also reported in [3].

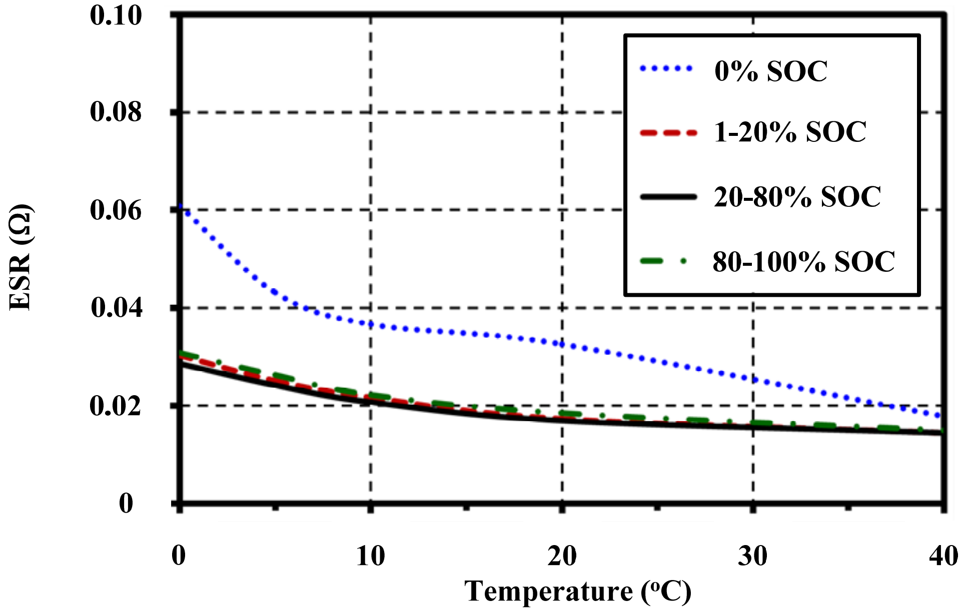

Figure 4.11 The relationship between ESR and operating temperature at different SOC ranges.

Figure 4.11 shows the relationship between ESR and operating temperature. The variation of resistance to temperature is low for the operating temperature higher than 10°C irrespective of the SOC. The ESR gradually increases with the decrement of temperature. The ESR for 0% SOC is obviously higher than the other SOCs, which can be explained in term of the end of discharge state, as well as in term of the start of charge state. These states are the most viscous for Li-ion movement during the intercalation resulting in high resistance. At the lowest temperature condition (0°C), the ESR for 0% SOC shows the increase by 1.66 times. The ESR model in a function of the operating temperature (T_0) at constant 1C-rate is approximated as Equation

(4.3) with the residual sum of squares (RSS), between the averaged ESRs and the model, of only $1.0709\times10^{-5}\ \Omega^2$.

$$\mathrm{ESR}(\mathrm{T}_0) \;=\; 2.75336\times10^{-2}\cdot e^{\left(-2.46976\times10^{-2}\right)\mathrm{T}_0} \tag{4.3}$$

4.8 Effect of current amplitude in continuous charge and discharge tests on the OCV Approximation

In this study, the continuous charge and discharge tests were performed with different current amplitudes (C-rates) between C/40 and 1C at 20 °C within the operating voltage ranges of the cell to study the influence of C-rates on the terminal voltage characteristics (VTs), and then to investigate the relationship between the VTs and OCV approximation.

The effects of C-rates on the terminal voltage characteristic are shown in Figure 4.12. The C-rates lower than C/20 do not obviously show the characteristic difference. However, the lower C-rates clearly illustrate the appearance of curly trends on both charge and discharge voltage profiles, especially between 60% and 80% SOCs as shown in Figure 4.12a and 4.12b, respectively.

Figure 4.13 shows the relationship between the average OCV and charge/discharge terminal voltages under different C-rates. Figure 4.13a shows that the VTs for low C-rates close to the average OCV. The polarization voltage gaps between the charge and discharge VTs can be reduced for the low C-rate. The polarization of the VTs is directly influenced by the C-rate. The cell operating at the larger current presents more polarization effects.

As aforementioned in Section 4.4 and 4.6, the OCVs and ESRs for each charging and discharging do not change with the C-rates. Therefore, the voltage drops across the ESR depend on the applying currents, resulting in the change of the terminal voltage. It can be recommended that the OCV characteristic can be approximated by measuring a terminal voltage at the low testing current.

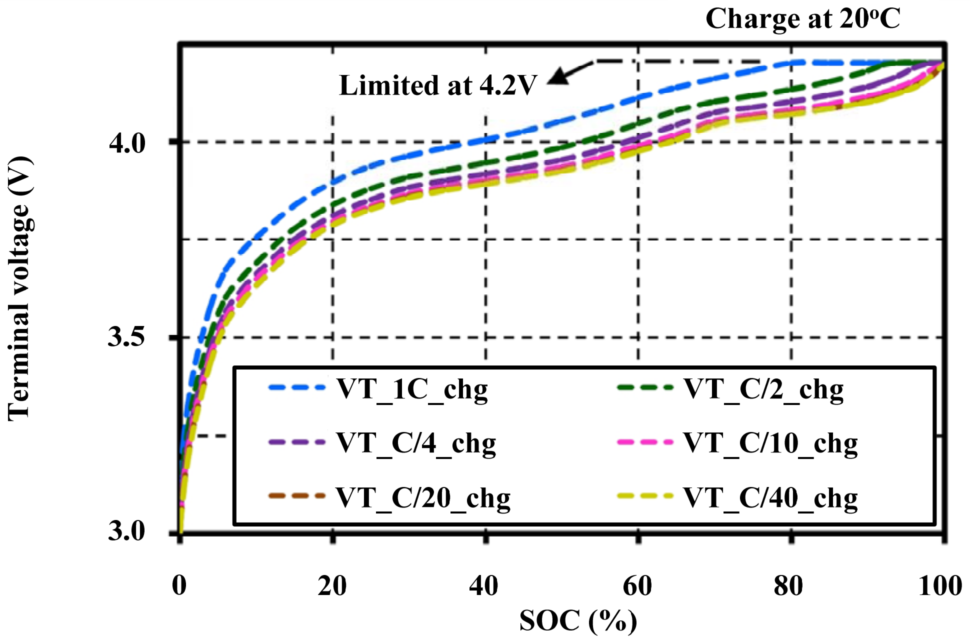

a) Under continuous charging

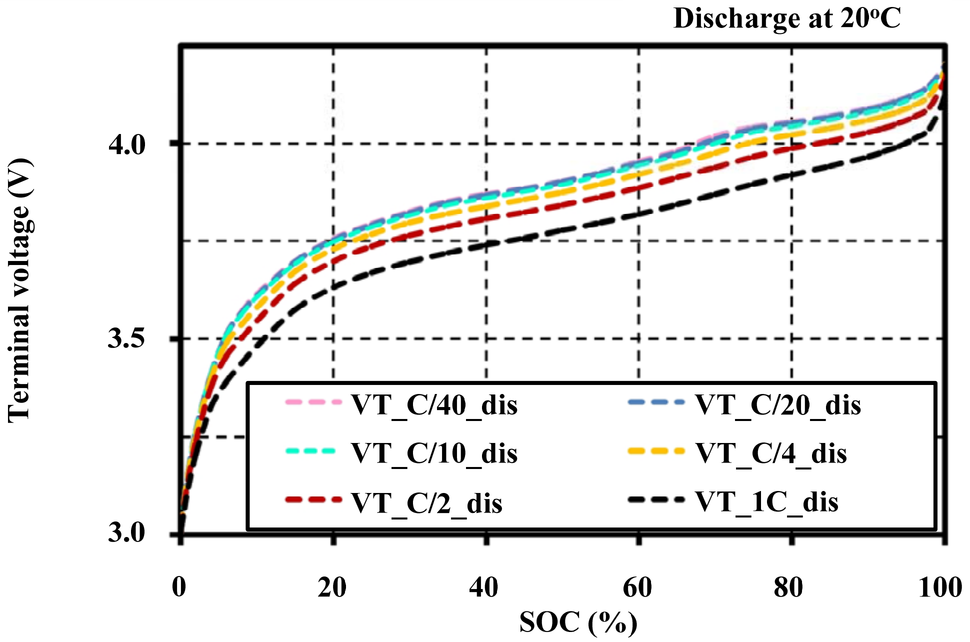

b) Under continuous discharging

Figure 4.12 Effects of current amplitudes on the terminal voltage characteristic.

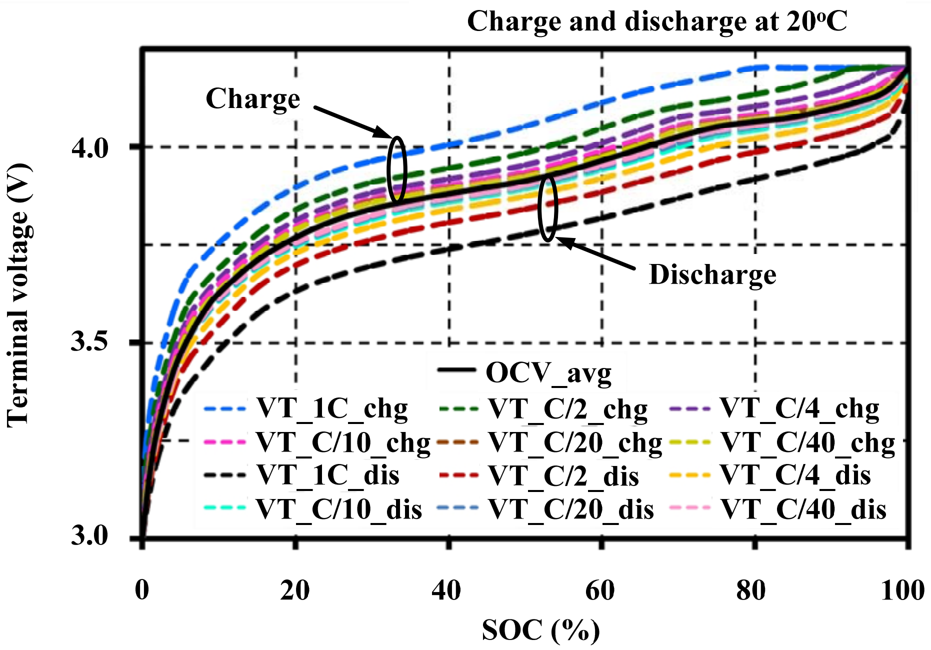

a) Polarization differences of terminal voltages under different rates of continuous testing current on the average OCV.

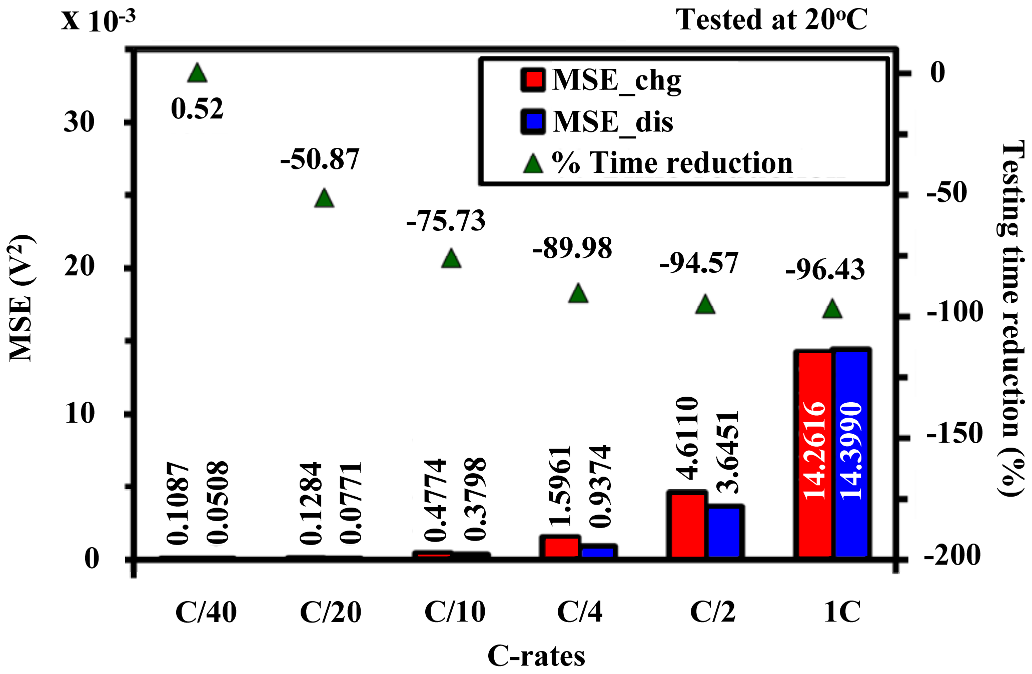

b) Mean of the squared residuals of errors (MSE) and testing time reduction for OCV approximation under different rates of continuous testing current.

Figure 4.13 Terminal voltage relationships to the OCV approximation.

Figure 4.13b shows the mean of the squared residuals of errors ($MSE_{C\text{-rate}}$) between the OCV and terminal voltage for each C-rate of Figure 4.13a, and shows a testing time reduction for the OCV approximation under different rates of continuous testing current. The $MSE_{C\text{-rate}}$ is calculated separately for the charge and discharge by using Equation (4.4):

$$MSE_{C-rate} = \frac{1}{n}\sum_{SOC_{i=1}}^{SOC_n}\left(VT_{SOC_i} - OCV\left(SOC_i\right)\right)^2 \tag{4.4}$$

Where

VT_{SOC_i} = Measured terminal voltage at SOC_i for a continuous test

$OCV(SOC)_i$ = Open-circuit-voltage obtained by OCV averaging at the different C-rates as a function of SOC_i for a sampling number n separately for charge and discharge

A recommended continuous testing current rate for the OCV approximation is C/20 because it can save time for charge and discharge tests, compared with the OCV pulse test method at 1C-rate, from 82.86 h to 40.71 h (or 50.87%) with low MSEs of only $0.1284\times10^{-3}V^2$ and $0.0771\times10^{-3}\ V^2$ for the charge and discharge, respectively. Moreover, it is also faster than the C/40 rate by 51.39% with the difference of MSEs of only $0.0197\times10^{-3}V^2$ and $0.0263\times10^{-3}\ V^2$ for the charge and discharge, respectively.

4.9 Effects of current amplitudes and temperatures on the capacity characteristic

In this section, the capacity characteristics of the LMO are analyzed and evaluated. The test parameters as C-rates and operating temperatures are used for evaluating the operational and environmental conditions. They are from C/2 to 5C-rates and from 0°C to 40°C, respectively. The characterization system as described in Chapter 3 is used for the tests. The tests are performed by discharging a fully charged cell, which is limited by the voltage rating of the cell from 4.20V to 3.00V.

The battery capacities are calculated based on the cumulative currents of battery using Equation (3.3). The capacity deterioration of the battery is evaluated, to study the characteristic changes under various operating temperatures and current amplitudes (C-rates), as shown in Equation (4.5).

$$Q_D = \left(\left(Q_B - Q_{RATED}\right)/Q_{RATED}\right)\times 100 \tag{4.5}$$

Where

Q_D = Capacity deterioration by operation (%)

Q_B = Accumulated battery capacity (Ah)

Q_{RATED} = Rated capacity of the battery (Ah)

The effects of C-rates on the accumulated capacity of the cell under various temperatures are illustrated in Figure 4.14.

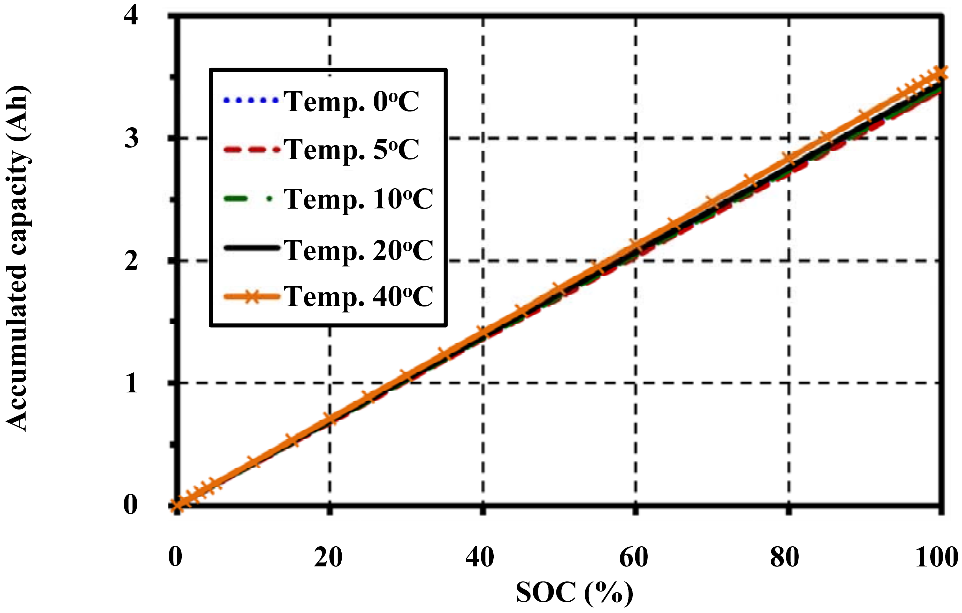

(a) At C/2-rate

Figure 4.14 Effects of incremental C-rates on the accumulated capacity of the cell under various temperatures.

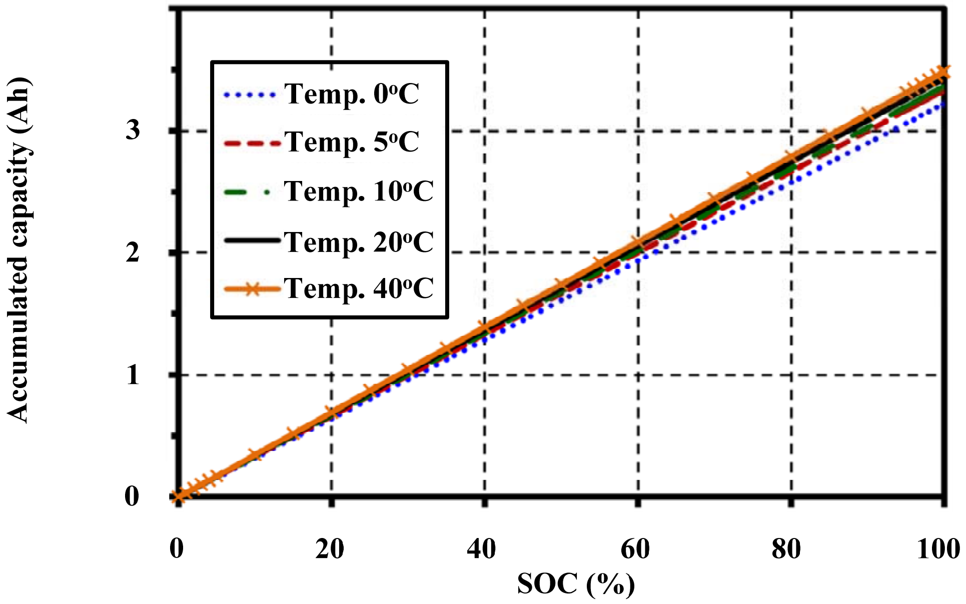

(b) At 1C-rate

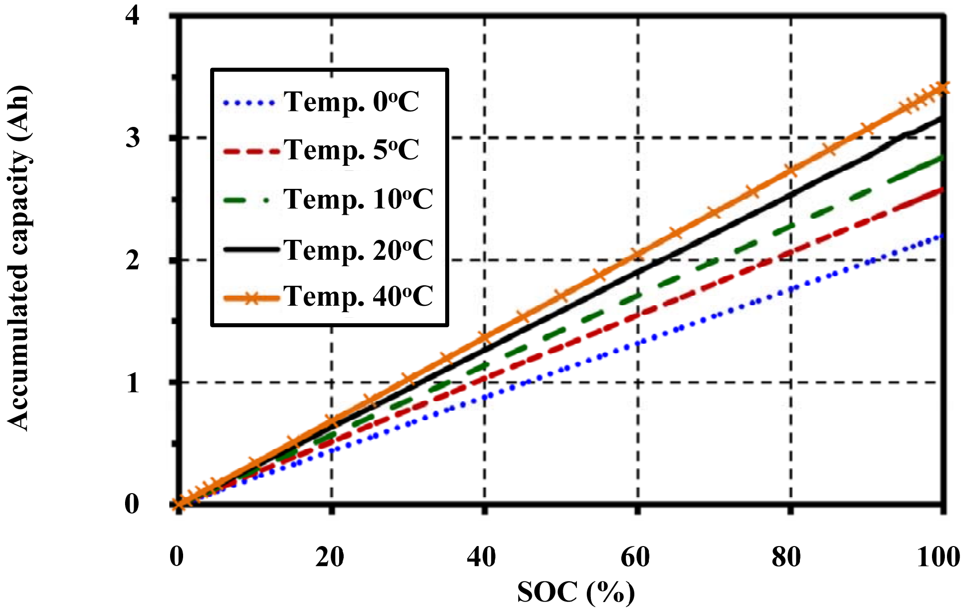

(c) At 3C-rate

Figure 4.14 (Cont.) Effects of incremental C-rates on the accumulated capacity of the cell under various temperatures.

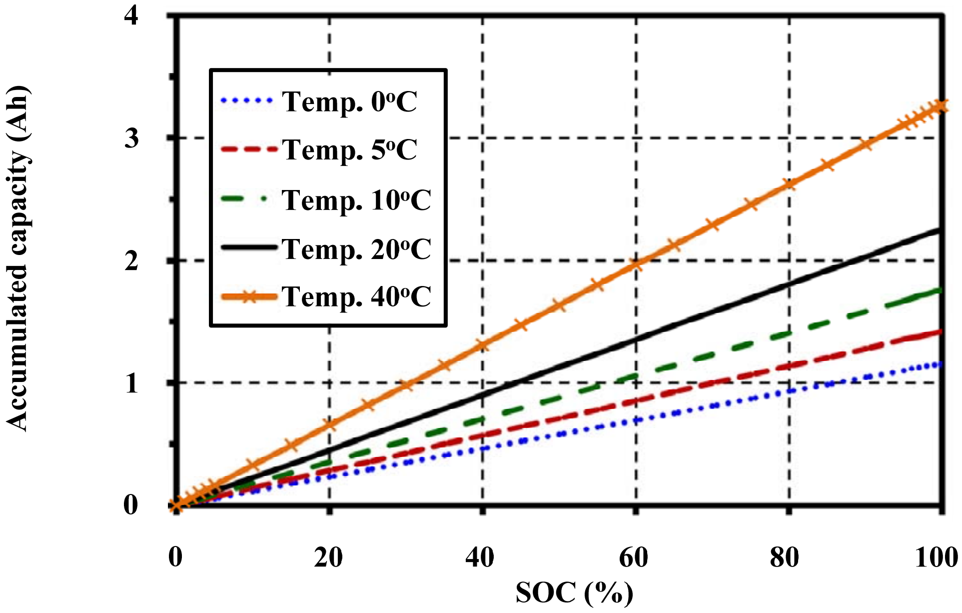

(d) At 5C-rate.

Figure 4.14 (Cont.) Effects of incremental C-rates on the accumulated capacity of the cell under various temperatures.

From Figure 4.14, all cell capacities have a linear relationship for each C-rate of the discharge continuous constant current. The operating temperature does not obviously affect on the cell capacity for low C-rate as shown in Figure 4.14a. However, the reduction of capacity is obvious for the large C-rate and low temperature as shown in Figure 4.14b-4.14d, respectively.

The effects of temperatures on the accumulated capacity of the cell under various C-rates are shown in Figure 4.15, and the effects of C-rates on the capacity deterioration of the cell under various temperatures are shown in Figure 4.16. The investigation of capacity deterioration for the cycling cells is far from the scope in this section. However, the details of cycling investigation will be explained in Chapter 6.

The capacity is not affected by the operating temperatures under low discharge rates as shown in Figure 4.15. However, the cell capacity drops with the low temperature for high discharging rates. These characteristics can be explained by the electrochemical reaction inside the battery. The electrolyte resistance is high for low temperature due to the low ionic conductivity in the electrolyte, and low transportation rate of Li-ions between electrodes in the electrolyte [4].

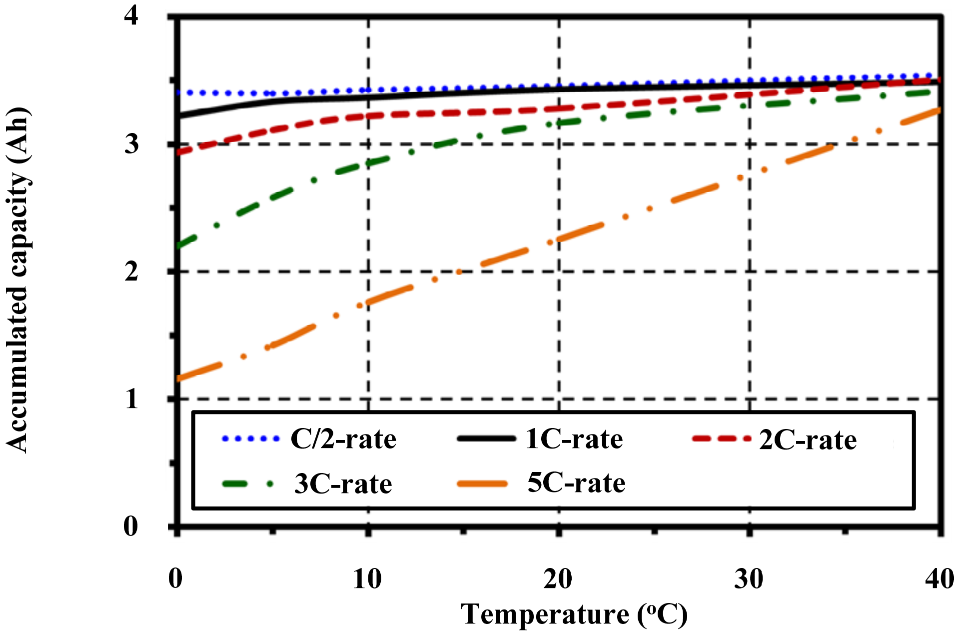

Figure 4.15 Effects of temperatures on the accumulated capacity of the cell under various C-rates.

Next, we consider the effects of high C-rates on the effective capacity for operations with a constant temperature. The exceeding Li-ion may temporarily accumulate on the surface of electrode when the Li-ion transportation rate increases and exceeds the rate that Li-ion can be fully intercalated into the intercalation layers [5]. The abilities of releasing and insertion of Li-ions between the electrodes are reduced for the operation under low temperature and high C-rate conditions, and results in a significant deterioration of the battery capacities. The experimental results in Figure 4.16 indicate all of these phenomena as abovementioned. The maximum capacity deterioration of this LMO occurring at the highest C-rate and lowest temperature (5C-rate, 0°C) that is 68.87%. These results led us understand the effects of the operational and environmental conditions on the cell capacity deterioration.

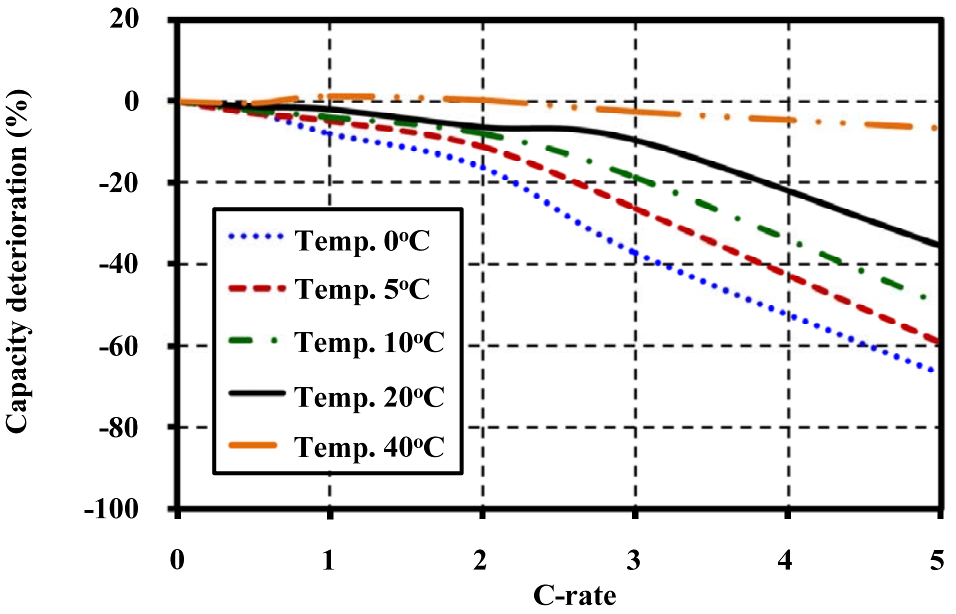

Figure 4.16 Effects of C-rates on the capacity deterioration of the cell under various temperatures.

4.10 Chapter summary

In this chapter, the adjusting factors that affect the battery characteristics were studied. The accurate OCV for the LMO can be obtained with a small step-size pulse of 1% for the non-linear regions below 10% and above 90% SOCs. The step-size can be increased up to 5% in the range of 10%–90% SOC for faster extraction with a small error. The short resting period of the pulse test directly affects the error of the OCV estimation. A recommended resting period for accurate OCV on this battery type is 60 min. The accurate OCV can be directly measured at terminals of the battery after energizing constant pulse currents and taking a rest at 60 min for each pulse to recover the battery close to its equilibrium. Between the charge and discharge, a hysteresis of this studied cell has the maximum voltage gap of only 28.738 mV at 25% SOC. The measuring of terminal voltage (VT) of the cell under the low C-rate of C/20 can illustrate the approximate OCV characteristic with acceptable MSE value by using only half the time for testing. It also found that the OCV and ESR are insensitive with the current rates (C-rate) of the pulse tests under a constant temperature. The ESR increases when the operating temperature decreases, especially at low SOC. The ESR for 0% SOC increases by 1.66 times than the other SOC ranges under low temperature condition as 0^{o}C. It is also found that the low temperature largely deteriorates the cell capacity. The cell capability, which is an ability of the cell to store the lithiums, is dropped under the low temperature condition. In this condition, the viscosity of electrolyte has increased that caused a reduction of the ionic conductivity, and reflected in the increment of ESR. The battery considerably deteriorates whenever operating at low temperature and large current conditions.

4.11 References

[1] M.A. Roscher, O. Bohlen, and J. Vetter, “OCV hysteresis in Li-ion batteries including two-phase transition materials”, Int. J. Electrochem., Vol. (2011), pp. 1-6, 2011.

[2] M. Parka, X. Zhanga, M. Chunga, G. B. Lessa, and A. M. Sastry, “A review of conduction phenomena in Li-ion batteries”, J. Power sources, Vol.195(24), pp.7904-7929, 2010.

[3] S.S. Zhang, K. Xu, and T.R. Jow, “The low temperature performance of Li-ion batteries”, J. Power sources, Vol.115, pp.137-140, 2003.

[4] M.A. Roscher, J. Assfalg, and O. S. Bohlen, “Detection of utilizable capacity deterioration in battery systems”, IEEE Trans. On Vehicular Technology, Vol. 60(1), pp.98-103, 2011.

[5]. K. Eberman, P. Gomadam, G. Jain, and E. Scott, “Material and design options for avoiding Lithium plating during charging”, ECS Transactions, Vol. 25(35), pp.47-58, 2010.

Chapter 5

Parameter Identification and Modeling of the LMO

This chapter shows the method and procedure for parameter identification of the LMO model based on the experiment of transient responses. The preparation for battery model parameter identification is introduced. The LMO modeling with testing data and the verification method are also proposed.

5.1 Preparation of parameter identification

The procedure for the parameter identification is started from a cell preparation by full charging then following with the pulse discharging at a standard condition. For the full charging, the cell is prepared by applying a charging at 1C-rate in CC-CV mode (3.5A and 4.2V) with the ambient temperature controlling at 20^{o}C using the charge system proposed in Chapter 3. The precise pulse discharge tests are then performed at a standard testing condition by applying the periodic constant current, 1C-rate (3.5A), using the developed programmable discharge system as mentioned in Chapter 3 to identify the model parameters, The conditions for the pulse tests are set at 1–5% step-size (ΔSOC) and 60 min of resting period as summarized in Chapter 4.

The steps of pulse test are precisely divided into 3 steps as follows:

- The first step is 10 shots of 0.6 min with 1C-rate pulse discharge, for a high range of the SOC from 100% to 90%, and the respective pulse deserves as 1% SOC reduction.
- The second step is 16 shots of 3 min with 1C-rate pulse discharge, for a medium range of the SOC from 90% to 10%, and the respective pulse deserves as 5% SOC reduction.
- The last step is 10 shots of 0.6 min with 1C-rate pulse discharge, for a low range of the SOC below 10%, and the respective pulse deserves as 1% SOC reduction.

The battery voltage response of the pulse discharge tests for parameter identification, obtained from the characterization system as mentioned in Chapter 3, are shown in Figure 5.1.

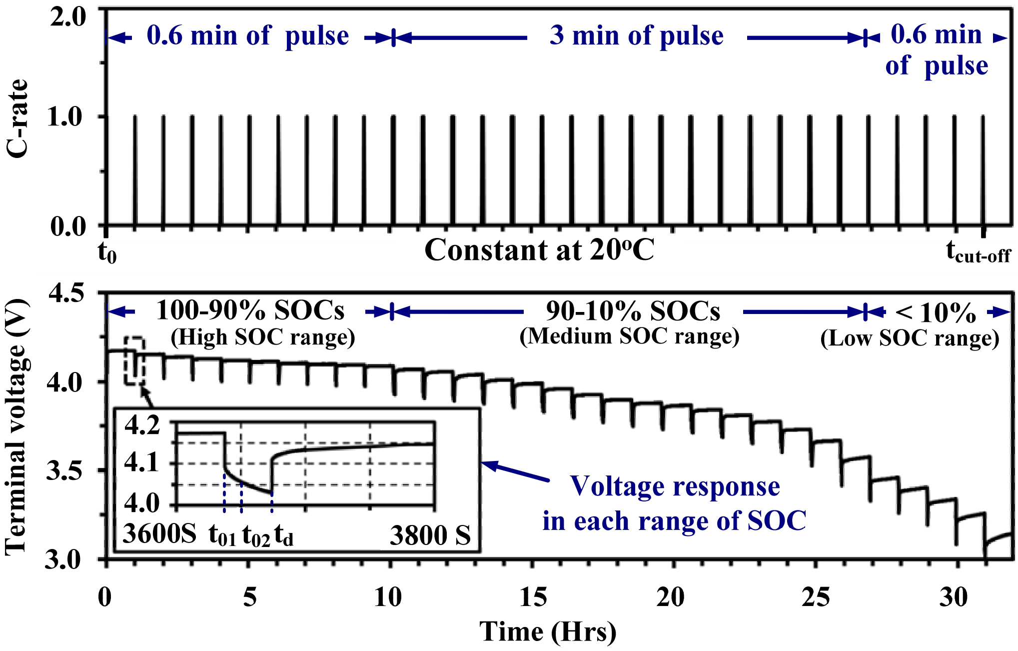

Figure 5.1 Battery voltage responses of the pulse discharge tests for parameter identification.

The pulse tests are started from the rated full charged voltage (4.2V), and continued until the voltage at terminals undergoes the rated discharge cut-off voltage (DCV) at 3V. During the test, the ambient temperature of the cell is controlled at 20°C for the standard condition. At the end of each pulse, the cell has rested for 60 min for relaxing the cell voltage to its equilibrium condition.

5.2 OCV modeling

A model of the OCV characteristic in LIBs is essential for the BMS in order to estimate the state variables during operations, and for investigating of battery electrode properties. Many OCV models of the batteries have been proposed [1,2]. They are related to the internal chemical variation of the batteries to fit with the tested results, depending on the purpose of the study and their applications.

The factors that affected the OCV are studied in the previous section, and the step-size of the pulse test and resting period are adjusted to obtain the accurate OCV. At the same time, we also found that the rates of the testing current (C-rates) have no effect on the OCV. The precise OCV from the experiments under these conditions is obtained as the averaged OCV to the respective C-rates separately in the charge and discharge. A simplified OCV model for the LMO is developed as a function of SOC, and then it is validated with the experimental OCV data.

The empirical high-order polynomial is used to implement the model for a real-time calculation in the BMS application, as shown in Equation (5.1):

$$\mathrm{OCV(SOC)} = \sum_{j=0}^{n} \left(k_j \mathrm{SOC}^j \right) \tag{5.1}$$

The coefficients (k_j) in Equation (5.1) are determined with MATLAB for the experimental SOC and OCV data from the previous section by using a non-linear least square estimation technique.

The objective function is given as in Equation (5.2):

$$\min_{k} \left\| f(k,SOC) - OCV_E \right\|^2 = \min_{k} \sum_{i=1}^{m} \left[f(k,SOC_i) - OCV_{Ei} \right]^2 \tag{5.2}$$

Where

k = SOC coefficient to be optimized

j = Degree of polynomial

OCV_E = Extracted OCV

f = Function for the objective equation

n = Highest-order of polynomial

m = Number of SOC and OCV data

From Equation (5.1), the highest-order (n) for smooth fitting of the OCV analytic function for this LMO is 17th for both charging and discharging. For this order, the MSEs are less than the maximum criteria ($\leq 1 \times 10^{-5}$ V^2) that is precise enough for fitting the OCV model. The optimum SOC coefficients of the OCV model for charge and discharge are shown in Table 5.1.

Table 5.1 Optimum SOC coefficients of the OCV model for charge and discharge.

SOC coefficient	Charge	Discharge	SOC coefficient	Charge	Discharge
k_0	3.0037	3.0016	k_9	1.0595×10^{-9}	8.4261×10^{-10}
k_1	2.3163×10^{-1}	2.0082×10^{-1}	k_{10}	-2.2638×10^{-11}	-1.8003×10^{-11}
k_2	-6.5271×10^{-2}	-5.0440×10^{-2}	k_{11}	3.6337×10^{-13}	2.8847×10^{-13}
k_3	1.4950×10^{-2}	1.1287×10^{-2}	k_{12}	-4.3564×10^{-15}	-3.4474×10^{-15}
k_4	-2.3529×10^{-3}	-1.7962×10^{-3}	k_{13}	3.8402×10^{-17}	3.0257×10^{-17}
k_5	2.5025×10^{-4}	1.9382×10^{-4}	k_{14}	-2.4147×10^{-19}	-1.8926×10^{-19}
k_6	-1.8436×10^{-5}	-1.4444×10^{-5}	k_{15}	1.0246×10^{-21}	7.9827×10^{-22}
k_7	9.6864×10^{-7}	7.6498×10^{-7}	k_{16}	-2.6280×10^{-24}	-2.0344×10^{-24}
k_8	-3.7174×10^{-8}	-2.9500×10^{-8}	k_{17}	3.0772×10^{-27}	2.3659×10^{-27}

The extracted OCV models are shown by the solid line in Figure 5.2. It shows that the proposed OCV model can illustrate the voltage characteristics correctly along the SOC range on both charge and discharge operations separately by the hysteresis phenomena.

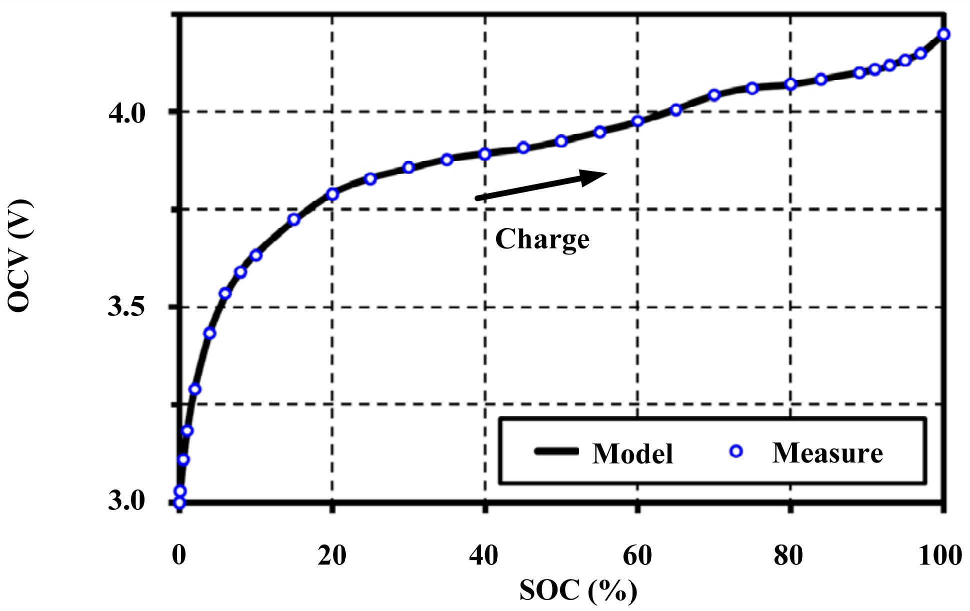

a) Fitting result for charging

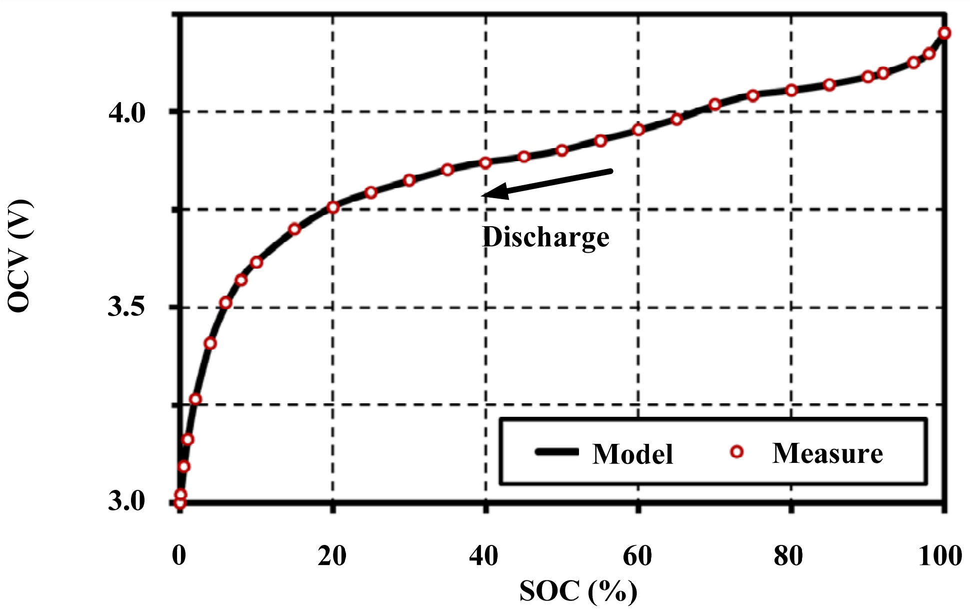

b) Fitting result for discharging

Figure 5.2 OCV fitting results for the LMO at 20°C.

A comparison of the MSEs and errors of estimation at different polynomial orders for OCV model is shown in Figure 5.3.

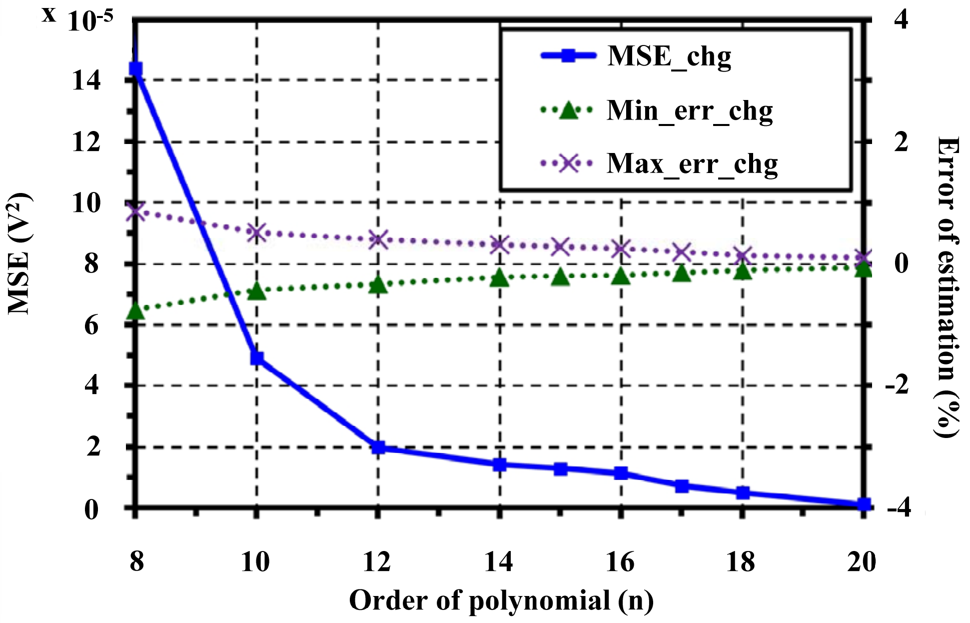

a) Results for charge

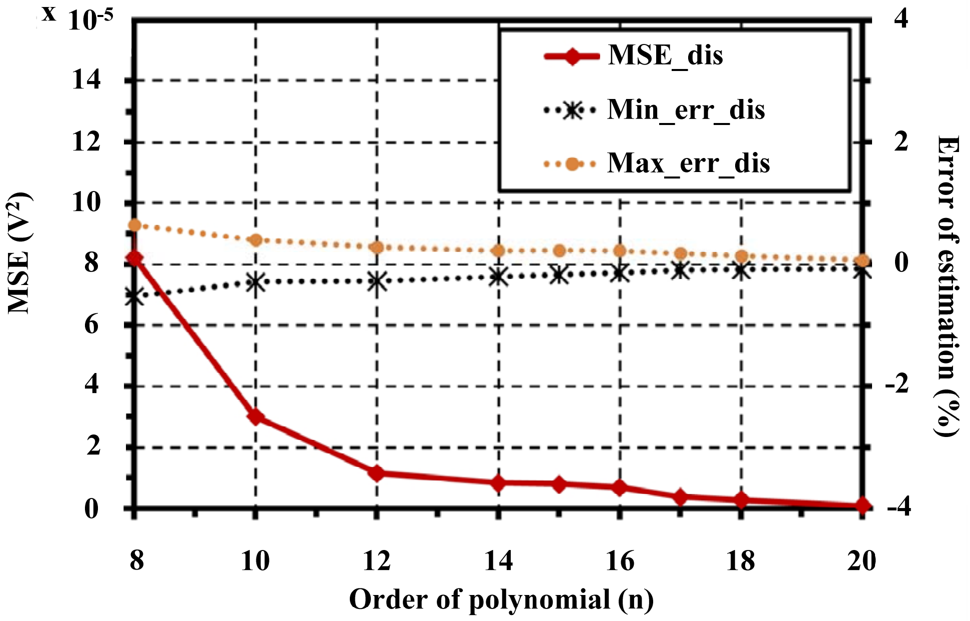

b) Results for discharge

Figure 5.3 Comparison results of MSEs and errors of estimation at different polynomial orders.

The errors of OCV model are evaluated in Figure 5.4 by means of squared residuals of the errors (MSEs).

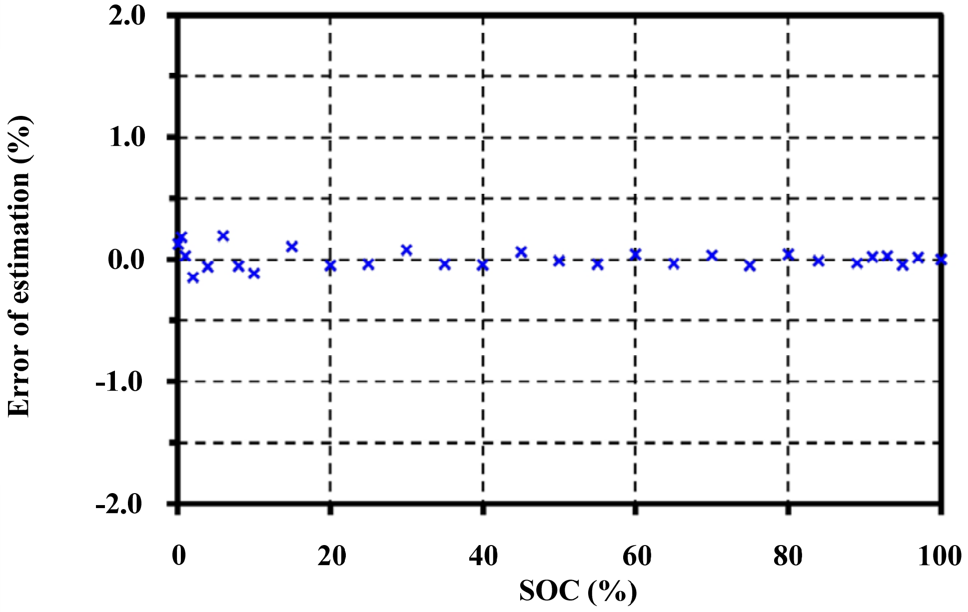

a) Error of estimation for charge

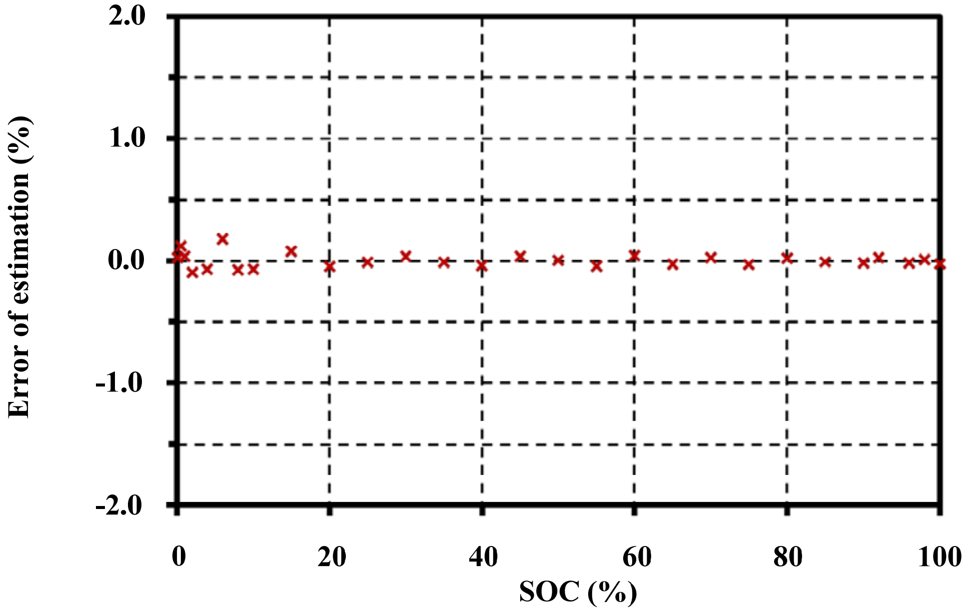

b) Error of estimation for discharge

Figure 5.4 The error evaluation for OCV model validation of the LMO at 20°C

The MSEs for charging and discharging are only 0.7414 × 10^{-5} V^2 and 0.3848 × 10^{-5} V^2, respectively. The minimum, maximum, and average values of the estimation error for charge are −4.7265 × 10^{-3} V, 6.9326 × 10^{-3} V, and 7.8056 × 10^{-8} V (or −0.1437%, 0.1961%, and 0.00008%), respectively, while the minimum, maximum, and average values of the estimation error for discharge are −3.0394 × 10^{-3} V, 6.3308 × 10^{-3} V, and 1.1389 × 10^{-7} V (or −0.0931%, 0.1802%, and 0.00004%), respectively.

5.3 Parameter identification method

The battery parameters for the transient response model shown in Figure 2.2 are identified by Equations (5.3) to (5.6). Equation (5.3) gives the voltage drop summation inside the battery. Equation (5.4) is used to calculate the equivalent bulk resistance after immediate applying the discharge pulse from instantaneous response. Equations (5.5) and (5.6) are the solution for the differential equations of RC parallel circuits.

$$V_{T_i} = OCV_i - V_{ESR\,i} - V_{1_i} - V_{2_i} \tag{5.3}$$

$$ESR_i = V_{ESR\,i} / I_{B_i} \tag{5.4}$$

$$V_{1_i} = I_{B_i} R_{1_i} (e^{-(t-t_{01i})/\tau_{1_i}}) \tag{5.5}$$

$$V_{2_i} = I_{B_i} R_{2_i} (e^{-(t-t_{02i})/\tau_{2_i}}) \tag{5.6}$$

Where

i = Experiment number for each SOC reduction

$V_{T\,i}$ = Terminal voltage (V)

$I_{B\,i}$ = Battery current (A)

ESR_i = Effective series resistances (Ω)

R_{1_i} = Faradic charge-transfer resistance (Ω)

R_{2_i} = Ionic diffusion resistance (Ω)

OCV_i = Open circuit voltage as a function of the SOC (V)

t_{01_i} and t_{02_i} = Initial time (sec) of V_{1_i} and V_{2_i} from the experiment

V_{ESR_i} = Voltage drop (V) across the ESR_i at definite time t_{01_i}

V_{1_i} and V_{2_i} = Voltage drop (V) across the R_{1_i} and R_{2_i} at definite time t_{01_i} to t_{02_i} and t_{02_i} to t_{d_i} (sec), respectively

τ_{1_i} = Short-term time constant (sec), which reflects the transient response of faradic charge-transfer resistance and its related double-layer capacitance [3] ($\tau_{1_i} = R_{1_i} C_{1_i}$)

τ_{2_i} = Long-term time constant (sec), which reflects the transient response of diffusion phenomenon ($\tau_{2_i} = R_{2_i} C_{2_i}$)

The proposed parameter identification method is based on the method from [3], which only tested and identified the parameters at 50% of SOC. However, the tested ranges of the SOC in this research are divided into 3 regions as abovementioned. The parameters of ESR, R_1, R_2, C_1 and C_2 are identified from the tested responses.

Calculation steps for parameter identification based on the experiment of transient responses are illustrated in the flowchart of Figure 5.5 for each SOC range. The parameters were identified for each pulse step until the OCV undergoes the discharge cut voltage level of 3V (DCV). The average values of the identified parameters ESR, R_1, R_2, C_1, and C_2 are 20.489 $m\Omega$, 4.334 $m\Omega$, 13.622 $m\Omega$, 9.527 F and 1,432.422 F respectively. All parameters will be validated in the next section.

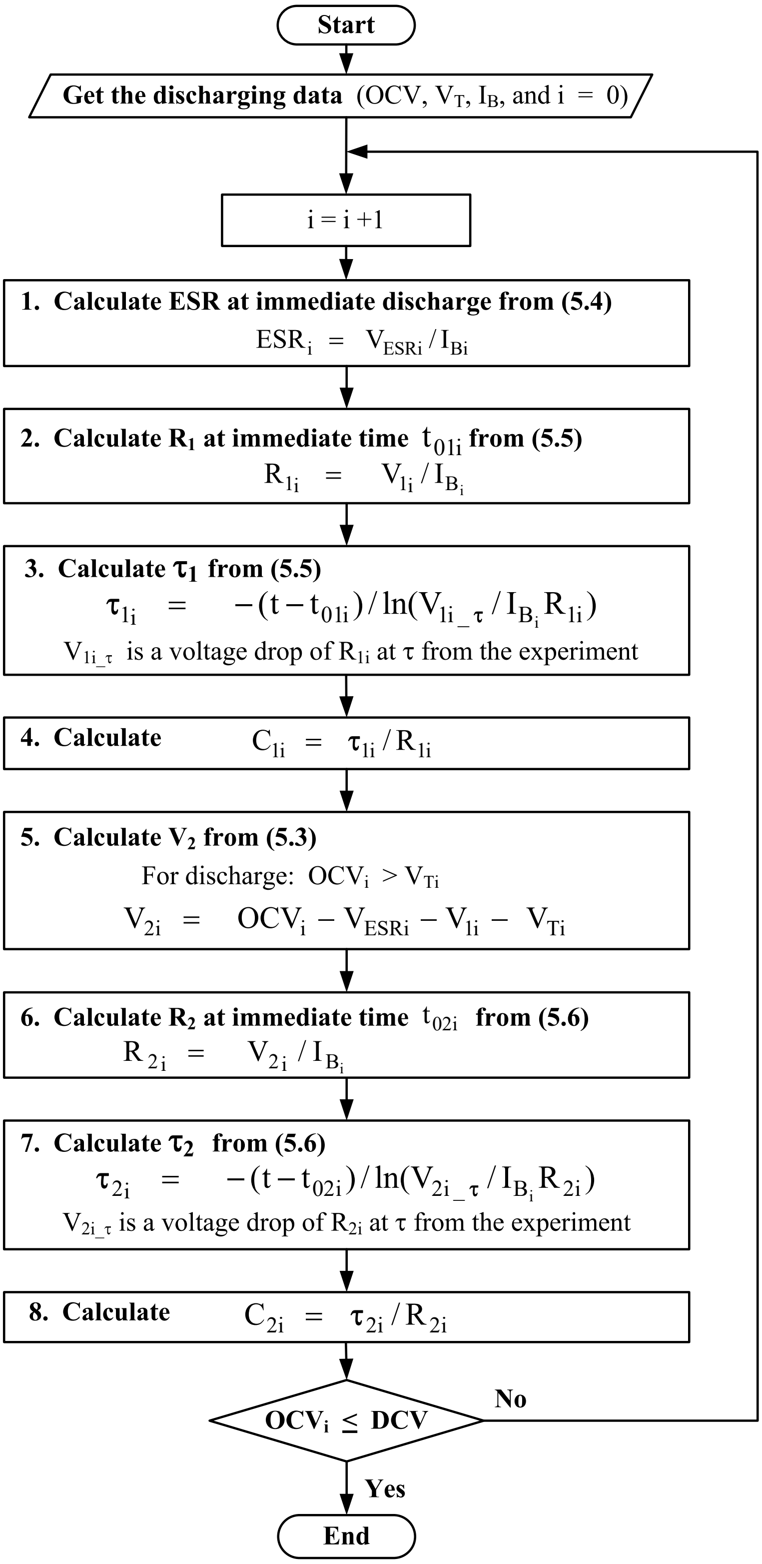

Figure 5.5 Flowchart of the proposed parameter identification method.

5.4 Battery parameter verification

The parameters from the transient response model with the proposed identification method of Figure 5.5 should be verified for studying the battery behaviors. In this case, we refer to the applied transient response equivalent circuit model to verify the identified parameters.

5.4.1 Equivalent circuit modeling

Figure 5.6 shows the applied transient response equivalent circuit model. It comprises of the state of charge voltage model based on the equivalent battery capacity (Left part of the circuit) and voltage-current characteristics model (Right part of the circuit) based on [4] considering with our practical testing information. The model is used to verify the identified parameters from the previous section. This model is implemented in a Spice simulation.

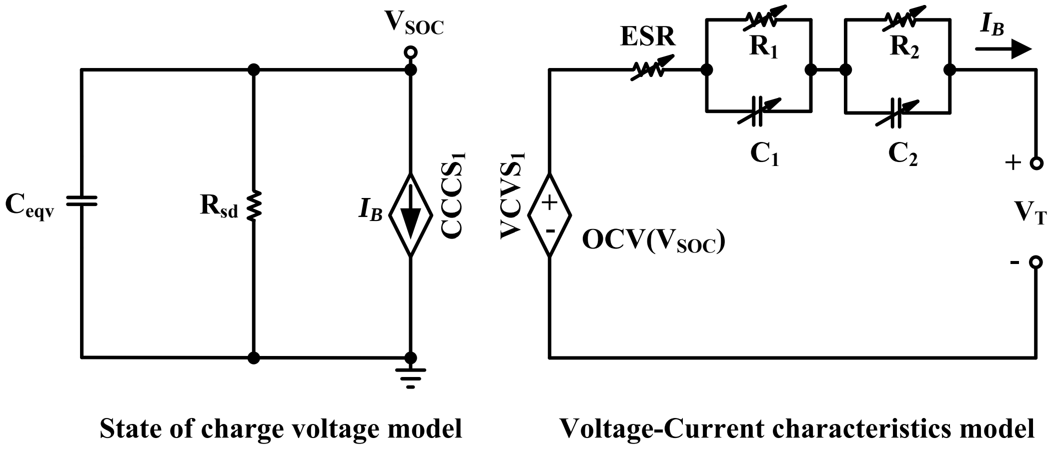

Figure 5.6 Applied transient response equivalent circuit model for parameter verification.

For the left part of circuit (state of charge voltage model) in Figure 5.6, a current controlled current source ($CCCS_1$) represents the battery current varying with the load to reflect a state of charge voltage (V_{SOC}) of the battery.

A self-discharge resistance (R_{sd}) represents the battery leakage. Usually, the rate of self-discharging is calculated over the month. The self discharge rate can be determined using long term experiments by comparing the RC-natural response voltage before and after taking a long resting when the cell is disconnected. For this battery, it is less than 3% per month. Then, in this simulation the self-discharge resistance will be ignored by setting to the infinity.

The next component is the equivalent capacitance (C_{eqv}). It is defined as an initial equivalent capacity of the LIB that is used for maintaining the battery voltage from the rated voltage to the end of discharged cut-off voltage of the battery at a standard condition (1C-rate at 20°C). The equivalent capacitance and rated energy of the LIB can be expressed as shown in Equations (5.7) and (5.8), respectively.

$$C_{eqv} = 2W_C / \left(V^2_{rated} - V^2_{cut-off}\right) \tag{5.7}$$

$$W_C = V_{rated} I_{rated} t \tag{5.8}$$

Where

C_{eqv} = Equivalent capacitance of the battery (F)

W_C = Rated energy of equivalent capacitance (J)

V_{rated} = Rated nominal voltage of the battery (V)

$V_{cut-off}$ = Discharge cut-off voltage of the battery (V)

I_{rated} = Rated operating current of the battery (A)

t = Time duration for the battery operation (sec)

A voltage controlled voltage source ($VCVS_1$) in the right part of circuit (voltage-current characteristics model) in Figure 5.6 represents the open circuit voltage of the LIB in a function of the SOC.

The elements ESR, R_1, C_1, R_2 and C_2 are the identified parameters, which are also set in the Spice simulation program. These parameters will be validated in the next section by observing a voltage response at the terminal of LIB.

5.4.2 Parameter verification

In order to verify the identified parameters, we set up a new experiment using the same test system in Chapter 3 for comparing the experiment with simulation results. The pulse currents are injected into the terminal of testing cell, with the different amplitudes and periods of pulse currents between -1C and 3C, for charging and discharging, respectively. Then, the voltage response behaviors at the terminal of testing cell are recorded. The equivalent circuit model of Figure 5.6 is used in the simulation with the parameters from the proposed identification method. The identified parameters are set in a Spice simulation environment. The simulated pulses with the same current amplitudes and periods as same as in the experiment are also set, and injected into the battery terminal of the circuit in the simulation.

A comparison between the experiment and simulation results for the model verification is shown in Figure 5.7. Figure 5.7a shows the time response of the simulation and experiment of testing current. Figure 5.7b illustrates voltage response behaviors for the simulation and experimental results. Figure 5.7b shows that the simulation of terminal voltage response has an acceptable conformity with the experimental result. The errors of voltage response between the experiment and simulation are shown in Figure 5.7c.

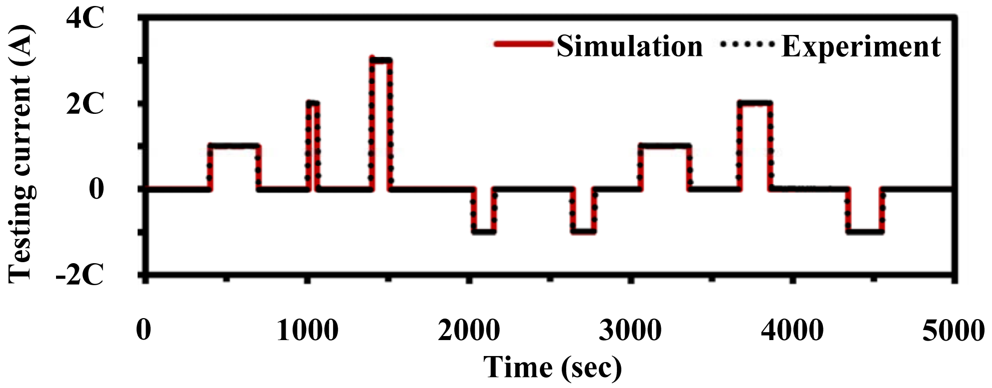

(a) Testing current.

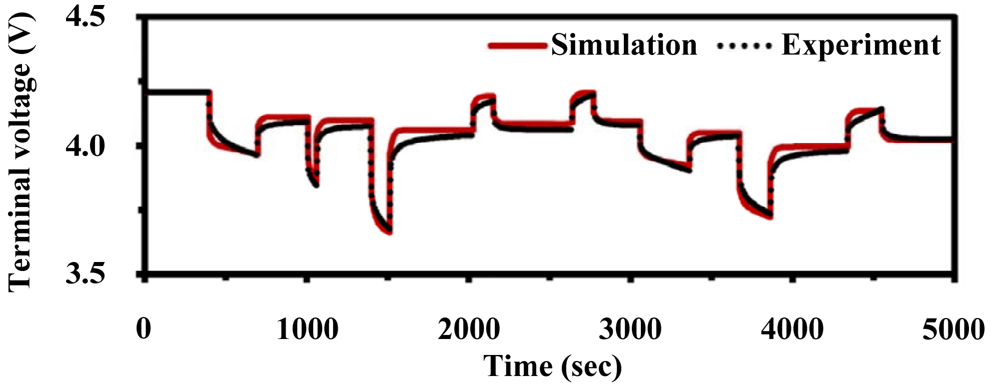

(b) Voltage response.

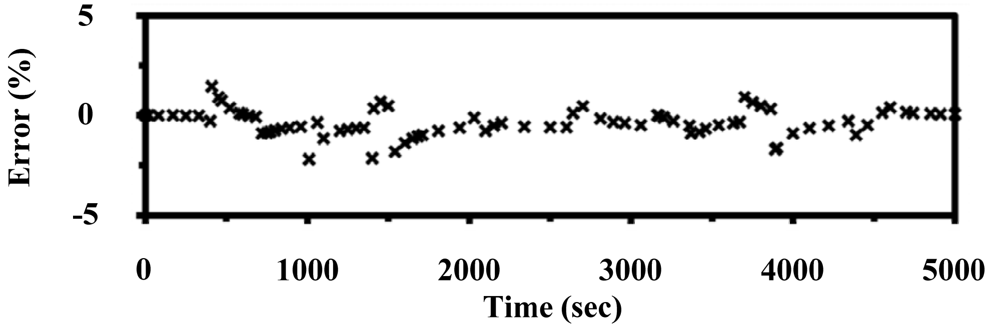

(c) Errors of voltage response behaviors between the experiment and simulation.

Figure 5.7 Comparison between the experiment and simulation results for parameter verification.

The errors and standard deviations (SD) of simulation model are summarized in Table 5.2. These results lead us to understand the terminal voltage behaviors of the battery with the chemical reaction variation.

Table 5.2 Errors and SD between the experiment and simulation.

Errors of simulated voltage	Max.	Min.	Average
	1.483 %	-2.173 %	-0.332 %
S.D. of the voltage responses			26.26 mV
S.D. of the errors			0.664%

5.5 Chapter summary

This chapter proposed the parameter identification method based on the experiment of transient responses and modelled the LMO. The proposed identification method including the calculation procedure can be applied for identifying the parameters for any Lithium-Ion battery types that have similar transient response behaviors. The model and parameters identified from the proposed method were validated in a simulated transient response model using a Spice simulation. The simulation showed an acceptable result by comparing with the experiments under the same condition, the standard deviation of the errors is only 0.664 %.

5.6 References

[1] B. Pattipati, B. Balasingam, G.V. Avvari, K.R. Pattipati, and Y. Bar-Shalom, “Open circuit voltage characterization of lithium-ion batteries”, J. Power Sources, Vol. 269, pp. 317–333, 2014.

[2] X. Hu, S. Li, H. Peng, and F. Sun, F. “Robustness analysis of state-of-charge estimation methods for two types of Li-ion batteries”, J. Power Sources, Vol. 217, pp. 209–219, 2012.

[3] B. Schweighofer, K. M. Raab, and G. Brasseur, “Modeling of high power automotive batteries by the use of an automated test system”, IEEE trans. on instrumentation and measurement, Vol.52(4), pp. 1087-1091, 2003.

[4] M. Chen and G.A. Rincon-Mora, “Accurate electrical battery model capable of predicting runtime and I-V performance”, IEEE Trans. On Energy Conversion, Vol. 21(2), pp.504-511, 2006.

Chapter 6

Analysis of Phase-transition Mechanism and Cycling Deterioration in the LMO

The study of battery behaviors has become a necessity in order to design the efficient BMS for large-scale energy storage applications. A SOH monitoring in the batteries is one of the important algorithms in the BMS, which is used for observing the deterioration of battery packs safely before the damage occurring.

Numerous researchers have reported interesting studies about the SOH and capacity deterioration of LIBs [1-4]. However, they focused on the utilization in model applications, which is based on the impedance changes and capacity and power fades of the cells to estimate the battery lifetime and healthiness without considering the electrochemical processes inside the battery. In order to develop the BMS efficiently, it is necessary to understand the electrochemical changes, which are related to the intercalation process and phase-transition mechanisms in cycling operations.

The aim of this study is to understand the relevant deterioration mechanisms in the LMO battery, meaning of OCV characteristic changes and their electrode properties regarding the phase-transition mechanisms. Differential voltage (DV) and incremental capacity (IC) techniques are applied for analyzing the phase-transition behaviors.

Based on the changes of DV and IC characteristics for the OCV, the phase-transitions are discussed and evaluated to understand electrochemical changes and deterioration mechanisms in the batteries during cycling operations.

6.1 Methodology for phase-transition analysis

In order to study the phenomena that occur during phase-transitions in the LMO, the differential voltage analysis (DVA) and incremental capacity analysis (ICA) were used. DVA and ICA are non-destructive methodologies, which use only a numerical process and have no need of a physical separation for each half-electrode of the testing cell. They can also be applied for investigating the cycling deterioration of LIBs during the operations [5,6].

The OCV was determined using the characterization system as explained in Chapter 3. The test system for the OCV used the same test condition at a step-size (ΔSOC) of 1-5% with a low constant current amplitude of 0.05C-rates (or 0.175A) at 20°C to clearly reflect the electrode property following a recommendation for the accurate OCV characterization [7].

After extracting the OCV_E and Q_B data and forming a polynomial $OCV(Q_B)$ model in Equation (6.1), the coefficients (φ) were determined by a nonlinear least square technique in MATLAB following the objective function in Equation (6.2). Then, the DVA and ICA are obtained by Equations (6.3) and (6.4), respectively.

$$OCV(Q_B) = \sum_{k=0}^{n} \left(\varphi_k Q_B^k \right) \tag{6.1}$$

$$\min_{\varphi} \left\| f(\varphi, Q_B) - OCV_E \right\|^2 = \min_{\varphi} \sum_{i=1}^{m} \left[f\left(\varphi, Q_{B_i}\right) - OCV_{E_i} \right]^2 \tag{6.2}$$

$$\mathrm{DVA} = \frac{\mathrm{dOCV}(Q_B)}{\mathrm{d}Q_B} = \sum_{k=1}^{n}\left(k \cdot \varphi_k \cdot Q_B^{k-1}\right) \tag{6.3}$$

$$\mathrm{ICA} = \frac{1}{\mathrm{DVA}} = \frac{\mathrm{d}Q_B(\mathrm{OCV})}{\mathrm{dOCV}} \tag{6.4}$$

Where

Q_B = Accumulated capacity (Ah)

OCV_E = Extracted OCV (V)

m = Number of Q_B and OCV_E data

n = Best-fit order of the model

φ = OCV fitting coefficient, $\varphi = [\varphi_1, \varphi_2, \ldots, \varphi_n]$

$f(\varphi, Q_B)$ = OCV model function for the objective equation

6.2 OCV and phase-transition relationships

The OCV characteristic of LIB depends on the difference in electrochemical potential of their specific material properties for electrodes and the effective concentration of Lithium during operations. The OCVs, which is extracted from the characterization system in Chapter 3, are shown with the black line in Figure 6.1.

The start and end of the charge operation in Figure 6.1a (Regions 2 and 6) give the minimum and maximum concentrations of Li-ions, respectively, and a steep rise of voltage implies the increase of Lithium concentration at the electrode surfaces and interface of the electrolyte [8]. While the decrease of Lithium concentration is found at the end and start of discharging for Regions 2 and 6 in Figure 6.1b, respectively. Two-step potentials (Regions 3 and 5 on the voltage profiles), where are nearly a constant voltage, reflect a small changing of Lithium concentration that intercalated between electrode surfaces during the phase transition. These behaviors can be explicitly interpreted by observing the voltage changes to their related capacities (dV/dQ) with the DVA.

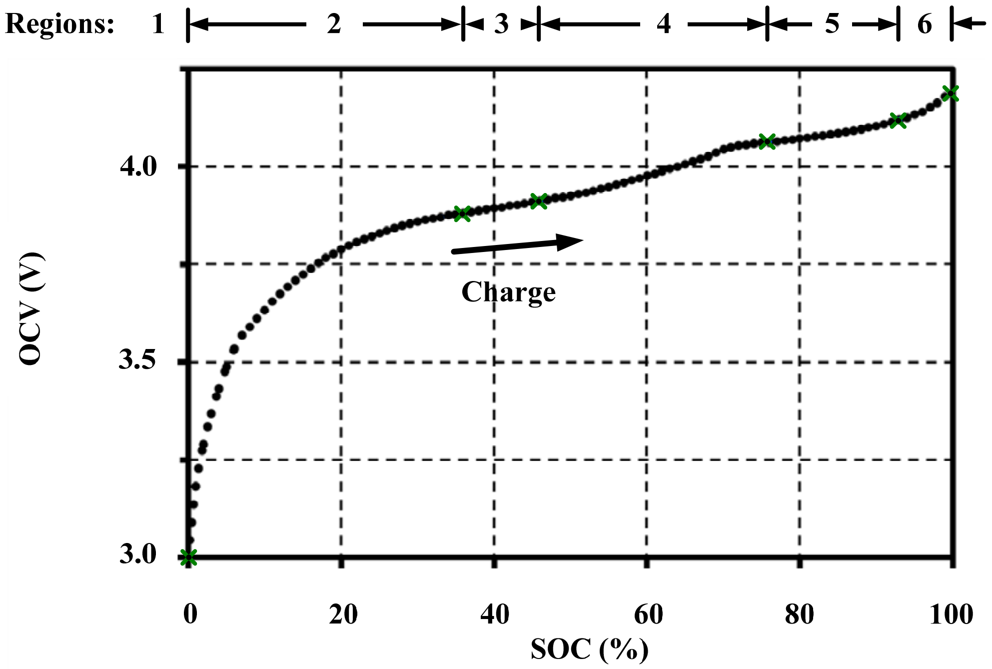

(a) Extracted from charge process

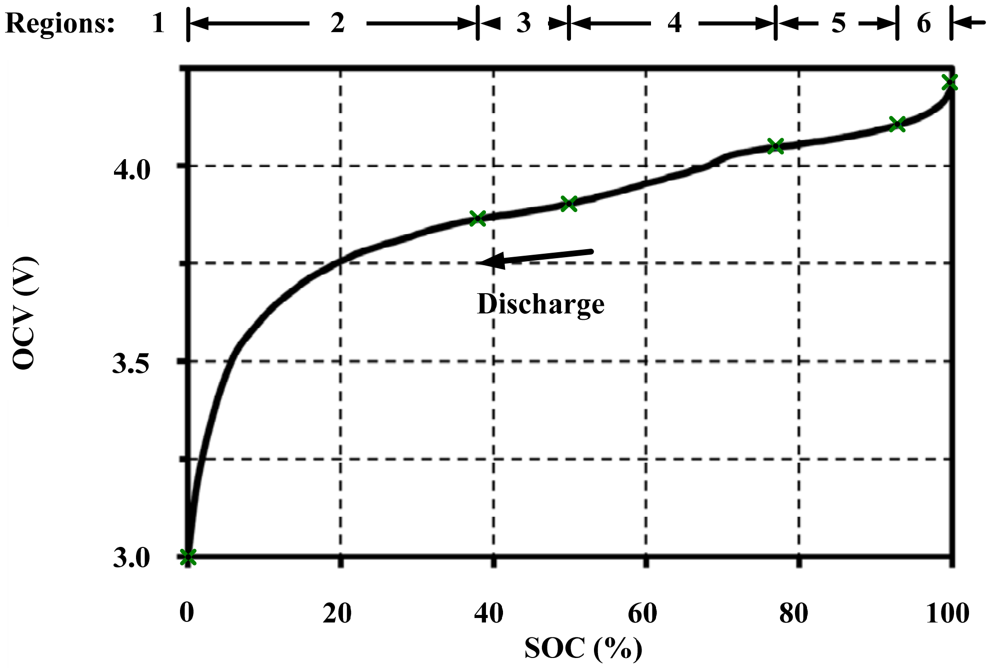

(b) Extracted from discharge process

Figure 6.1 OCV characteristics of the LMO.

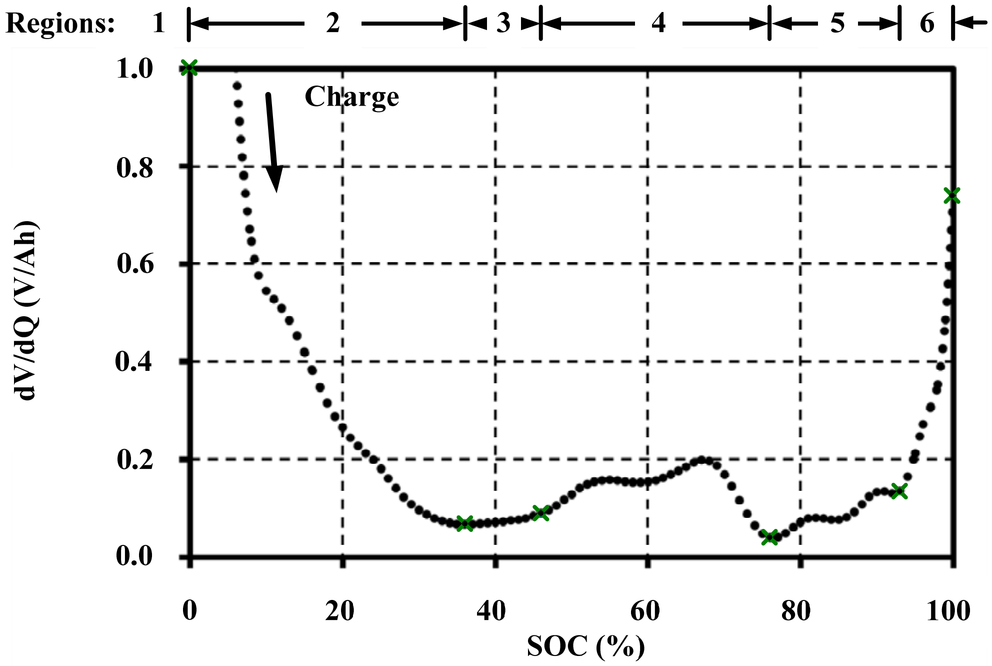

(a) DV for charging process

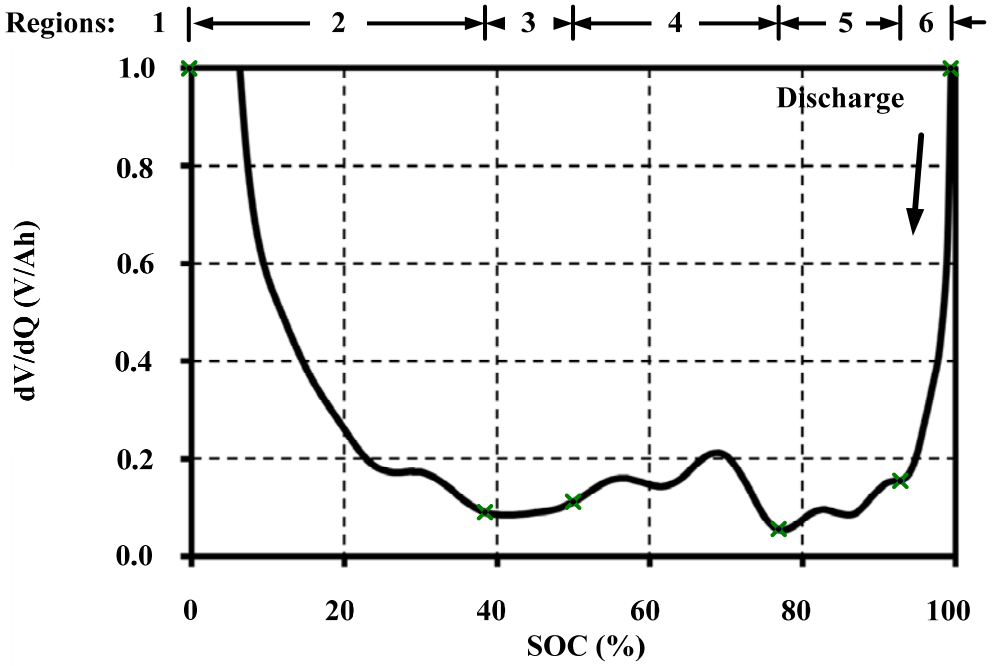

(b) DV for discharging process

Figure 6.2 Differential voltage (DV) characteristics of the LMO.

Figure 6.2 shows the DV characteristics of the LMO, which clearly illustrated the phase-transitions with the peaks of dV/dQ (Region 4) between the two flat-plateaus. The dV/dQ quantitatively has slight differences between the charge and discharge as shown in Figure 6.2a and 6.2b, respectively. All regions for the phase-transition explanation are also identified by these changes of the DV between the plateaus.

The two-step potentials on the voltage profile are evaluated by the incremental capacity (dQ/dV vs. V) from the ICA. Figure 6.3 shows the incremental capacity characteristics of the LMO. The trends of dQ/dV characteristics to the OCV have also slight differences between the charge and discharge as shown in Figure 6.3a and 6.3b, respectively.

The LMO electrode has a two-phase transition property [9]. For the first phase transition, Li-ions are inserted into the octahedral site in a spinel structure at approximately 3V [10] as shown by Region 1 in Figure 6.1a, 6.2a and 6.3a. This transition results from a changing of the crystal structure from the $LiMn_2O_4$ cubic spinel structure (Fd3m space group) to the $Li_2Mn_2O_4$ orthorhombic spinel structure (Fddd space group, or a rock-salt composition structure) on the electrode surface [11].

During the insertion of Li-ions, the manganese ions are changed from Mn^{4+} to Mn^{3+} in relation to the gradual increasing of the accumulated charge on the electrode [9]. As a result, the dV/dQ for the charging process is continuously decreased at an intermediate state (Region 2 of Figure 6.2a) corresponding to the gradual increases of dQ/dV on the IC curve (Region 2 of Figure 6.3a) as the first phase transition (3V). However, the phenomenon at this state for the discharging is occurring conversely (Region 2 of Figure 6.2b and Figure 6.3b).

Such a phenomenon that keeps the trend of characteristics looks similar to both charge and discharge. This behavior is consistent with a slow reduction of accumulated charge of the discharging near the first transition.

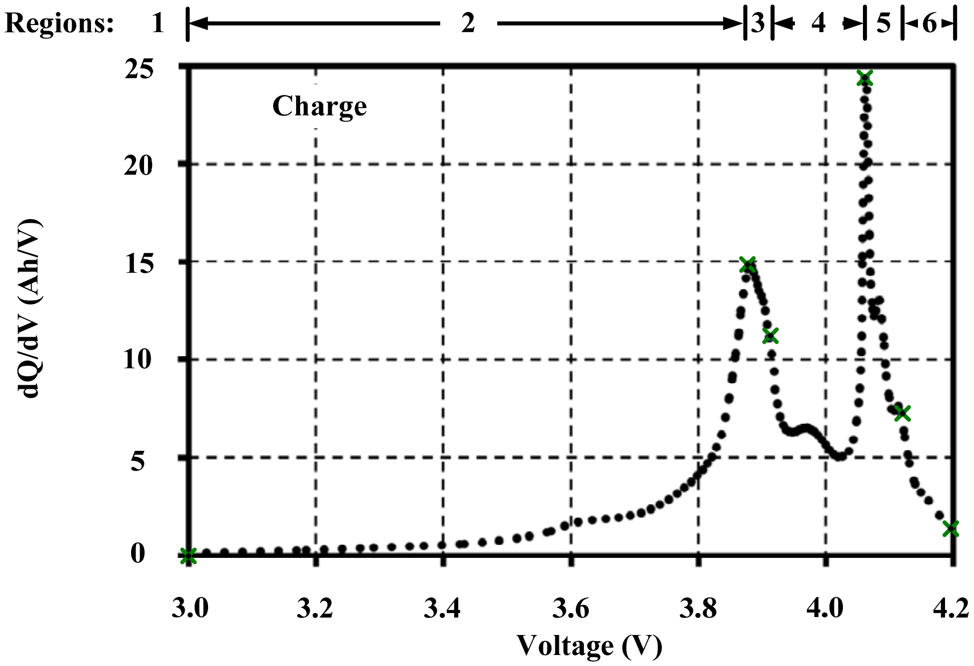

(a) IC for charging process

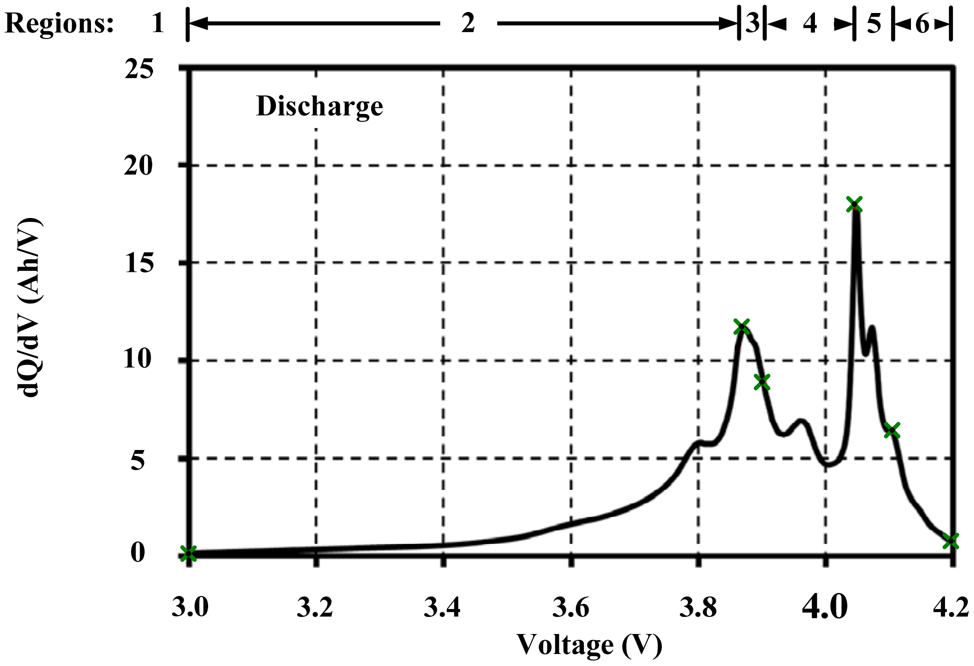

(b) IC for discharging process

Figure 6.3 Incremental capacity characteristics of the LMO.

Next, we consider the second phase transition. From Region 4 in Figure 6.1, the obvious potential peaks around the 4V-region can be observed. These peaks between two-step potentials occurred around 3.88-3.91V and 4.06-4.12V for charging (Regions 3 and 5 in Figure 6.1a), and occurred around 3.87-3.90V and 4.05-4.11V for discharging (Regions 3 and 5 in Figure 6.1b). These two-step potentials are identified by the low dV/dQ (mostly exhibiting a constant voltage during changing of capacity) as shown by Regions 3 and 5 of Figure 6.2a and 6.2b, respectively. Besides, the peak of dQ/dV as shown in Figure 6.3 can also represent the two-step potentials. The steep increase of the dQ/dV implies that the concentration of Lithium at this state is hardly changed with the injected charge. These IC peaks clearly illustrate the starting point of the step potential. In Figure 6.3a, the dQ/dV peaks for charging shown in Regions 3 and 5 are 14.76 Ah/V and 24.35 Ah/V, respectively, while the dQ/dV peaks for discharging shown in Regions 3 and 5 (Figure 6.3b) are 11.67 Ah/V and 17.85 Ah/V, respectively.

The de-intercalation process is referred for the second phase transition. In this state, a spinel structure is starting to change back from the orthorhombic to cubic structures. Li-ions are extracted from the tetrahedral sites of the spinel structure at approximately 4V with the two-step potentials separated by 0.10-0.15V [12].

In addition, a two-step process observed on the voltage profile is due to the ordering of Li-ion diffusion [13]. In this ordering, a Li-ion is on the one-half of the face sharing for the tetrahedral 8a sites along the diffusion path, where Li-ions are moving rapidly to the vacant octahedral 16c site along the 3D structure of the 8a-16c-8a-16c pathway. This ordering, followed by a steep potential peak, causes a second phase transition [10]. This transition behavior between the two-plateaus of electrochemical equilibrium condition can be clearly seen from the peak areas of dV/dQ, which are 0.1983 V/Ah (at 67% SOC) for charging and 0.2127 V/Ah (at 69% SOC) for discharging as illustrated by Region 4 in Figure 6.2a and Figure 6.2b, respectively. A steep slope of dV/dQ at the end of charging indicates the abrupt voltage increase for the surplus charge at the end of the intercalation process as illustrated by Region 6 of Figure 6.2a. On the contrary, a steep slope of dV/dQ at the start of discharge indicates the abrupt voltage decrease for the surplus charge at the starting of the de-intercalation process as illustrated by Region 6 of Figure 6.2b. In conclusion, a phase-transition behavior in the LMO can be explicitly interpreted with the related experimental OCV associated with dV/dQ and dQ/dV on the DV and IC curves, respectively.

6.3 *Cycling deterioration in the LMO*

In order to study the cycling deterioration and influence of characteristic changes in the LMO on the phase transition, a cell was tested at standard testing temperature 20°C with the full rate of charge (1C) and the full rate of discharge (5C). The OCV and incremental capacity characteristics of the LMO were extracted for 400 cycles, 1,200 cycles and 2,400 cycles as shown in Figure 6.4 and Figure 6.5, respectively.

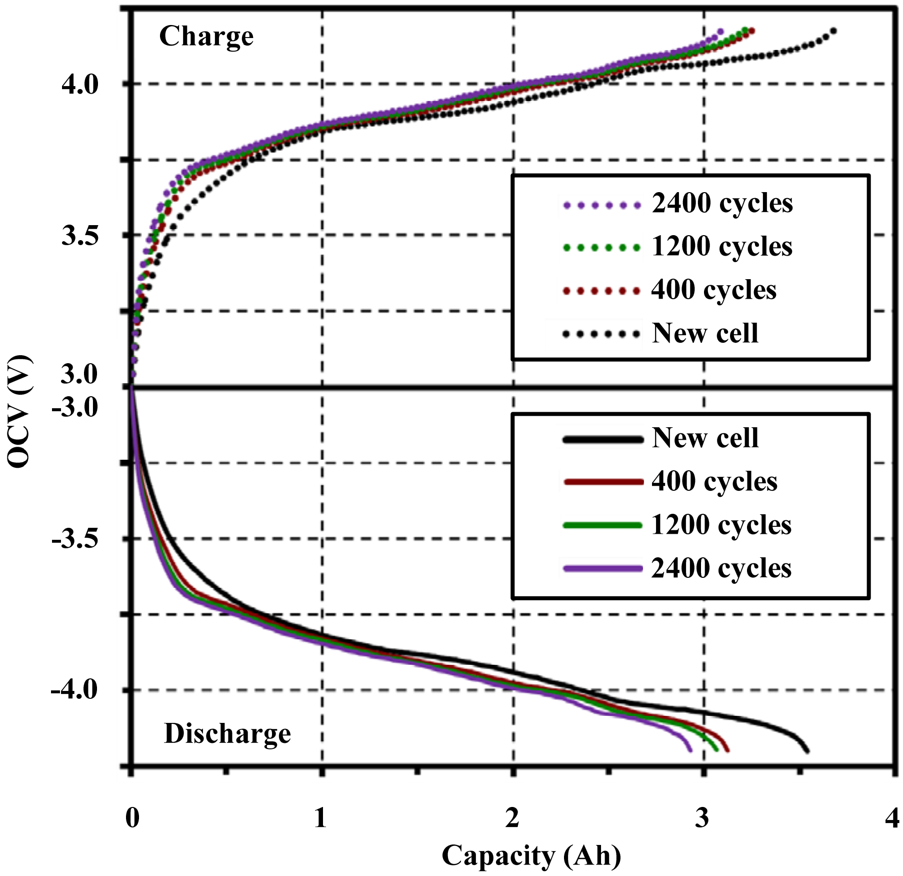

Figure 6.4 OCV characteristics of the LMO at different cycles.

The OCV patterns in Figure 6.4 slightly change with the cycles. A shrinking of tails on the OCV curves reveals that the increasing cycles drop the capacity of the cell. A build-up of the OCV around the knee point can be clearly observed by transforming it into the IC characteristic (Figure 6.5) after the first phase transition around 3.70V and 3.74V for discharge and charge, respectively. This steep voltage change stems from the large variation of a concentration of lithium. These phenomena are noticeable after the cycling number of the cell increases.

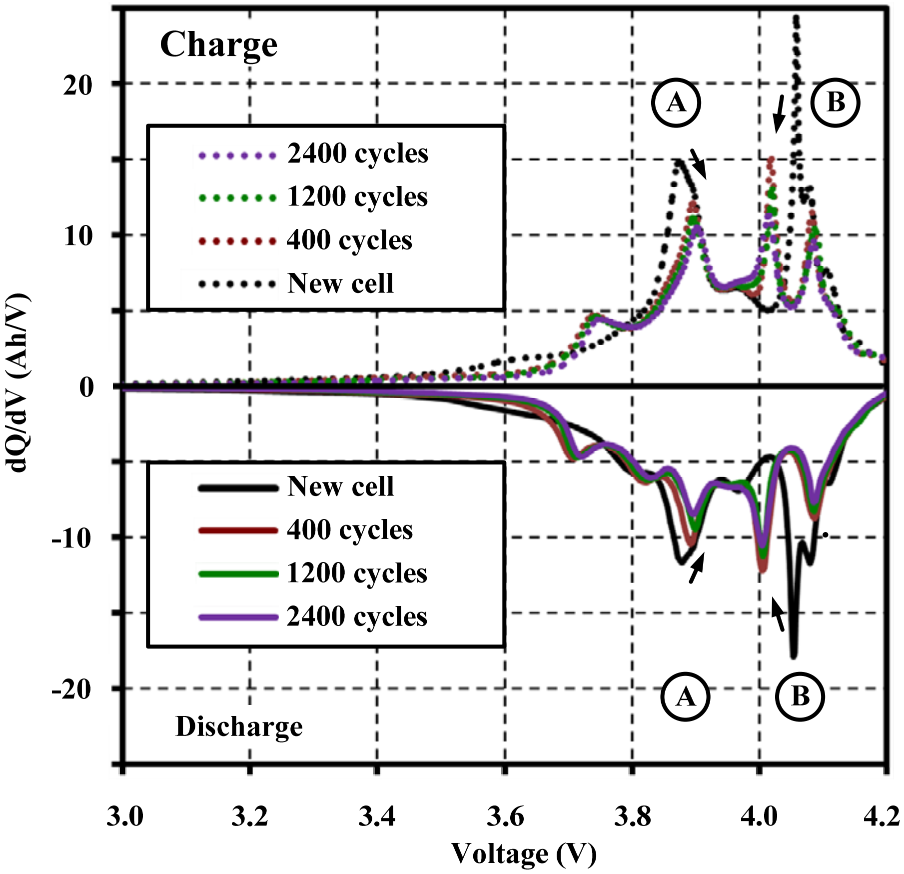

Figure 6.5 IC characteristics of the LMO at different cycles.

The extracted IC characteristics of Figure 6.5 can also be used to display a slight change of the OCVs, especially in the linear-region range around the middle part of Figure 6.4. They obviously show that the increasing number of cycles reduces the peak amplitudes and shifting of peak positions around the 4V-region. The deterioration of capacity and IC with cycling operations is shown in Figure 6.6.

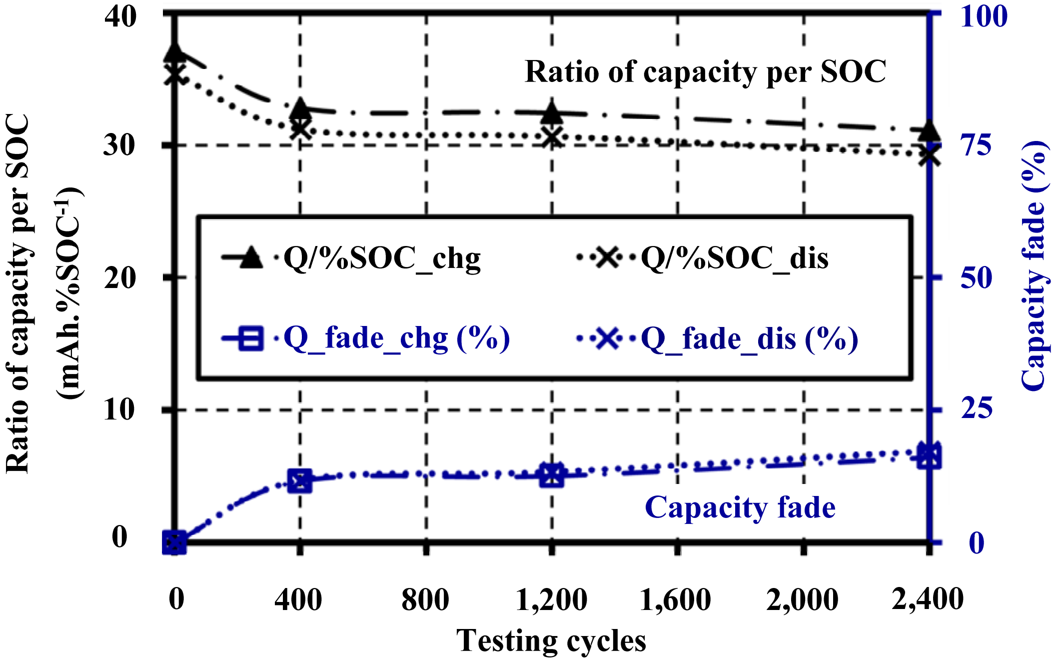

(a) Capacity variations

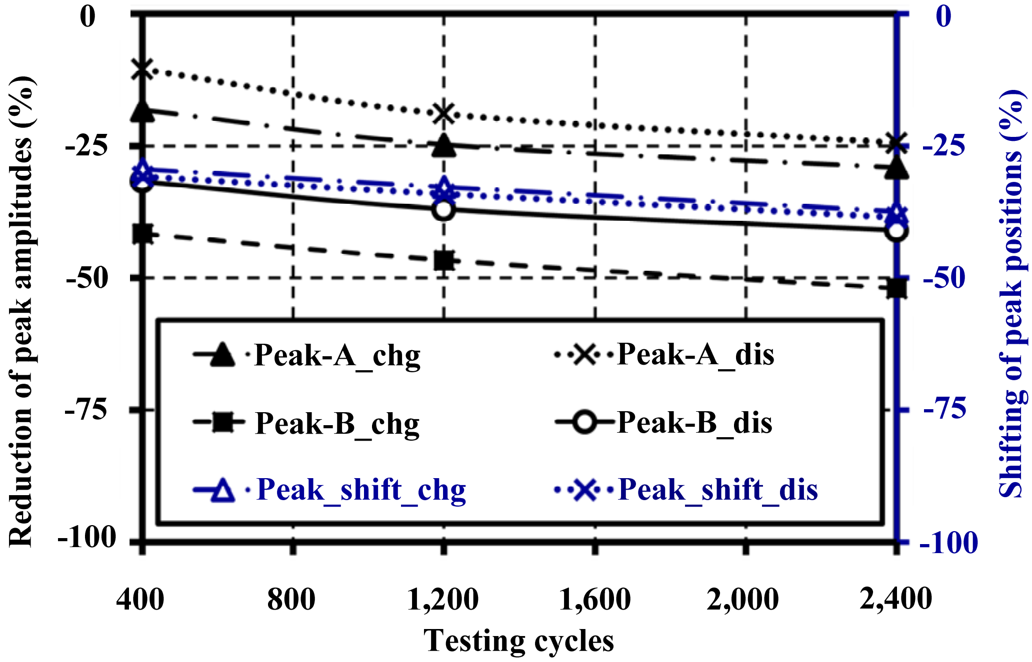

(b) IC variations

Figure 6.6 Deterioration trends of LMO under the cycling operations.

Figure 6.6a shows the capacity fade and the ratio of capacity per SOC (also called the capacity ration) on the increasing of cycles. The results show that capacity fades of the cell for 400 cycles, 1,200 cycles and 2,400 cycles increase by 11.55%, 12.56% and 16.02% for charge and 11.72%, 13.31% and 17.18% for discharge, respectively. The cycling capacity fade is mainly due to the loss of cycleable lithium with growing of the solid electrolyte interface (SEI) layer on the surface of the carbon-based negative electrode [14], and is partly due to the loss of active electrode materials [15].

Figure 6.6b shows the reduction of IC peak amplitudes and shifting of peak positions between the peaks A and B of Figure 6.5 for the cycling operations. The reduction of IC peaks reflects the cycling capacity fade for the process of intercalation and de-intercalation, while the shortening of the distance between the peaks around 4V-region reflects the shrinkage of the two-step potentials during the phase transformation.

The cell deterioration can be explained in term of the phase transformation during lithium intercalation/de-intercalation. In the intercalation process, Li-ion occupies a tetrahedral coordination and Mn-ion occupies an octahedral coordination in the form of MnO_6. During the intercalation and de-intercalation, the transformations between cubic and orthorhombic crystal systems are occurring. Cubic lattices are stretched to orthorhombic lattices along orthogonal pairs for the intercalation, and the process is reversed for Lithium de-intercalation [16, 17].

The distortion by the changing of structure causes crystal asymmetry and causes stress. This results in electromechanical grinding on those spinel particles that affect the reversibility of the phase-transition and gradual capacity deterioration during the cycling operations [11]. These tendencies of cycling deterioration can be observed by the peak changes of dQ/dV around the 4V-region, the average rate of the reduction of peak amplitudes and the narrowing of the voltage gap between the two peaks is approximately $5.406 \text{ x}10^{-3}$ % per cycle and $3.919 \text{ x}10^{-3}$ % per cycle, respectively.

6.4 Chapter summary

In this chapter, phase-transition mechanisms of manganese-type Li-ion batteries were studied. The open-circuit-voltage (OCV) characteristics were extracted using a proposed characterization system, and analyzed with the differential voltage (DV) and incremental capacity (IC) techniques. The DV peak indicates the second phase-transition around the 4V-region, while the IC peak indicates the starting point of the OCV step plateau, which is the electrochemical equilibrium condition during the phase transformation. The capacity fade and variation of the IC peaks can be used as a deterioration index of the cell. From the study, we found that the cycling operation reduces the IC peak amplitudes and narrows the voltage gap between the peaks by 5.406×10^{-3} % per cycle and 3.919×10^{-3} % per cycle, respectively. These studies let us understand the phase transformation behaviors and related characteristic interpretation of the cell.

6.5 References

[1] V. Marano, S. Onori, Y. Guezennec, G. Rizzoni, and N. Madella, “Lithium-ion batteries life estimation for plug-in hybrid electric vehicles”, Proc. IEEE Conf., Veh. and Power Propulsion, Michigan, USA, pp. 536-543, 7-11 September, 2009.

[2] L. Lam and P. Bauer, “Practical capacity fading model for Li-ion battery cells in electric vehicles”, IEEE Trans. on Power Electronics, Vol. 28(12), pp. 5910-5918, 2013.

[3] P. Rong and M. Pedram, “An analysis model for predicting the remaining battery capacity of Lithium-ion batteries”, IEEE Trans. on VLSI Systems, Vol. 14(5), pp. 441-451, 2006.

[4] H.F. Yuan and L.R. Dung, “Offline state-of-health estimation for high-power lithium-ion batteries using three-point impedance extraction method”, IEEE Trans. on Veh. Tech., Vol. 66(3), pp. 2019-2032, 2017.

6.5 References (Cont.)

[5] M. Dubarry and B.Y. Liaw, "Identify capacity fading mechanism in a commercial $LiFePO_4$ cell", J. Power Sources, Vol. 194, pp. 541-549, 2009.

[6] Y. Zhang, C.Y. Wang, and X. Tang, "Cycling degradation of an automotive $LiFePO_4$", J. Power Sources, Vol. 196, pp. 1513-1520, 2011.

[7] N. Somakettarin and T. Funaki, "Study on factors for accurate open circuit voltage characterizations in Mn-type Li-ion batteries", Batteries, Vol. 3(8), pp. 1-13, 2017.

[8] D. Klotz, "Characterization and modeling of electrochemical energy conversion systems by impedance techniques", Ph.D. Dissertation, Karlsruher Institute of Technology, Germany, 2012.

[9] J. Bisquert, Nanostructured energy devices: Equilibrium concepts and kinetics, CRC press, Taylor & Francis group, Florida, 1st ed., pp. 115-155, 2015.

[10] T. Ohzuku, M. Kitagawa, and T. Hirai, "Electrochemistry of manganese dioxide in lithium nonaqueous cell: III X-ray diffractional study on the reduction of spinel-related manganese dioxide", J. of Electrochem. Vol. 137(3), pp. 769-775, 1990.

[11] T. Eriksson, "$LiMn_2O_4$ as a Li-ion battery cathode from bulk to electrolyte interface", Ph.D. Dissertation, Uppsala University, Sweden, 2001.

[12] N. Somakettarin and T. Funaki, "Parameter extraction and characteristics study for manganese-type lithium-ion battery", Int. J. of Renewable Energy Research, Vol. 5(2), pp. 464-475, 2015.

[13] K. Ozawa, Lithium Ion Rechargeable Batteries: Materials, Technology, and New Applications, Wiley-VCH Verlag GmbH, Germany, 1st ed., pp. 103-157, 2009.

6.5 References (Cont.)

[14] R. Deshpande, M. Verbrugge, Y.T. Cheng, J. Wang, and P. Liu, “Battery cycle life prediction with coupled chemical degradation and fatigue mechanics”, J. Electrochem., Vol. 159(10), pp.A1730-A1738, 2012.

[15] X. Han, M. Ouyang, L. Lu, and J. Li, “Cycle life of commercial lithium-ion batteries with Lithium titanium oxide anodes in electric vehicles”, Energies, Vol. 7, pp. 4895-4909, 2014.

[16] J. E. Greedan, “Geometrically frustrated magnetic materials”, J. Mater. Chem., Vol. 11, pp. 37-53, 2001.

[17] G. Rousse, C. Masquelier, J.R. Carvajal, E. Elkaim, J.P. Lauriat, and J.L. Martinez, “X-ray study of the spinel $LiMn_2O_4$ at low temperature”, Chem. Mater., Vol. 11, pp. 3629-3635, 1999.

Chapter 7

Conclusion

This dissertation dealt with a lithium manganese oxide secondary battery (LMO). The focus of this dissertation was on the characterization and modeling of the LMO. The first part overviewed the structure and related mechanism that are the important knowledge to understand the LMO equivalent circuit modeling, and to analyze the characteristic of the battery. The LMO comprised of positive $LiMn_2O_4$ spinel-type and negative graphite electrodes. This spinel compound has dominant properties in high nominal voltage per cell, high discharge current rupturing, high thermal stability for over-charge, and notable performance for fast charge and discharge operations due to its stable crystal structure.

The important contributions in this dissertation are the designs of programmable Li-ion battery characterization and life-cycle testing systems. They are developed in a LabVIEW environment, and can be applied for any Li-ion cell types. The developed charge and discharge systems implemented with our sequential-controlled and protection algorithms can correctly manipulate all of scheduling of the tests for battery parameter characterization and cycling investigations of the LMO with safety. The dominant features of the developed systems are: 1) the automatic testing system with a real-time monitoring, which can display all status of operations; and 2) the conditional charge/discharge cutting algorithms, which can detect and cut-off testing instruments in case of the fault occurrences, and can show the alarm messages, such as over current, over power and over/under voltage events, during operations. These proposed algorithms can be considered for the further BMS development.

In the analysis part of LMO characteristic results, several adjusting factors were tested. The factors that affected the inaccurate open-circuit-voltage (OCV) during the characterizations are: 1) the large step-size of the pulse tests over than 5% for all of the SOC range; and 2) the resting period of the cell less than 60 min for each pulse test. This studied cell illustrated a small hysteresis character between the charge and discharge operations with the maximum voltage gap of only 0.758% of its average value. It is found that the current amplitudes (C-rates) of the pulse tests have no effect on the OCV and effective series resistance (ESR) under the constant temperature. For the temperature effect study, the capacity deterioration and ESR in the LMO have greatly affected by low temperature. The ESR had increased with the low temperature, and the capacity deterioration had obviously increased especially under low temperature and large current conditions. These results let us understand the characteristics of the LMO battery including the capacity deterioration under the various conditions of temperatures and operating currents. The empirical results of study can also be used as a fundamental testing guideline for engineers who design the energy storage system (ESS) with LIBs and its management system and/or the battery protection system in order to consider the optimal operating conditions for other similar batteries.

This dissertation also introduced the electrical equivalent circuit modeling for the LMO. The model parameters were extracted using the proposed identification method based on the experiment of transient responses. They were validated in a Spice simulation with the practical testing information. The terminal voltage response showed an acceptable conformity between the experiment and simulation to the different periods and amplitudes of pulse currents. A simulated dynamic voltage of the model can be used for studying and predicting voltage response behaviors of the battery to the variation of applied terminal current before the worst-case occurrence such as over current or under/over voltage phenomena.

In the last part, the cycling deterioration related with the phase-transition mechanism was analyzed by using the differential voltage (DV) and incremental capacity (IC) techniques. This LMO indicated the phase-transformation around the 4V-region by observing at the DV peak obtained from the accurate extracted OCV.

Two main processes that affected the battery ability and capacity deterioration are the intercalation and de-intercalation under long cycling operations of charge and discharge. The deterioration of aged cells can be observed by the variations of IC peak and capacity. The phase-transition study helped us to understand the basic mechanism of cycling capacity fade and the deterioration occurring in the LIB, and provide us essential knowledge for further investigations about the cell deteriorations and state of health monitoring under the cycling operations for the BMS development.

It should be noted that this LMO type might not be the most prominent battery on the market due to the rapid development of battery technology. However, the results of our experiment of 2,400 cycles can guarantee that this battery type is sufficiently safe for long cycling operations of charge and discharge.

The proposed characterization method, modeling, analysis techniques, electrochemical explanations and results of the study can be used to provide us essential knowledge for further development of the BMS design, and can also be applied for studying the behaviors and dynamic responses of other similar electrode Li-ion batteries, or the batteries with manganese-based composition.

In addition, studies of life extension, efficient battery-management system design, behavior prediction and accurate state estimation based on the proposed knowledge of characterization and modeling are still necessary to be investigated for modern lithium batteries. These issues are the challenging topics for future studies.

List of publications

Journals

J-1 N. Somakettarin and T. Funaki, “Parameter extraction and characteristics study for manganese-type lithium-ion battery”, Int. J. of Renewable Energy Research, Vol. 5(2), pp. 464-475, 2015.

J-2 N. Somakettarin and T. Funaki, “Study on factors for accurate open circuit voltage characterizations in Mn-type Li-ion batteries”, Batteries (MDPI), Vol. 3(8), pp. 1-13, 2017.

J-3 N. Somakettarin, H. Sugihara, and T. Funaki, “Open-circuit-voltage characterization system design for studies of phase-transition mechanism and deterioration in Mn-type Li-ion batteries”, IEICE Electronics Express, Vol. 14(15), pp. 1-11, 2017.

Conferences

C-1 N. Somakettarin and T. Funaki, “An experimental study on modeling of transient response and parameters identification for Mn-type Li-Ion battery with temperature dependency”, Int. conf. on renewable energy research and applications (ICRERA), Wisconsin, USA, Available on http://ieeexplore.ieee.org, pp.804-809, 19th-22nd Oct 2014.

C-2 N. Somakettarin and T. Funaki, “An experimental study on the effect of temperature on effective series resistance and open circuit voltage for Mn-type Li-Ion battery”, Conf. on Electronic Components and Materials research, IEICE and cosponsored by IEEE Power Electronics Society, Tokyo, Japan, Vol.113, No.445, CPM2013-152, pp.15-20, 27th Feb 2014.